A Measurement of the Z Forward-Backward Charge Asymmetry in $p\bar{p} \rightarrow e^+e^-$

by

Jedong Lee

Submitted in Partial Fulfillment of the
Requirements for the Degree of
Doctor of Philosophy

Supervised by
Professor Kevin McFarland
Physics and Astronomy
The College
Arts and Sciences

University of Rochester
Rochester, New York
2006

Curriculum Vitae

The author attended Yonsei University from 1993 to 2000, and graduated with a Bachelor of Science degree in physics. He came to the University of Rochester in the Fall of 2000 and began graduate studies in Physics. He received a Robert E. Marshak Fellowship in 2003 and 2004. He pursued his research in High Energy Particle Physics under the direction of Professor Kevin McFarland and received the Master of Science degree from the University of Rochester in 2002.

Acknowledgements

This thesis would have never existed without the help and support of so many people. First and foremost, I would like to thank my advisor Kevin McFarland, for his teaching and support. His advice always kept me on track along the long and exhausting way of graduate studies. I am indebted to Kevin for any development that I have made as a physicist.

I would like to thank the colleagues involved in the Z' analysis, Catalin Ciobanu, Sam Harper, and Greg Veramendi. The time we spent together was dreadfully productive and also enjoyable. I owe a great deal to the CDF group of the University of Rochester. I am grateful to Gilles DeLentdecker for the co-work during his stay with the Rochester group and afterwards.

I owe a great deal to fellow students, Sarah Demers, Ben Kilminster and Bo-Young Han. Special thanks to theory physicists, Jung-il Lee, Paul Langacker, and Heather Logan, for their invaluable advice. Finally, I thank my family for being always supportive and trustful.

Abstract

We present a measurement of the Z boson forward-backward charge asymmetry of the process $p\bar{p} \rightarrow \gamma^*/Z + X \rightarrow e^+e^- + X$, where the mass of the intermediate γ^*/Z has invariant mass above 30 GeV/c^2. The measurement uses 0.36 fb^{-1} of Run II data. The method of matrix inversion is used to correct for the distortion in the measurement caused by the detector resolution and photon radiation in the final state. A search for a new physics based upon the forward-backward asymmetry is also presented.

Contents

Curriculum Vitae **ii**

Acknowledgements **iii**

Abstract **iv**

List of Tables **vii**

List of Figures **viii**

Introduction **1**

1 Theory **4**

1.1 Electroweak Theory of the Standard Model 4

1.2 Z Boson 8

1.3 Extra Neutral Gauge Boson 12

2 Apparatus **17**

2.1 Accelerator 17

2.2 Collider Detector at Fermilab 20

2.2.1 Central Outer Tracker 22

2.2.2 Electromagnetic Calorimeter 24

2.3 Data Acquisition System 26

3 Data Sample **31**

3.1 Electron Reconstruction 31

3.2 Selection Variables 33

3.3 Monte Carlo Sample . . . 37
3.4 Trigger Requirements . . . 37
3.5 Selection Cuts . . . 43
3.6 Energy Scale . . . 43

4 Background **49**
4.1 Di-jet Background . . . 49
4.1.1 Isolation Fit . . . 51
4.1.2 Normalizing the Mass Distribution . . . 56
4.1.3 Systematic Uncertainties . . . 64
4.2 Electroweak Background . . . 67

5 Forward-Backward Asymmetry **69**
5.1 Unfolding . . . 70
5.2 Pseudo Experiment Test . . . 72
5.3 Systematic Uncertainty . . . 76
5.4 Forward-Backward Asymmetry in the Data . . . 83

6 A Search for Z' **87**
6.1 Z' Production . . . 88
6.2 Signal Modeling . . . 90
6.3 Background . . . 92
6.4 Statistical Method . . . 95
6.5 Results . . . 99

7 Publication of Search for $Z' \to e^+e^-$ **101**

8 Conclusion **108**

A Glossary **111**

Bibliography **113**

List of Tables

1.1 The coupling constants in the $Z \to f\bar{f}$ vertex in the tree level SM. . . 9
1.2 Coupling constants of E_6 Z' to fermions. 14
1.3 Coupling constants of general Z' bosons to the fermions. 15

3.1 Electron selection cuts. 44

4.1 Selection cuts for the electron template. 52
4.2 Selection cuts for the jet template. 54
4.3 Subtraction of the $W + jets$ events. 55
4.4 Estimation of di-jet background events. 57
4.5 Systematic and statistical uncertainties to the background estimation. 65
4.6 Electroweak background estimated from Monte Carlo simulation. . . 68

5.1 Pseudo experiment test of the matrix inversion unfolding method. . . 73
5.2 The systematic uncertainties to the A_{FB} measurement. 81
5.3 Numbers of data and background events in each mass bins. 84

6.1 Summary of expected backgrounds to the Z' search. 95
6.2 The observed 95 % confidence level lower limits on $M_{Z'}$ for chosen Z' models. 99

List of Figures

1.1 The Higgs potential $V(\phi)$. 7
1.2 Radiative corrections to the Higgs mass. 9
1.3 The Collins-Soper frame. 11
1.4 Z' search at CDF and D0 with Run I data. 16

2.1 Accelerator chain at Fermilab. 18
2.2 A side view of the CDF II detector. 21
2.3 The COT superlayers. 23
2.4 The calorimeter system of CDF Run II. 25
2.5 Data flow at CDF. 27
2.6 CDF Trigger system. 28
2.7 Software architecture of the Consumer Server/Logger (CSL). 30

3.1 The distributions of EM E_T and track P_T. 38
3.2 The distributions of E/P and track z_0. 39
3.3 The distributions of Had/EM and isolation. 40
3.4 The distributions of L_{shr} and PEM $\chi^2_{3\text{ x }3}$. 41
3.5 Global energy scale correction. 46
3.6 Di-electron mass distribution. 47
3.7 $\cos\theta^*$ distribution. 48

4.1 A schematic diagram of the isolation distributions of electrons and jets. 50
4.2 Isolation fit result with the CC events. 58
4.3 Isolation fit result with the CP events below the Z pole. 59

4.4 Isolation fit result with the CP events above the Z pole. 60
4.5 The di-jet invariant mass distribution. 61
4.6 Jet clustering and electron clustering. 62
4.7 Normalized di-jet mass distribution. 63
4.8 Estimation of systematic uncertainty to the di-jet background. 66
4.9 A_{FB} of the electroweak background. 68

5.1 The response matrix. 74
5.2 Pseudo experiment test of the matrix inversion unfolding method. . . 75
5.3 The uncertainties in the energy scale and the resolution. 77
5.4 Determination of the central material uncertainty with the E/P distribution. 79
5.5 PDF systematics. 82
5.6 The A_{FB} measurement with the data of 364 pb^{-1}. 85
5.7 The A_{FB} measurement with the data of 364 pb^{-1} around the Z pole. 86

6.1 A diagram showing the definition of the acceptance matrix A_{ij}. . . . 91
6.2 Invariant mass distribution of the data compared to the prediction. . 93
6.3 $\cos\theta^*$ distribution of the data compared to the prediction. 94
6.4 The distributions of test statistics Q from pseudo-experiments. 97
6.5 Exclusion contours for the Z' model-lines $B-xL$, $10+x\bar{5}$, $d-xu$, and $q+xu$. 100

8.1 The expected Z' signature at the ATLAS experiment. 109
8.2 Parton-level forward-backward asymmetries for $u\bar{u} \to e^+e^-$. 110

Introduction

The Standard Model (SM) describes the current understanding of the microscopic phenomena of elementary particles. The SM has been tested extensively by experiments and no compelling evidence against the model has been found so far [1] [31]. The SM consists of three generations of quarks and leptons.

$$\begin{pmatrix} u & c & t \\ d & s & b \end{pmatrix}, \qquad \begin{pmatrix} \nu_e & \nu_\mu & \nu_\tau \\ e & \mu & \tau \end{pmatrix}$$

These spin 1/2 particles are ruled by Fermi statistics and called fermions. The light quarks, predominantly u and d, are the constituents of protons and neutrons which make up nuclei of atoms. Heavier quarks are unstable and they can exist only temporarily before decaying to lighter particles. Out of six leptons, only the electron is a constituent of atoms, while the others are either unstable or very weakly interacting. The three columns of pairs of quarks and those of leptons represent the three generations of fundamental particles, which are identical except in mass. The existence of or numbers of generations is not predicted or understood.

To date, it is thought that there are four fundamental interactions between the elementary particles. The SM explains the strong, weak and electromagnetic interactions as an exchange of gauge bosons, or force carrying particles. The theory of electromagnetic interaction, which binds nuclei and electrons, is called quantum

[1] Neutrino mass however does add new features to the SM.

electrodynamics (QED), and the interaction is mediated by a massless photon. The strong interaction, which confines quarks into "color neutral" hadrons without long range strong interactions, is described by quantum chromodynamics (QCD). The force carriers of QCD are massless gluons. The weak interaction is mediated by massive vector bosons, W^+, W^-, and Z, and is the mechanism by which heavy quarks and charged leptons decay. The electromagnetic and weak interactions are described in a unified way by the electroweak theory [33].

The explanation of the interactions in the SM is based upon the local gauge symmetry of the Lagrangian [34]. As will be seen in the next chapter, the symmetry requires the mass of the particles to be generated dynamically. The minimal mass generation scenario requires the existence of a massive spin zero particle, or Higgs boson [24, 19, 20]. The Higgs boson is the only SM particle that is not discovered yet. The direct observation of Higgs boson is an important goal of current and future collider experiments.

The combined theoretical and experimental bounds for the Higgs mass are 114 GeV/c^2 $\lesssim m_H \lesssim$ 251 GeV/c^2 [9]. However a quantum correction to the Higgs mass is very large unless the correction is cancelled by contributions from new physics processes. One way of addressing the problem is a search for the direct signal of a new particle at around 1 TeV scale. Another approach is precision measurements of the SM expectations or detection of any deviation from the SM, which is the topic of this thesis. The analysis presented in this paper is based upon the final state that has two electrons e^+ and e^- produced through proton antiproton collisions at the Collider Detector at Fermilb (CDF). The di-electron final state is a very good channel for a precision measurement because the signal is very clean and the background is

well understood. For the same reason, the channel is also useful for a search for a new particle that decays into an electron pair. If there existed such a particle, the distribution of the kinematic variables of the electrons would deviate from the expectation of the SM.

Chapter 1

Theory

1.1 Electroweak Theory of the Standard Model

The electroweak Lagrangian can be written in two parts as following. [6, 21]

$$\mathcal{L} = \mathcal{L}_{\text{symm}} + \mathcal{L}_{\text{Higgs}} \tag{1.1}$$

The first part $\mathcal{L}_{\text{symm}}$ describes the fermion fields and their electroweak interactions:

$$\mathcal{L}_{\text{symm}} = -\frac{1}{4}\sum_{a=1}^{3} F^a_{\mu\nu}F^{\mu\nu a} - \frac{1}{4}B_{\mu\nu}B^{\mu\nu} + \bar{\psi}_L i\gamma^\mu D_\mu \psi_L + \bar{\psi}_R i\gamma^\mu D_\mu \psi_R, \tag{1.2}$$

where ψ is a sum over all flavors of quarks and leptons. The first two terms are Yang-Mills Lagrangian for the gauge group $SU(2) \otimes U(1)$. The weak isospin field strength tensor $F^a_{\mu\nu}$ is constructed out of the gauge field W^a_μ corresponding to the three $SU(2)$ generators:

$$F^a_{\mu\nu} = \partial_\mu W^a_\nu - \partial_\nu W^a_\mu - \epsilon^{abc} W^b_\mu W^c_\nu, \qquad a, b, c = 1, 2, 3, \tag{1.3}$$

where ϵ^{abc} is the $SU(2)$ group structure function. The hypercharge field strength is constructed from $U(1)$ gauge field B_μ:

$$B_{\mu\nu} = \partial_\mu B_\nu - \partial_\nu B_\mu. \tag{1.4}$$

The other two terms are the fermion matter fields. The subscripts L and R denotes two chirality states of the fermions that behave differently under the gauge group $SU(2)$. The left-handed and right-handed components are selected by the projection operators,

$$\psi_{L,R} = \frac{(1 \mp \gamma_5)}{2}\psi, \qquad \bar{\psi}_{L,R} = \bar{\psi}\frac{(1 \pm \gamma_5)}{2}. \tag{1.5}$$

The covariant derivatives $D_\mu \psi_{L,R}$ are given by

$$D_\mu \psi_{L,R} = \left[\partial_\mu + ig\sum_{a=1}^{3} T^a_{L,R} W^a_\mu + ig'\frac{1}{2}Y_{L,R}B_\mu\right]\psi_{L,R}, \tag{1.6}$$

where $T^a_{L,R}$ and $\frac{1}{2}Y_{L,R}$ are the $SU(2)$ and $U(1)$ generators and g and g' are the dimensionless coupling constants for weak isospin and hypercharge. The $SU(2)$ generators satisfy the commutation relation

$$[T^a_{L,R},\ T^b_{L,R}] = i\epsilon_{abc}T^c_{L,R}. \tag{1.7}$$

The generator of a $U(1)_{em}$ symmetry group of electromagnetic interaction is given by

$$Q = T^3_{L,R} + \frac{1}{2}Y_{L,R}, \tag{1.8}$$

and is referred to as an electric charge operator.

The vertex factors can be derived from the Eqs. (1.2) and (1.6). The charged-current vertex is

$$V_{\bar{\psi}\psi W} = g\bar{\psi}\gamma_\mu[(T^+_L/\sqrt{2})(1-\gamma_5)/2 + (T^+_R/\sqrt{2})(1+\gamma_5)/2]\psi W^-_\mu + h.c, \tag{1.9}$$

where $T^\pm = T^1 \pm iT^2$ and $W^\pm = (W^1 \pm iW^2)/\sqrt{2}$. The neutral-current is mediated by two mass eigenstates formed by linear combinations of B_μ and W^3_μ:

$$A_\mu = \cos\theta_W B_\mu + \sin\theta_W W^3_\mu, \tag{1.10}$$

$$Z_\mu = -\sin\theta_W B_\mu + \cos\theta_W W^3_\mu, \tag{1.11}$$

where A_μ is the massless photon field, Z_μ is the massive gauge boson field, and θ_W is the weak mixing angle. The photon has the same couplings to the left and right handed fermions with strength equal to e. From the Eqs. (1.8) and (1.11), we obtain

$$g \sin\theta_W = g' \cos\theta_W = e. \tag{1.12}$$

With the parameters determined by the experiments, Z couplings can be derived as

$$V_{\bar{\psi}\psi Z} = g/(2\cos\theta_W)\bar{\psi}\gamma_\mu[T_L^3(1-\gamma_5) + T_R^3(1+\gamma_5) - 2Q\sin^2\theta_W]\psi Z^\mu, \tag{1.13}$$

where $T_R^3 = 0$ and $T_L^3 = \pm 1/2$.

In the SM, all ψ_R are weak singlets and all ψ_L are weak doublets. Therefore mass terms for fermions such as $\bar{\psi}_L\psi_R$ are forbidden. Fermion masses are dynamically generated through the electroweak symmetry breaking. The minimal model of the mass generation requires a spin zero Higgs boson [24, 19, 20]. The Higgs sector of the electroweak Lagrangian is:

$$\mathcal{L}_{\text{Higgs}} = (D_\mu\phi)^\dagger(D^\mu\phi) - V(\phi^\dagger\phi) - \bar{\psi}_L\Gamma\psi_R\phi - \bar{\psi}_R\Gamma^\dagger\psi_L\phi^\dagger, \tag{1.14}$$

where ϕ is the Higgs scalar field. The potential $V(\phi^\dagger\phi)$ is given by

$$V(\phi^\dagger\phi) = -\frac{1}{2}\mu^2\phi^\dagger\phi + \frac{1}{4}\lambda(\phi^\dagger\phi)^2. \tag{1.15}$$

Spontaneous symmetry breaking occurs when the signs of μ^2 and λ are positive (Fig. 1.1). The vacuum expectation value of ϕ is denoted by v:

$$< 0|\phi(x)|0 >= v > 0. \tag{1.16}$$

Substituting the vacuum expectation value v for $\phi(x)$, the fermion mass matrix is given by

$$M = \bar{\psi}_L\mathcal{M}\psi_R + \bar{\psi}_R\mathcal{M}^\dagger\psi_L, \tag{1.17}$$

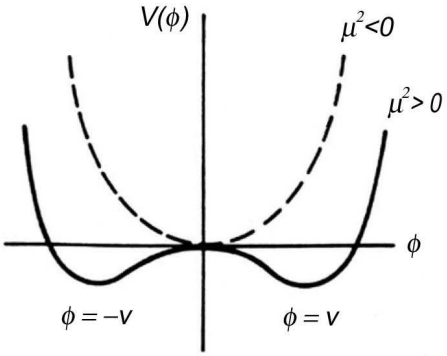

Figure 1.1: The Higgs potential $V(\phi)$. The potential has its minimum when $\phi = v \neq 0$.

where $\mathcal{M} = \Gamma \cdot v$. Since Γ is arbitrary, the fermion mass is not predicted by the SM.

The gauge boson masses are derived from the term $(D_\mu\phi)^\dagger(D^\mu\phi)$ in $\mathcal{L}_{\text{Higgs}}$, where

$$D_\mu\phi = \left[\partial_\mu + ig\sum_{a=1}^{3} T^a W_\mu^a + ig'(Y/2)B_\mu\right]\phi. \tag{1.18}$$

The charged W boson mass is identified by the quadratic terms in W field in $\mathcal{L}_{\text{Higgs}}$ with the substitution $\phi(x) \to v$:

$$m_W^2 W_\mu^+ W^{-\mu} = g^2|(T^+ v/\sqrt{2})|^2 W_\mu^+ W^{-\mu}. \tag{1.19}$$

For Higgs doublets,

$$\phi = \begin{pmatrix} \phi^+ \\ \phi^0 \end{pmatrix}, \qquad v = \begin{pmatrix} 0 \\ v \end{pmatrix}, \tag{1.20}$$

and the W mass is given by

$$m_W^2 = 1/2 g^2 v^2. \tag{1.21}$$

The relevant term for the Z mass is

$$\frac{1}{2}m_Z^2 Z_\mu Z^\mu = |\ [g\cos\theta_W T^3 - g'\sin\theta_W (Y/2)]v\ |^2 Z_\mu Z^\mu, \tag{1.22}$$

and it follows that

$$m_Z^2 = 1/2 g^2 v^2/\cos^2\theta_W. \tag{1.23}$$

The Higgs mass is $m_H^2 \sim \lambda v^2$, where $v = 174$ GeV is measured from properties of the weak interactions. λ is not fixed, leaving the Higgs mass a free parameter in the SM. Direct searches for the Higgs boson at LEP II experiments set the lower mass limit $m_H \gtrsim 114$ GeV/c^2. Indirect indications from the precision measurements imply the upper bound of the Higgs mass $m_H \lesssim 251$ GeV/c^2, if the SM is valid. However the SM has a problem with a loop correction (Fig. 1.2) to the Higgs mass. The correction to the tree-level mass is quadratically divergent [13]:

$$\delta m_H^2 \approx \frac{G_F}{4\pi^2\sqrt{2}}\Lambda^2(6m_W^2 + 3m_Z^2 + m_H^2 - 12m_t^2) \tag{1.24}$$

$$= -\left(\frac{\Lambda}{1 \text{ TeV}}\ 300 \text{ GeV}\right)^2, \tag{1.25}$$

where Λ is the next higher scale in the theory, above which this formula becomes invalid with new processes accessible at this scale. If the scale is assumed to be the Planck scale, the correction becomes much larger than what is thought to be natural, requiring a fine tuning. This problem implies the existence of new physics at 1 TeV scale [27]. An important goal of the current and future hadron collider experiments is to address this problem by precision measurements of the SM and searches for new processes. This paper presents one of the SM precision measurements with $Z \to e^+e^-$ decay channel and a search for an extra neutral gauge boson.

1.2 Z Boson

The vertex factor for the Z boson and a fermion pair (Eq. 1.13) can be written as following.

$$V_{\bar{f}fZ} = g/(2\cos\theta_W)\bar{\psi}_f\gamma_\mu[c_V^f - c_A^f\gamma^5]\psi_f Z^\mu, \tag{1.26}$$

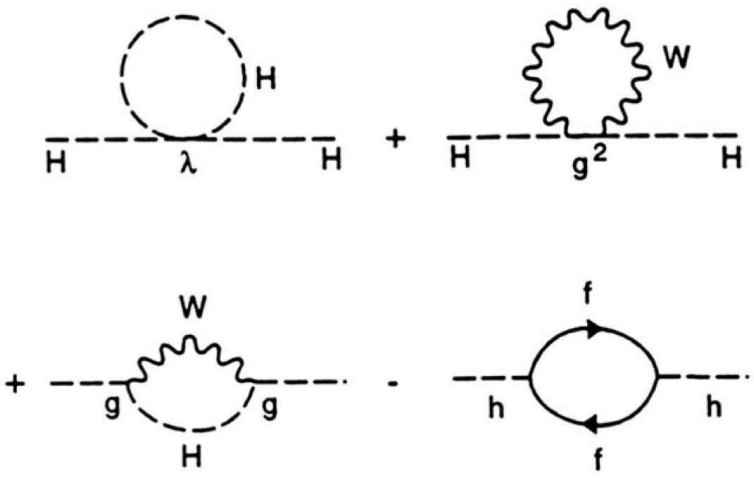

Figure 1.2: Radiative corrections to the Higgs mass.

where f denotes the flavor of the fermion, $c_V^f = T_f^3$ and $c_A^f = T_f^3 - 2\sin^2\theta_W Q_f$ are the vector and axial vector coupling constants (Table 1.1). The presence of both vector and axial-vector components gives rise to an asymmetry in the polar angle of the outgoing lepton in the rest frame of the fermion pair.

At a hadron collider, the process $p\bar{p} \to l^+l^-X$ is induced by a $q\bar{q}$ annihilation and mediated by an interference between the photon γ and Z boson exchange. The differential cross section of $q\bar{q} \to l^+l^-$ can be written in terms of the lepton scattering

f	T_f^3	Q_f	c_A^f	c_V^f
$\nu_e,\ \nu_\mu,\ \nu_\tau$	$\frac{1}{2}$	0	$\frac{1}{2}$	$\frac{1}{2}$
$e^-,\ \mu^-,\ \tau^-$	$-\frac{1}{2}$	-1	$-\frac{1}{2}$	$-\frac{1}{2} + 2\sin^2\theta_W$
$u,\ c,\ t$	$\frac{1}{2}$	$\frac{2}{3}$	$\frac{1}{2}$	$\frac{1}{2} - \frac{4}{3}\sin^2\theta_W$
$d,\ s,\ b$	$-\frac{1}{2}$	$-\frac{1}{3}$	$-\frac{1}{2}$	$-\frac{1}{2} + \frac{2}{3}\sin^2\theta_W$

Table 1.1: The coupling constants in the $Z \to f\bar{f}$ vertex in the tree level SM.

angle θ as follows

$$\frac{d\hat{\sigma}}{d\cos\theta}(q\bar{q} \to l^+l^-) = \frac{4\pi\alpha^2}{3s}\left[\frac{3}{8}A(1+\cos^2\theta) + B\cos\theta\right], \tag{1.27}$$

where

$$\begin{aligned} A &= Q_l^2Q_q^2 + 2Q_lQ_qg_V^qg_V^lRe(\chi(s)) + {g_V^l}^2({g_V^q}^2 + {g_A^q}^2)|\chi(s)|^2 + {g_A^l}^2({g_V^q}^2 + {g_A^q}^2)|\chi(s)|^2, \\ B &= \frac{3}{2}g_A^qg_A^l(Q_lQ_qRe(\chi(s)) + 2g_V^qg_V^l|\chi(s)|^2), \\ \chi(s) &= \frac{1}{\cos^2\theta_W\sin^2\theta_W}\frac{s}{s - M_Z^2 + i\Gamma_ZM_Z}, \end{aligned}$$

$Q_{l,q}$ is the electric charge of the lepton or quark, and s is the center-of-mass energy of the incoming $q\bar{q}$ system. The angular asymmetry is measured by the forward-backward asymmetry A_{FB}, which is defined as the following.

$$A_{FB} = \frac{\int_0^{+1}\frac{d\sigma}{d\cos\theta}d\cos\theta + \int_{-1}^{0}\frac{d\sigma}{d\cos\theta}d\cos\theta}{\int_{-1}^{+1}\frac{d\sigma}{d\cos\theta}d\cos\theta} = \frac{B}{A}. \tag{1.28}$$

Therefore a measurement of A_{FB} is a direct probe of the relative strength of the vector and axial-vector structure of the electroweak interaction.

The momentum of a parton in the initial state is a fraction of proton or antiproton momentum and can only be determined statistically. The momentum fraction x of a parton q out of a proton follows the parton distribution function $f_q(x)$. Therefore the cross section for the process $p\bar{p} \to \gamma^*/Z + X \to e^+e^- + X$ is given by integral of the parton level cross section with respect to the momentum fractions of partons, and summing over the flavors of the incoming partons:

$$\frac{d\sigma}{d\cos\theta}(p\bar{p} \to e^+e^-X) = \sum_q \int_{x_1}\int_{x_2} dx_1dx_2f_q(x_1)f_{\bar{q}}(x_2)\frac{d\hat{\sigma}}{d\cos\theta}(q\bar{q} \to l^+l^-). \tag{1.29}$$

If the incoming quarks had no transverse momentum, the scattering angle θ of the outgoing lepton can be simply measured from the axis of the incoming quarks.

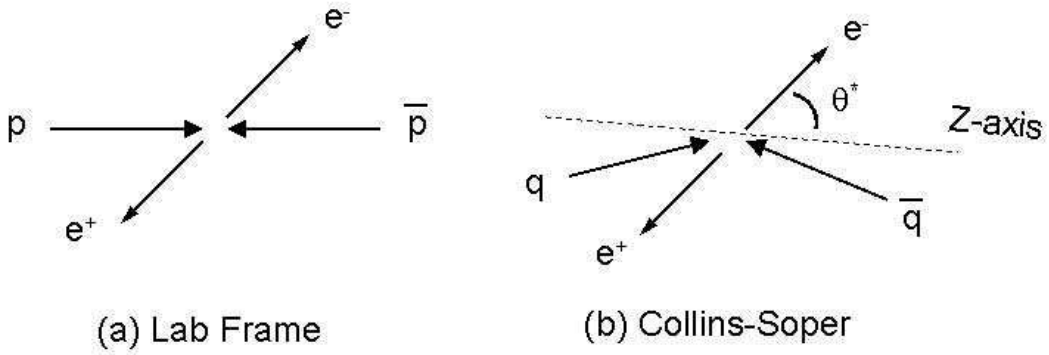

Figure 1.3: The Collins-Soper formalism minimizes the ambiguity of the event axis. The quarks come out of the proton and anti-proton with transverse momentum which is not measurable. By choosing the bisector of the proton and anti-proton beams, a new z-axis is define.

However, the partons can have transverse momentum that obscures the definition of the frame. Therefore we adopt the Collins-Soper formalism [18] to minimize the effect of the transverse momentum of the incoming quarks (Fig. 1.3). With the formalism, the polar axis is defined as the bisector of the proton beam momentum and the negative of the antiproton beam momentum when they are boosted into the center-of-mass frame of the electron-positron pair. The scattering angle of the outgoing electron θ^* is defined as the angle between the electron and the polar axis. Then $\cos\theta^*$ is given by

$$\cos\theta^* = \frac{2}{Q\sqrt{Q^2+Q_T^2}}(P_1^+P_2^- - P_1^-P_2^+), \tag{1.30}$$

where Q (Q_T) is the four momentum (transverse momentum) of the electron-positron pair. $P_i^\pm$ is defined to be $\frac{1}{\sqrt{2}}(P_i^0 \pm P_i^3)$, where P^0 and P^3 represent energy and the longitudinal components of the momentum, and $i = 1, 2$ represent electron and positron, respectively. Forward and backward events are defined by the sign of $\cos\theta^*$. The measurement of the forward-backward asymmetry as a function of di-electron invariant mass is the main topic of the thesis.

1.3 Extra Neutral Gauge Boson

The standard model describes the electroweak interaction in a unified way based upon the gauge group $SU(2)_L \times U(1)_Y$. The interactions are mediated by massive charged gauge bosons, W^+ and W^-, a massive neutral gauge boson, Z^0 and a massless photon γ. The $SU(2)_L \times U(1)_Y$ gauge theory has been remarkably successful in describing the experimental data and in demonstrating its predictive power. However, the $SU(2)_L \times U(1)_Y$ gauge group is not a complete unification because it consists of two gauge groups with different coupling strengths. Many theoretical models attempt to unify the interactions with a single coupling constant. Theories motivated by such an objective are called Grand Unifying Theories (GUT). Grand Unifying Theories typically extend the standard model gauge group by incorporating it in larger symmetries. If the new gauge group includes another $U(1)$ group, then there exists an electrically-neutral spin-1 particle, which is usually labeled Z'. The mass of the gauge bosons are generally not constrained by the theories, and in principle the mass can range from the electroweak scale to the Planck scale. To date, no compelling evidence for Z' bosons has been detected experimentally, and limits on their mass have been set.

E_6 is a possible choice for a GUT gauge group. Interest in the E_6 model has risen since it has been shown that E_6 is naturally incorporated in superstring theories as an effective GUT group. The E_6 group contains two extra $U(1)$ groups when its breaking leads to effective rank-6 groups at low energies. One possible breaking scenario is

$$E_6 \rightarrow SO(10) \times U(1)_\psi \tag{1.31}$$

$$\rightarrow SU(5) \times U(1)_\chi \times U(1)_\psi. \tag{1.32}$$

There arise two extra neutral gauge bosons associated with each extra $U(1)$ group. The mass eigenstates of Z' boson can be parameterized as linear combinations of two neutral gauge bosons Z_ψ and Z_χ. Assuming that the Z' mass eigenstates are not degenerate, we obtain the effective rank-5 model

$$E_6 \to SU(5) \times U(1)', \tag{1.33}$$

and the corresponding lowest mass Z' can be written most generally as

$$Z' = Z_\chi \cos\theta_{E_6} + Z_\psi \sin\theta_{E_6}, \tag{1.34}$$

where $0 \leq \theta_{E_6} < \pi$ is a mixing angle. Since the χ and ψ couplings are predicted by E_6 breaking, the angle θ_{E_6} determines the coupling constants of the Z'. When the E_6 group breaks, as in the Eq. (1.34), Z' is denoted as Z_η and $\theta_{E_6} = \tan^{-1}(\sqrt{3/5})$.

Another possible breaking scenario involves $E_6 \to SU(6) \times SU(2)_I$. The resulting Z' boson in this scenario, Z_I, turns out to correspond to a special case of the mixing scenario where $\theta_{E_6} = \tan^{-1}(-\sqrt{5/3})$.

The vertex for the Z' and fermion pair $f\bar{f}$ can be written as

$$V_{\bar{f}fZ'} = g_\theta \bar{\psi}_f \gamma_\mu [c_V^f - c_A^f \gamma^5] \psi_f Z'^\mu. \tag{1.35}$$

The left-handed and right-handed coupling constants $c_L^f \equiv c_V^f - c_A^f$ and $c_R^f \equiv c_V^f + c_A^f$ are shown in the Table 1.2 in terms of the following variables.

$$g_Z^2 \equiv \frac{e^2}{z(1-z)}, \tag{1.36}$$

$$g_\theta^2 \equiv \frac{5e^2}{3(1-z)}, \qquad z \equiv \sin^2\theta_W, \tag{1.37}$$

$$A \equiv \frac{\cos\theta_{E_6}}{2\sqrt{6}}, \qquad B \equiv \frac{\sin\theta_{E_6}}{2\sqrt{10}}. \tag{1.38}$$

Fermion	Coupling constant
u_L	-(A+B)
u_R	A+B
d_L	-(A+B)
d_R	A - 3B
e_L	3B - A
e_R	A+B

Table 1.2: Coupling constants of E_6 Z' to fermions.

In a recent study by Carena, Daleo, Dobrescu and Tait [16], the couplings are more generally expressed as first-order polynomials in a real number x. A number of constraints are applied in order to reduce the number of free parameters that describe a Z'. The constraints include the stringent limit on the $Z - Z'$ mixing, anomaly free, and no flavor changing neutral current. Four sets of solutions to the constraints are found, defining four types of Z' models: $B - xL$, $d - xu$, $q + xu$, and $10 + x\bar{5}$. Within each of these four model-lines, a certain Z' boson is specified by its mass $M_{Z'}$, the coupling strength $g_{Z'}$, and the value of x. This represents a drastic reduction in the number of parameters from the general Z' case and makes the study of the different Z' models tractable. The coupling constants is represented in terms of x as in the Table 1.3.

A direct search for Z' has been made with the Run I data of CDF and D0 [11]. Both the di-lepton invariant mass distribution and the forward-backward asymmetry distributions were investigated for any deviation from the standard model expectations (Fig. 1.4). A search for an extra neutral gauge boson with the CDF Run II data is described in chapter 6.

Fermion	Model-lines			
	$B - xL$	$q + xu$	$10 + x\bar{5}$	$d - xu$
u_L	$1/3$	$1/3$	$1/3$	0
u_R	$1/3$	$x/3$	-1/3	$-x/3$
d_L	$1/3$	$1/3$	$1/3$	0
d_R	$1/3$	$(2-x)/3$	$-x/3$	$1/3$
e_L	$-x$	-1	$x/3$	$(-1+x)/3$
e_R	$-x$	$-(2+x)/3$	-1/3	$x/3$

Table 1.3: Coupling constants of general Z' bosons to the fermions.

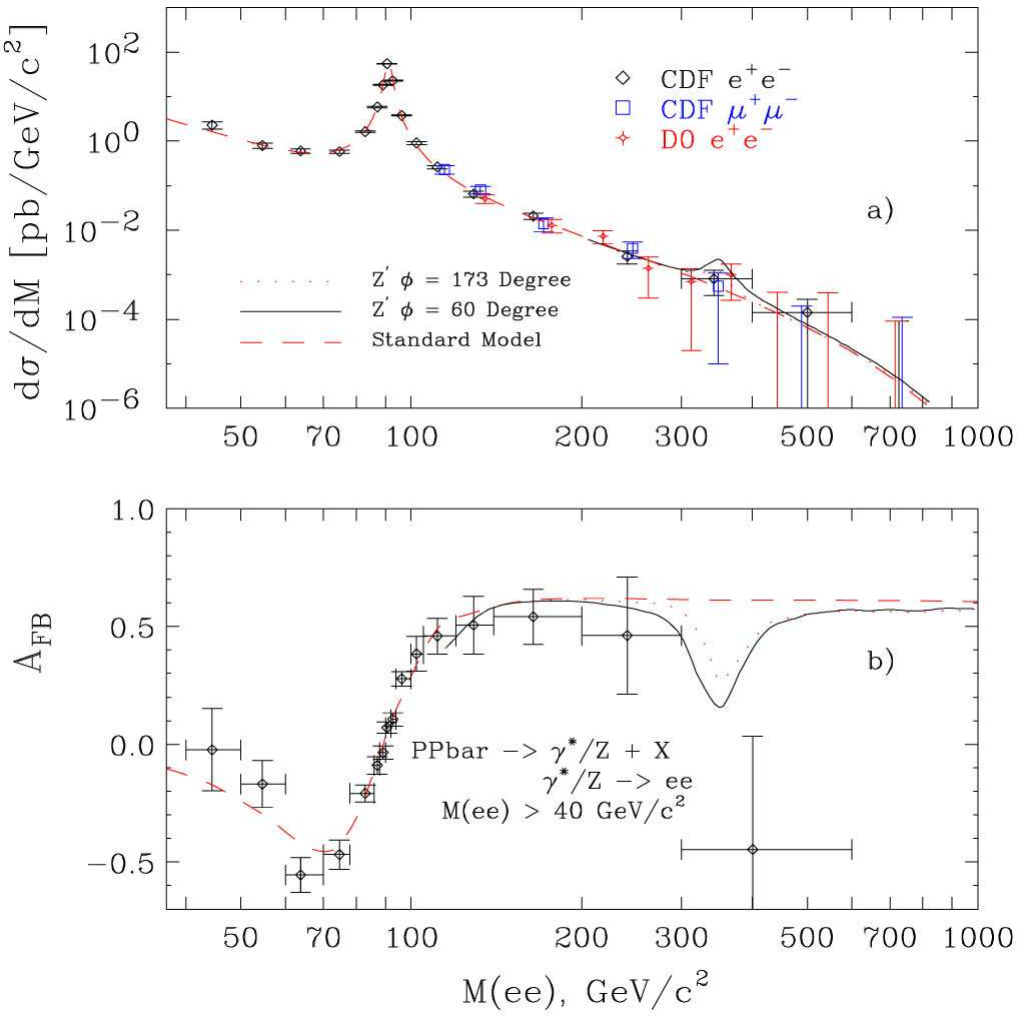

Figure 1.4: (a) $d\sigma/dM$ distribution of e^+e^- (CDF and D0) and $\mu^+\mu^-$ pairs (CDF). (b) CDF A_{FB} versus mass compared to the predicted theoretical curves for $d\sigma/dM$ and A_{FB} with an extra E_6 boson with $M_{Z'} = 350$ GeV/c^2 and $\Gamma_{Z'} = -0.1\ M_{Z'}$, for $\theta_{E_6} = 60°$ (solid) and $\theta_{E_6} = 173°$ (dotted).

Chapter 2

Apparatus

2.1 Accelerator

Phenomena at a very small scale can be studied by colliding highly energetic particles. At Fermi National Accelerator Laboratory (Fermilab), proton and anti-proton beams are accelerated and collided at a center of mass energy of 1.96 TeV. Acceleration is accomplished through five stages (Figure 6.1). First, negative hydrogen ions (H^-) are accelerated to a kinetic energy of 750 KeV in the Cockcroft-Walton accelerator and injected into the linear accelerator (Linac). The Linac accelerates the ions to an energy of 400 MeV and then passes the ions through a carbon foil to remove the electrons. Then the protons are fed into the Booster synchrotron, where the kinetic energy of the bunches is raised to 8 GeV. Subsequently the Main Injector accelerates the protons to 150 GeV, and feeds them into the Tevatron. In all stages except the electrostatic Cockcroft-Walton, acceleration is provided by application of radio frequency (RF) electric fields to the beam.

Antiprotons are generated by colliding a inconel alloy target with 150 GeV protons from the Main Injector. The resulting shower of the beams is focused into a beam line with a Lithium lens. Then the particles pass through a magnet which acts as a

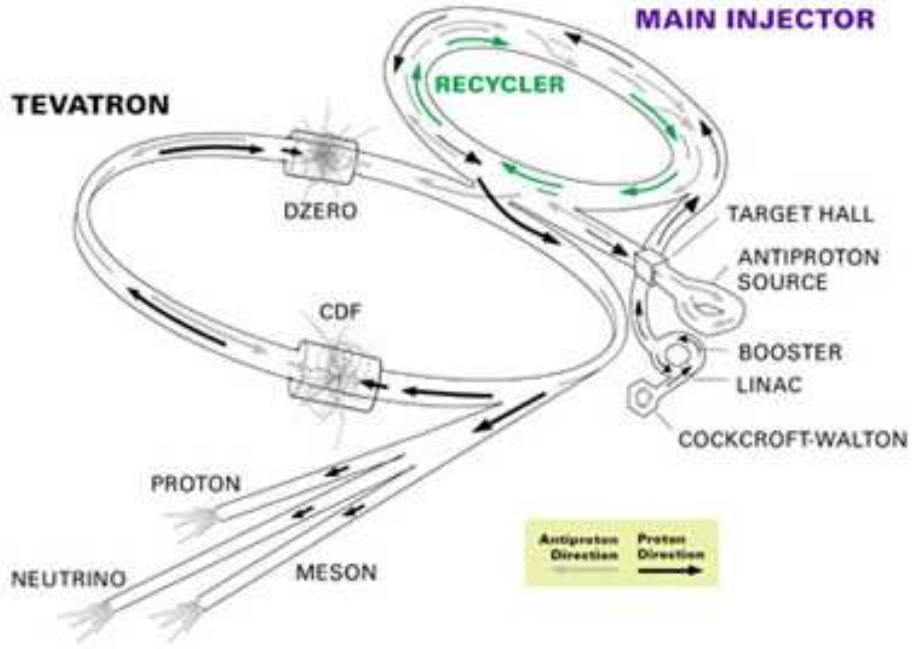

Figure 2.1: Accelerator chain at Fermilab. Tevatron has two collision points, CDF and D0. Beams can also be used for fixed target experiments.

charge-mass spectrometer, and antiprotons with an energy around 8 GeV are selected. The energy spread of the antiproton beam is reduced by the Debuncher, which instead enlarges the longitudinal spread of the bunches. Then the antiprotons are injected into the Accumulator and recycler ring for temporary storage. Both the Debuncher and the Accumulator reduce the momentum fluctuations within the bunches by applying negative feedback to the particles. The technique is called stochastic cooling. Accumulated antiprotons are transferred into the Main injector and accelerated to 150 GeV.

Bunches of protons and antiprotons are transferred from the Main Injector into the Tevatron in opposite directions, and accelerated further up to an energy of 980 GeV. The Tevatron is the last step of the chain that accelerates the particles up to an energy of 980 GeV. The particles are kept on the beamline of the Tevatron

by superconducting magnets cooled in liquid helium. Proton and antiproton beams travel on helical orbits that intersect with each other only at the collision points.

The rate of a physics process is proportional to the product of the luminosity and the cross section. The cross section is inherent quantity in each processes and can be calculated from the standard model. The luminosity measures the intensity of the beam and it is defined as

$$L = nf\frac{N_p N_{\bar{p}}}{4\pi\sigma_x\sigma_y}\ (\mathrm{cm}^{-2}\mathrm{s}^{-1}), \tag{2.1}$$

where n is the number of bunches, $f = 50$ kHz is the revolution frequency of a bunch traveling at the speed of light around the circumference of the Tevatron ring, N_p and $N_{\bar{p}}$ are the numbers of protons and antiprotons per bunch, respectively. σ_x and σ_y are the Gaussian beam profiles in the transverse plane, averaged over z. At a luminosity of 1.0×10^{32} $\mathrm{cm}^{-2}\mathrm{s}^{-1}$, there are about 10^{12} protons and about an order of magnitude fewer anti-protons per bunch.

Collisions are brought about by focusing the two beams with quadrupole magnets. At the collision point, the bunch cross section is roughly circular with a radius of 35 μm and the length along the beamline is about 35 cm. The period of time from the beginning of the collision to the termination of the beam is called a 'store'. A store is terminated when the bunches lose particles at collisions and the luminosity of the beams decrease. Each store can be as long as about 30 hours when there is no operational problem.

The typical luminosity during the period of Run I, the data taking period from 1992 and 1996, was $L = 1.6 \times 10^{31}$ $\mathrm{cm}^{-2}\mathrm{s}^{-1}$. The second data taking period, Run II, was started in June 2001 with the upgraded main injector, new anti-proton recycler and upgraded detector. The record instantaneous luminosity of Run II is $1.8 \times$

10^{32} cm^{-2}s^{-1}, recorded on February 14, 2006.

2.2 Collider Detector at Fermilab

The Collider Detector at Fermilab (CDF) is a general purpose particle detector which surrounds the point of the proton-antiproton collision, [2]. The first collision was observed in 1985 and Run I recorded the data of total integrated luminosity 110 pb^{-1}. Run II so far has recorded the data of 1 fb^{-1}, and it is expected to collect the data of between 4 and 9 fb^{-1} until the year 2009.

The CDF coordinate system is defined with the z direction along the proton beam direction. The y axis is chosen to be upward, and the x axis points outward from the Tevatron ring. The polar angle θ is measured from the z axis and the azimuthal angle ϕ from the x direction. The pseudorapidity is an angular coordinate defined as $\eta = -\ln(\tan\theta/2)$, so that $\Delta\eta$ is invariant under Lorentz boost along the z direction. The region with $0 < |\eta| < 1$ is called central, and the region with $|\eta| > 1$ is called plug or forward. The transverse plane is perpendicular to the z axis.

The CDF II detector consists of three major parts; tracking, calorimetry, and muon systems (Figure 2.2). The detector has both cylindrical and forward-backward symmetries. The innermost component of the CDF detector are the layers of silicon detectors for the precision measurement of the particle trajectory. The Central Outer Tracker (COT) [4] surrounds the silicon tracking system and records the trajectory of the charged particles. The COT is surrounded by a super-conducting solenoid of radius 1.5 m that provides 1.4 Tesla of magnetic field parallel to the beam axis.

The calorimeter system surrounds the tracking system and covers 2π in azimuth and the pseudorapidity within $|\eta| < 3.64$. They are segmented to form a projective

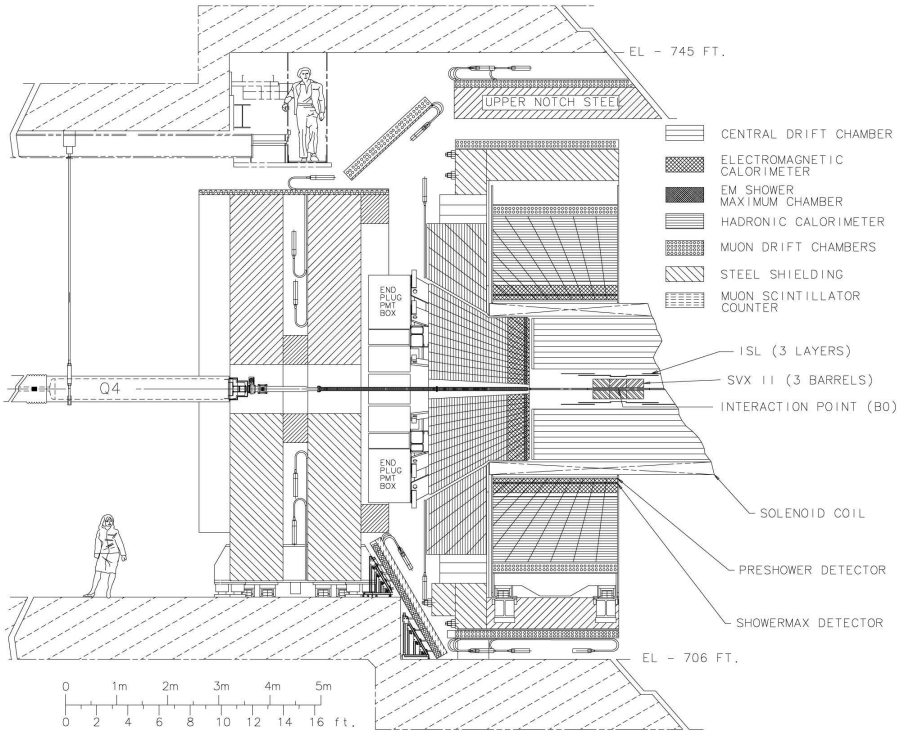

Figure 2.2: A half of the side view of the CDF II detector. The detector is cylindrically symmetric.

tower geometry which points back to the nominal interaction point. The calorimeter is separated into two sections. The central calorimeter is cylindrical, covering the region $|\eta| < 1.1$. The forward region is covered by the plug calorimeter, which covers $1.1 < |\eta| < 3.6$. Each region has an electromagnetic calorimeter and a hadronic calorimeter. The electromagnetic calorimeter consists of layers of lead absorber and plastic scintillator. The hadronic calorimeter consists of layers of steel absorber and plastic scintillator. The energy deposition is measured with photomultiplier tubes (PMT). The electromagnetic calorimeter is designed so that electrons and photons deposit most of their energies. Hadrons pass through the electromagnetic calorimeter with significant amount of energy and their energy is measured by the hadronic

calorimeter.

Finally, muons are detected by the muon chambers which comprise the outermost layer of the detector. Neutrinos escape the detector without an interaction and their energy is measured from the imbalance in the vector sum of the detected energy. Electrons consist of the final state of the analysis described in this paper. The relevant detector components are the COT and the electromagnetic calorimeter which are described in more detail in the following sections.

2.2.1 Central Outer Tracker

The COT is a cylindrical open-cell drift chamber with inner and outer radii of 44 and 132 cm and 30,240 gold-plated tungsten wires are arranged as eight super-layers (Figure 2.3 (a)). It finds track of the charged particles in the region $|\eta| < 1$. A superconducting solenoid creates a 1.4 Tesla magnetic field along the $-z$ direction over the tracking region. The trajectory of a charged particle is curved in the $r - \phi$ plane by the magnetic field. The path is reconstructed as a helix and the momentum of the particle is determined from the curvature of the track from the following relation.

$$P \text{ (GeV/c)} = 0.3 \; B \; r \text{ (Tesla} \cdot \text{cm)}, \tag{2.2}$$

in the units of electron charge, where B is the strength of the magnetic field and r is the radius of curvature.

The wires in four axial super-layers run parallel to the beamline and provide position information in $r - \phi$ coordinates. The other four superlayers are tilted by 2° with respect to the z direction. Each super layer is subdivided into cells which contain 12 sense wires, alternated with 13 potential wires which shape the electric field within the cell (Figure 2.3 (b)). The wire spacing is about 7.5 mm.

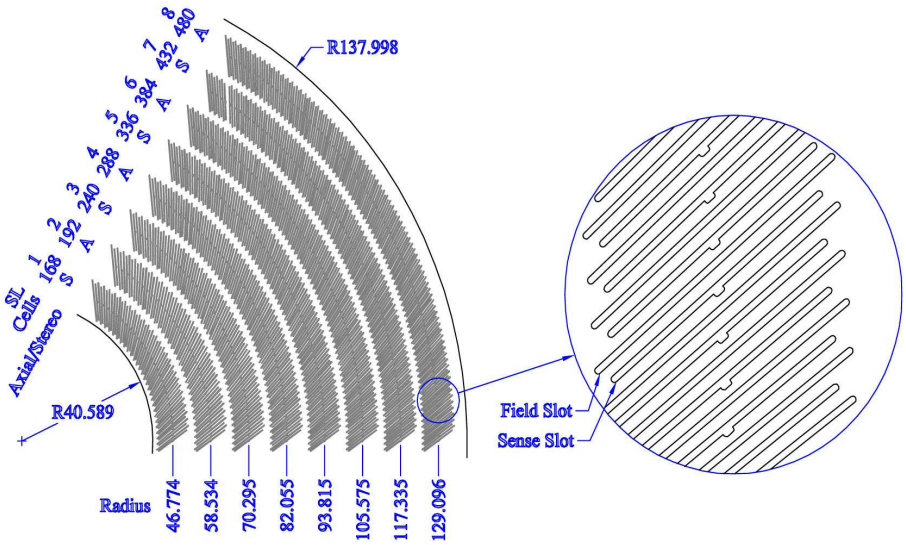

(a)

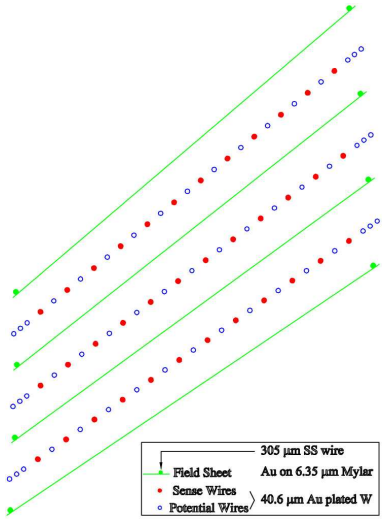

(b)

Figure 2.3: The COT superlayers. (a) 1/6 of the COT cross section. (b) Three cells which are tilted by 37° to compensate for the magnetic field and keep the drift path linear.

The wires are contained in a chamber which is filled with argon (50 %) and ethane (50 %) gases. Charged particles passing through the COT drift chamber ionize the gas molecules. The avalanche of the electrons from the ionization drift onto the sense wires and generate electric signals. The maximum drift time is about 100 ns, which is less than the bunch spacing of 396 ns. The drift time is converted to a pathlength. The COT resolution of the transverse momentum is $\Delta P_T/P_T^2 < 0.15$ % GeV/c, which leads to 1 % of charge fake probability at the energy of 200 GeV.

2.2.2 Electromagnetic Calorimeter

As an electron or photon enters the calorimeter, it interacts with the heavy material generating a shower of photons and electron pairs. The shower crosses the scintillating material and excites the atoms of the scintillator which then radiate photons as they return to their ground state. The photons are collected through acrylic light guides leading to PMT. Integrating the charge collected in the PMT gives a measure of the energy deposited in the calorimeter.

The central electromagnetic calorimeter (CEM, [8]) is cylindrically symmetric, divided in half at $\eta = 0$. Each half of the calorimeter is segmented into 24 wedges of 15° in ϕ. Each wedge is divided into ten projective towers such that each tower has the width of $\Delta\phi = 0.1$ (Figure 2.4 (a)). A tower contains 31 layers of 0.125 inch lead interleaved with 5.0 mm polystyrene scintillator giving a total radiation length of 18 X_0. One radiation length, denoted by 'X_0', is the mean distance over which a high-energetic particle loses 67 % of its energy. The energy resolution of the CEM is measured to be $1.7\% + 13.5\%/\sqrt{E(\mathrm{GeV})}$.

At the location of the shower maximum ($6 \times X_0$), after the eighth layer of lead, a strip detector is installed into each wedge. A view of an edge of the central calorimeter

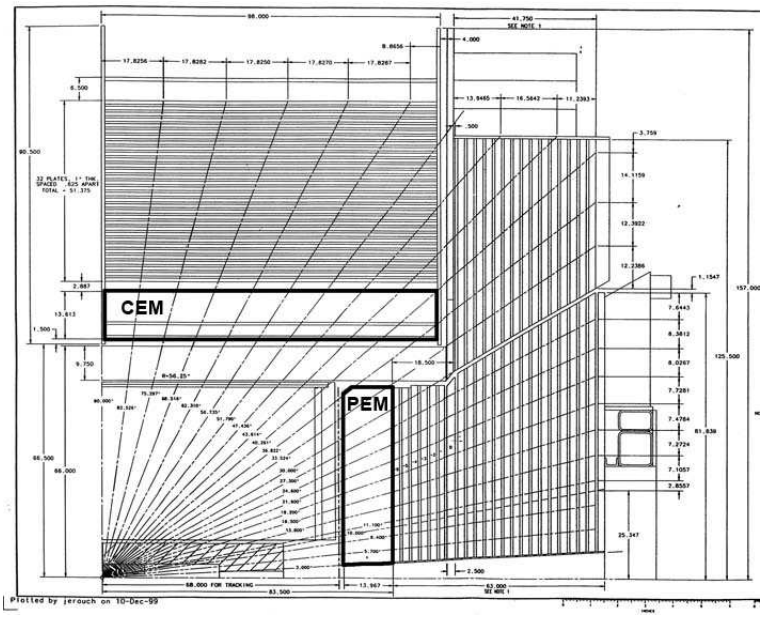

(a)

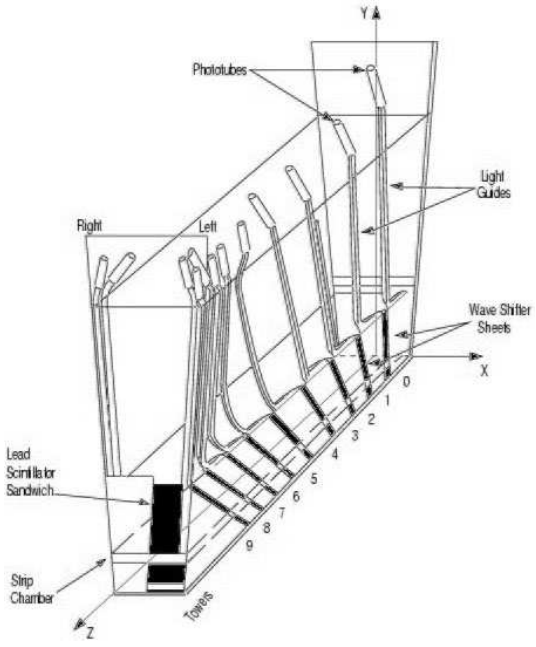

(b)

Figure 2.4: The calorimeter system of CDF Run II. (a) Half of CEM and PEM are shown. CEM covers $|\eta| < 1$ and PEM covers $1 < |\eta| < 3.6$. (b) A CEM wedge that covers 15° in ϕ.

is shown in Figure 2.4 (b). The shower maximum detector contains orthogonal strips and wires, with wires running parallel to the beam axis. The shower signal provides precise position information. In front of the CEM wedge is a proportional chamber, or the central preradiator (CPR). The CPR measures the soft shower profiles caused by the interaction of particles with the tracking material or the solenoid. The information is useful for discriminating between pions and electrons.

The plug electromagnetic calorimeter (PEM, [5]) is located in front of a hadronic calorimeter (Figure 2.4 (a)). The PEM is divided into wedges of 30° . Each wedge consists of 23 layers of lead and scintillator, which makes up a total radiation depth of 21 X_0. The energy resolution of PEM is $16\,\%/\sqrt{E(\mathrm{GeV})} + 1\,\%$. The shower maximum detector in the forward region is also located within the PEM at about $6X_0$. In front of the PEM is the plug preradiator (PPR) made of a layer of plastic scintillator, which plays a similar role as CPR.

2.3 Data Acquisition System

The rate of the proton anti-proton bunch crossing is every 396 ns or at 2.5 MHz. The events are filtered by the three-layered trigger system (Figure 2.5 and 2.6). The level 1 trigger is implemented by custom designed hardware. The electronics of each detector component is composed of a buffer of 42 pipelines. Uncalibrated data from the calorimeter, COT and the muon detector are fed into the pipelines. The decision time of the Level 1 trigger is about 4 μs and the decision is made before the pipeline goes through one cycle. The rate of the events out of the Level 1 trigger is below 20 kHz.

An event is then passed to the Level 2 trigger on a Level 1 accept. The data is

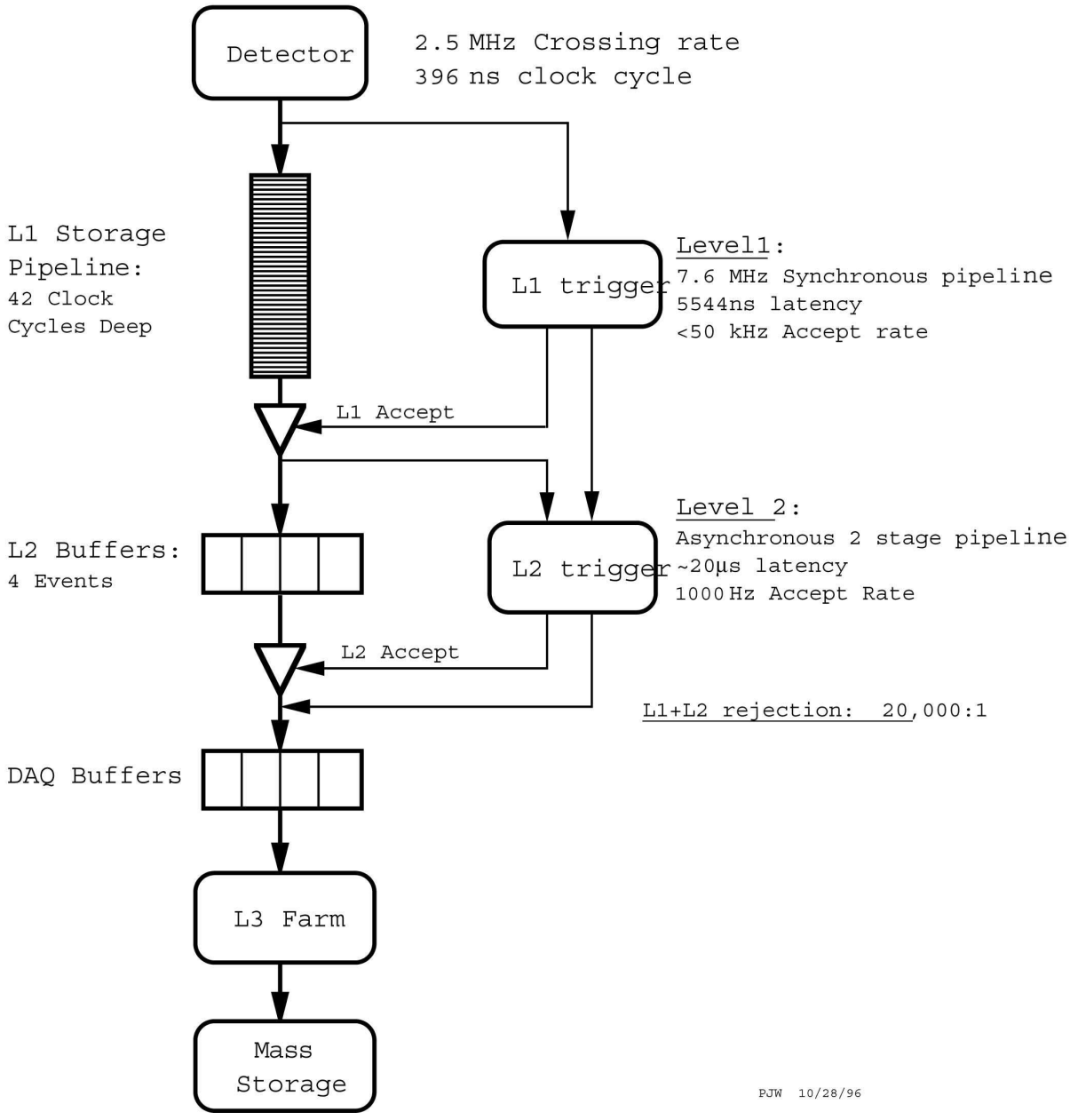

Figure 2.5: Data flow from the CDF detector to the mass storage system. Three layers of triggers filter the events 2.5 MHz down to about 100 Hz.

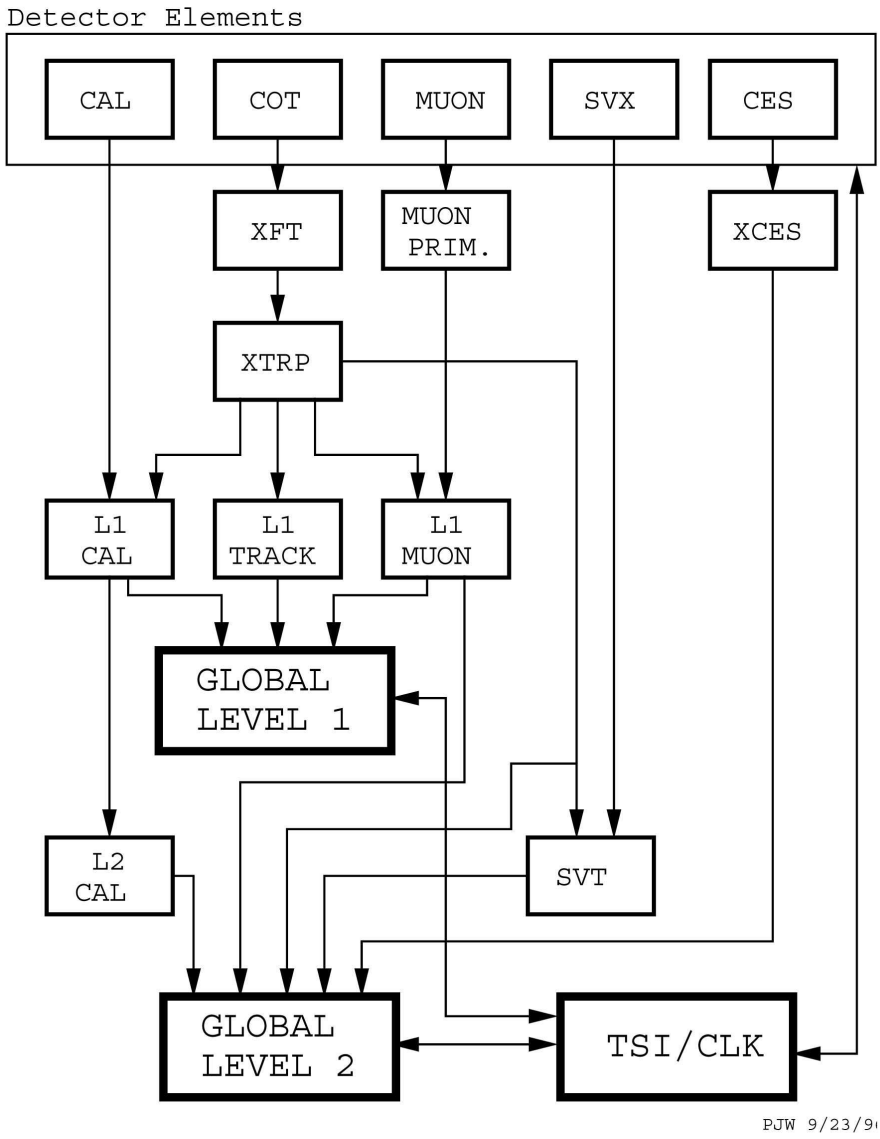

Figure 2.6: CDF Trigger system. The Level 1 decision is made based upon the calorimeter, COT and muon system. Enhanced calorimeter clustering and the silicon tracking are additionally available for the Level 2 decision.

written into one of four data buffers of each detector component. The Level 2 trigger decision is made in about 20 μs. The larger decision time of Level 2 allows the use of information such as shower maximum detectors and the silicon tracking information, in addition to all the data used for the Level 1 decision. The algorithm on the Level 2 decision provides higher granularity giving better resolution than at Level 1. For example, the Level 2 trigger reconstructs clusters of towers by adding the energies of the adjacent two towers. The Level 2 hardware also calculates total transverse energy and transverse missing energy. The Level 2 trigger is designed to work with a maximum accept rate of 1000 Hz.

Passing the Level 2 trigger, event fragments are combined into an event of about 150 KB on average. It is then passed to the Level 3 trigger system which consists of hundreds of Linux machines connected by an Ethernet network. The available decision time of the Level 3 trigger is about a second, allowing an almost complete reconstruction of an event with the offline software. At the Level 3 trigger, the calibration information is applied to the data to achieve the best possible resolution. Once an event is accepted, the event is compressed and sent to the mass storage system at a rate of about 100 Hz.

The Consumer Server/Logger (CSL) creates the raw data file and writes the events. The CSL is implemented by a SGI Origin 2000 series server with eight CPU's. The software structure on the CSL machine is shown in the Figure 2.7. For each Level 3 output nodes, a receiver process is forked. During the data taking, there are eight logger processes that write the eight streams of data into eight files. There are six external RAID disks of about 3 Terabytes attached to the CSL machine via Fiber Channel interface. Each RAID system consists of six SCSI disks which are configured

as RAID-3 for a redundancy that enables recovery of data in case of a disk failure.

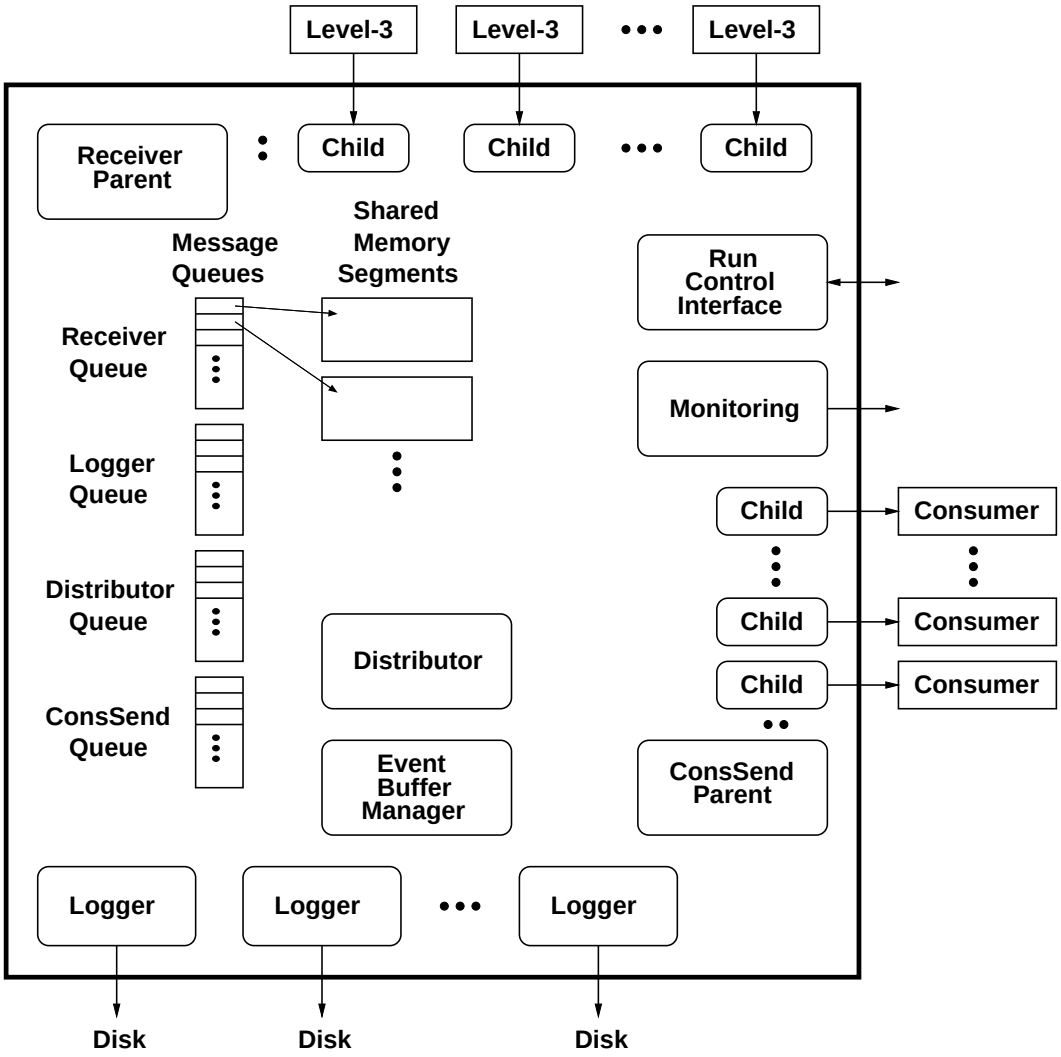

Figure 2.7: Software architecture of the Consumer Server/Logger (CSL). The events are stored in one of the shared memory segments and the interprocess communication is performed through the message queues.

Chapter 3

Data Sample

The analysis requires an electron and a positron in the final state. A central electron (e^+ or e^-) is reconstructed from the information recorded by CEM and COT detectors. The CEM gives information on the energy deposition of the electron, and COT measures the trajectory and the momentum of the electron. The combination of the two detectors provides a sample with high purity and very low background. The COT detector does not cover the plug region and therefore a matching track is not required if an electron is found in the plug region where $|\eta| > 1.0$. The events are required to have at least one good electron candidate in the central region, and the other electron is allowed to be either in the central or plug regions.

3.1 Electron Reconstruction

An EM object is a collection of variables designed to describe an electron or a photon, which deposits its energy through an electromagnetic shower in the calorimeter. An EM object is reconstructed through an algorithm which is seeded by an energy deposit in the electromagnetic calorimeter. An electron is selected by applying a set of cuts to the EM objects. The algorithm first orders the electromagnetic calorimeter towers

by the measured transverse energy (EM E_T). The tower with the highest EM E_T is selected as a seed for a cluster, if E_T is larger than the threshold 2 GeV. Transverse energy is calculated assuming that the event originates from the center of the detector with $z = 0$, until the position is corrected from the vertex found from the tracks. If the seed tower is in the central region of the detector, a tower that is adjacent in η is added to the cluster as a shoulder tower, if $E_T > 100$ MeV. If the cluster is in the plug region of the detector, adjacent towers with less energy deposits are added to the cluster, with the same threshold 100 MeV, so that the resulting size of the cluster is 2 x 2 towers.

The difference in the calorimeter response within each tower is corrected after the reconstruction. The response is determined by the test beam response to electrons entering at different points in the tower. The difference of response in different towers and the time dependence of the response are also corrected. The energy measured by the PPR is added to the plug electron energy to account for the energy loss before the electron reaches the calorimeter face.

Shower max detectors (CES in central and PES in plug) provide the position of an electron with high resolution. The central shower max CES consists of wires and strips in perpendicular directions in the $z - \phi$ coordinate. The channels are scanned for a signal above threshold. Up to 11 channels above threshold are added to a CES cluster. The plug shower max PES is constructed with two layers of scintillating strips, called U and V, which cross each other at 45°. A PES cluster is composed by up to nine channels with a signal above threshold. The profile of the shower shape is then compared to templates obtained from the test beam. The centroid of the shower max cluster is used as the location of the electron object.

The electron in the central region passes through the tracking chamber COT, which is 99.3 % efficient finding a track associated with a charged particle [25]. Three dimensional track information is reconstructed from the individual hits. After the reconstruction of all the tracks in an event, an attempt is made to find a matching track with the calorimeter cluster. The matching is determined by extrapolating the track position onto the plane of the CES. Finally, the transverse energy of an electron object is recalculated from the vertex of the track. A matching track is not required for plug electrons. The transverse energy of plug electrons are calculated from the event vertex, which is reconstructed from the high P_T COT tracks in an event.

3.2 Selection Variables

Event selection is made by applying a set of cuts to the variables associated with the electron candidates. The definitions of the variables that are used for the electron identification are listed below.

- CES Fiduciality

  Particles are required to pass the instrumented and active region of the detector. The location of the CES cluster is required to be within 21 cm in ϕ from the center of the wedge, and between 9 and 230 cm in the z direction.

- Track z_0

  The interaction point along the z direction of the beam line is found from the matching track to the central electromagnetic cluster. The position is required to be within 60 cm from the center of the detector, in order to ensure that the trajectory of the particle passes the tracking volume. This requirement is 95 %

efficient for the $Z \rightarrow e^+e^-$ events.

- E_T

  The electron transverse energy E_T is calculated as $E_T = E \times \sin\theta$ where E is the energy deposited in the calorimeter cluster and θ is the electron polar angle with respect to the beam line. The cluster in the central region consists of two calorimeter towers with highest energy depositions. In the plug region, a cluster is made of four towers in 2 x 2 geometry. The electron polar angle θ of a central electron is calculated from the vertex of the matching COT track. The vertex of a plug electron is calculated from the event vertex, which is reconstructed from the COT tracks in the event. E_T is required to be above a threshold, in order to distinguish it from underlying events and backgrounds.

- Had/EM

  Had/EM is the ratio of the energies deposited in the hadronic calorimeter and the electromagnetic calorimeter. A particle passes through the electromagnetic calorimeter first, and the depth of the electromagnetic calorimeter is designed so that most of the electron energy is absorbed. Therefore the ratio Had/EM is expected to be small if the particle is a real electron. On the other hand, heavier particles in hadronic jets tend to deposit smaller fractions of their energies in the electromagnetic calorimeter and deposit more energy in the hadronic calorimeter. Therefore by requiring Had/Em to be smaller than a cut value, electrons can be selected and the background objects can be rejected.

- Isolation

  A measure of how much an object in the calorimeter is free of other activities

in the nearby towers is defined as

$$\frac{E_T^{0.4} - E_T^{cluster}}{E_T^{cluster}},$$

where $E_T^{0.4}$ is sum of the transverse energy deposited in a cone of $\Delta R = \sqrt{\Delta\phi^2 + \Delta\eta^2} < 0.4$, centered at the location of the shower max, and $E_T^{cluster}$ is the energy deposited in the electron cluster. The isolation is zero when there is no extra activity in the calorimeter around the cluster, and becomes larger if there are other towers with energy deposits. From the Monte Carlo simulation studies, it is known that the electrons from Z decays are well isolated. Therefore requiring small isolation helps selecting electrons.

- P_T

  P_T is the transverse momentum calculated from the matching COT track to the central electron. The track P_T is required to be above a threshold value.

- E/P

  E/P is the ratio of the total energy and the track momentum. In the high energy limit, particles can be regarded as massless and the energy E would be equal to the magnitude of the three momentum P. However energetic electrons radiate photons as they pass through the detector material and the photons tend to recombine in the calorimeter towers where the electrons are absorbed. Then the track momentum would be measured to be less than the energy deposit, leading the E/P to be larger than 1.0. The shape of the tail of E/P distribution can be studied to extract the information on the amount of the material in the detector. The quantity is also used as electron selection variable, since the E/P of an electron tends to peak around 1.0. Real electrons can have low E/P

when P is mis-measured, especially when the momentum is high and the track curvature is large. A high E/P can occur when the momentum is lost through QED radiation, and the radiated photons recombine is the calorimeter tower. The E/P of the jet background is usually inconsistent with 1.0.

- CES - track match

  The matching track is extrapolated to the plane of CES detector, and the difference in the location is required to be within a tolerance. The difference in ϕ direction is denoted as Δx and the difference in z direction is denoted as Δz.

- L_{shr}

  A quantity that measures how the lateral shower shape resembles the shape expected from the test beam data. L_{shr} is defined in the central region only, as following.

$$L_{shr} = 0.14 \sum_i \frac{E_i^{adj} - E_i^{expected}}{\sqrt{(0.14\sqrt{E})^2 + (\sigma_{E_i^{expected}})^2}},$$

  where E_i^{adj} is the measured energy in the towers adjacent to the seed towers, and $E_i^{expected}$ is the expected energy in the tower calculated from the test beam data. $0.14\sqrt{E}$ and $\sigma_{E_i^{expected}}$ are the uncertainties of energy measurement and the expected energy, respectively.

- χ^2_{strip}

  The CES shower shape is compared to that of test beam data, in the z direction. The shape in the ϕ direction is easily distorted by the bremsstrahlung radiation and is not used for the identification. A χ^2 is calculated from the energies in

the 11 strips. An object with χ^2 larger than the cut value is rejected for the selection.

- PEM $\chi^2_{3\text{ x }3}$

  The shower profile in the plug region is compared to the test beam data for consistency. The energy deposition in the nine towers in 3 x 3 geometry around the seed tower is used for the calculation of χ^2. For the electron identification, the quantity is required to be below a cut value.

3.3 Monte Carlo Sample

12 million $p\bar{p} \rightarrow Z/\gamma \rightarrow e^+e^-$ events were generated by a Monte Carlo simulation program PYTHIA [32] version 6.216 for comparison with the data. The generator includes the interference between the virtual photon γ^* and the Z boson exchanges, as well as final state QED radiation. A parton distribution function CTEQ5L is used to describe the parton evolution prior to the hard scattering. The generated events were run through a CDF detector simulation and the offline reconstruction programs. The distributions of the selection variables are shown in Figs. 3.1 through 3.4, showing both the data and the Monte Carlo expectations. The excess of the data points beyond the selection cuts shows the background contamination in the data in those regions.

3.4 Trigger Requirements

The CDF detector incorporates three layers of triggers which filter the events during data taking. Currently there are about 170 trigger paths, each of which defines the requirements and pre-scale rates at each level of triggers. The detailed requirements

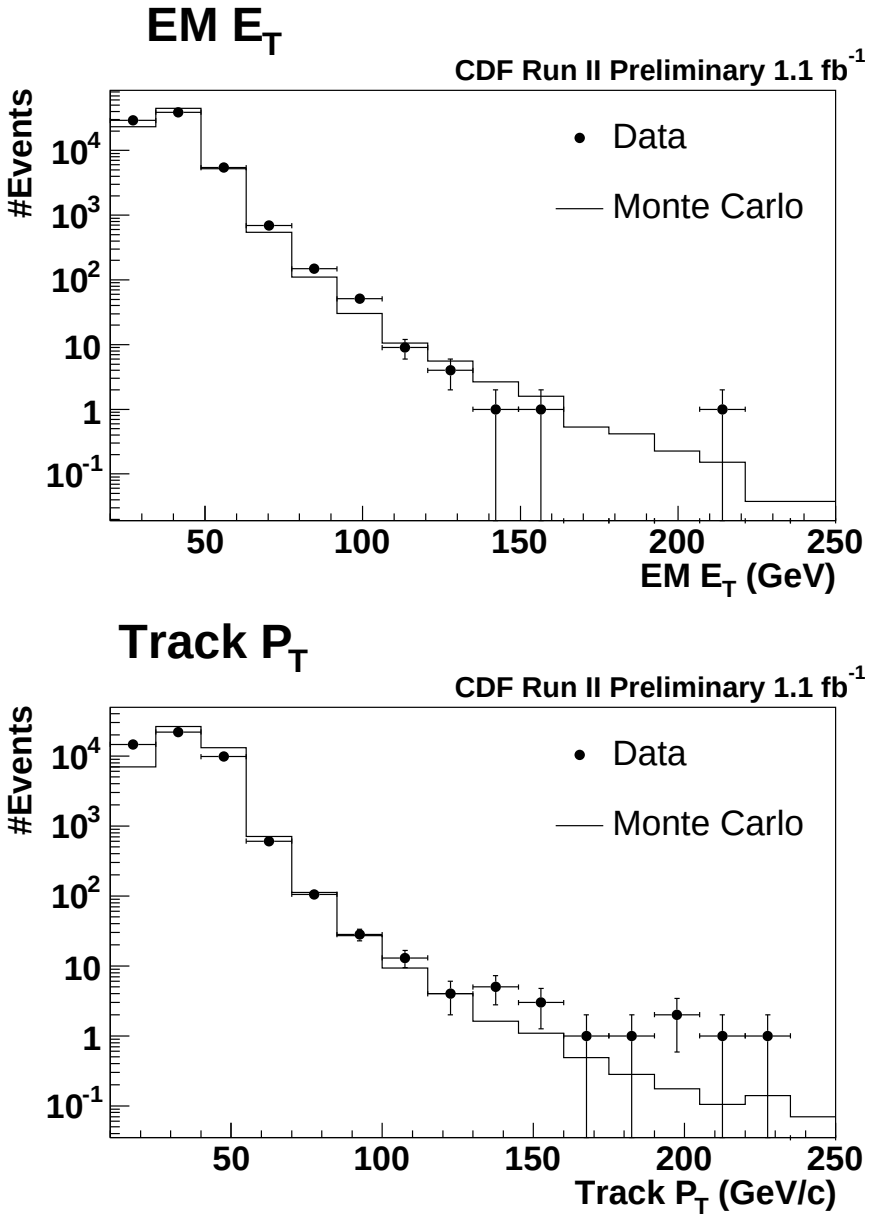

Figure 3.1: The distributions of EM E_T and track P_T. The data and Monte Carlo simulations are compared. The excess of the data points at high track P_T region shows the background contamination in the data.

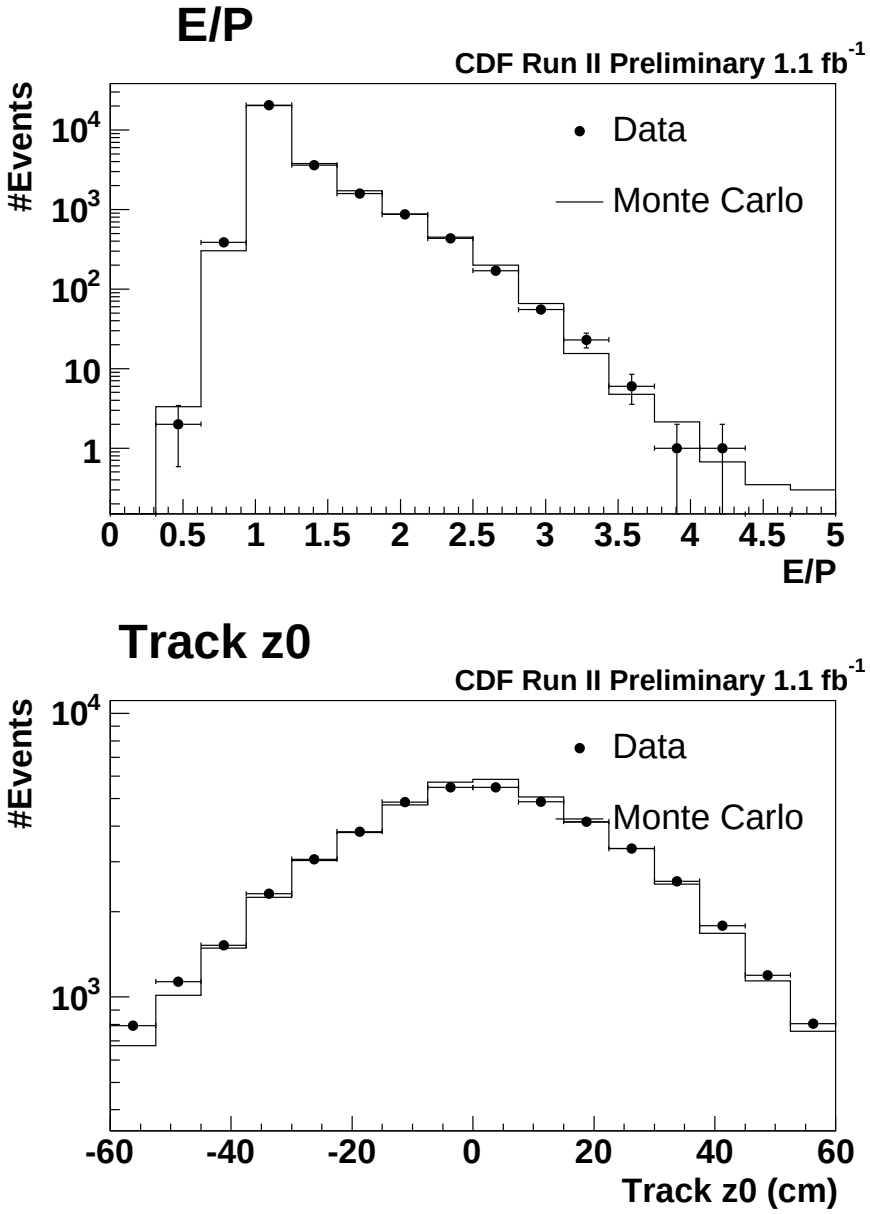

Figure 3.2: The distributions of E/P and track z_0. The data and Monte Carlo simulations are compared.

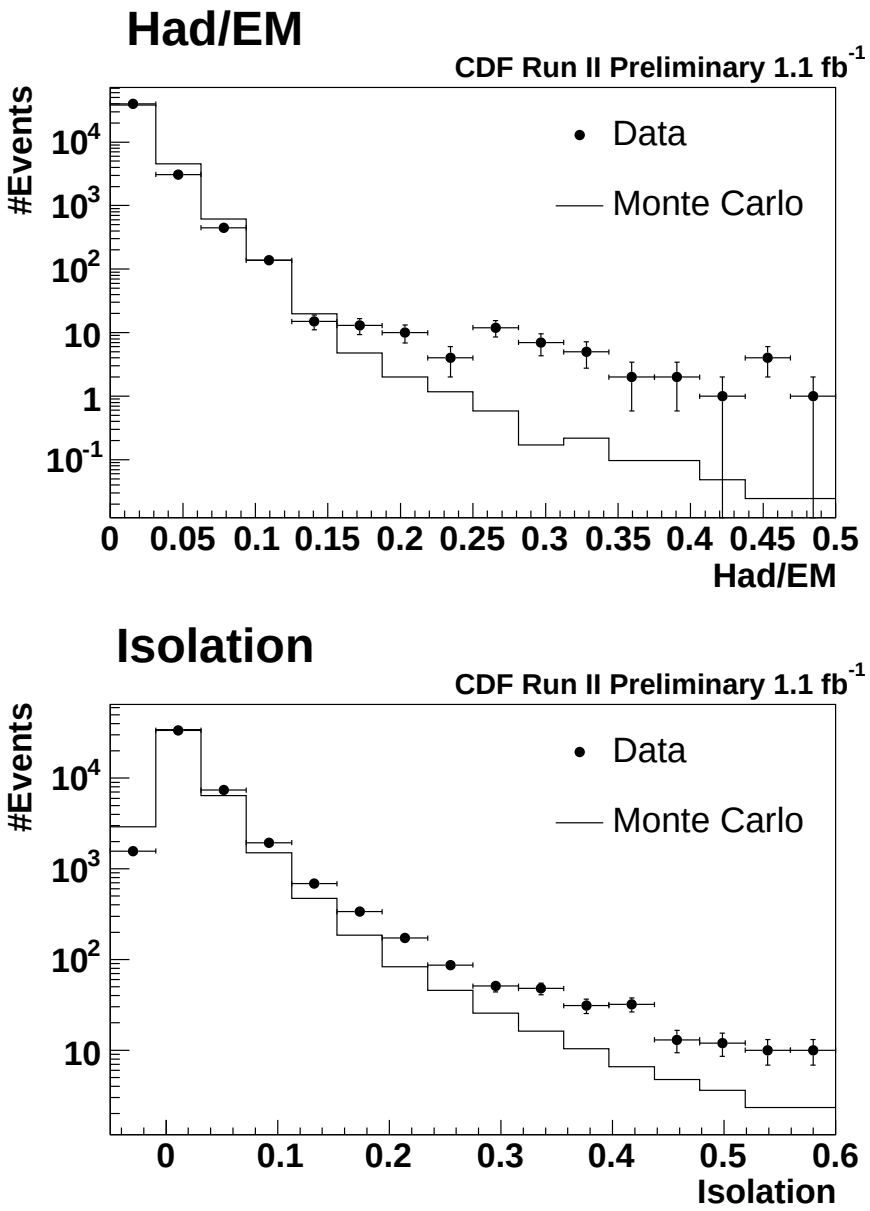

Figure 3.3: The distributions of Had/EM and isolation. The data and Monte Carlo simulations are compared. The excess of the data points at the regions of high Had/EM and isolation shows the background contamination in the data.

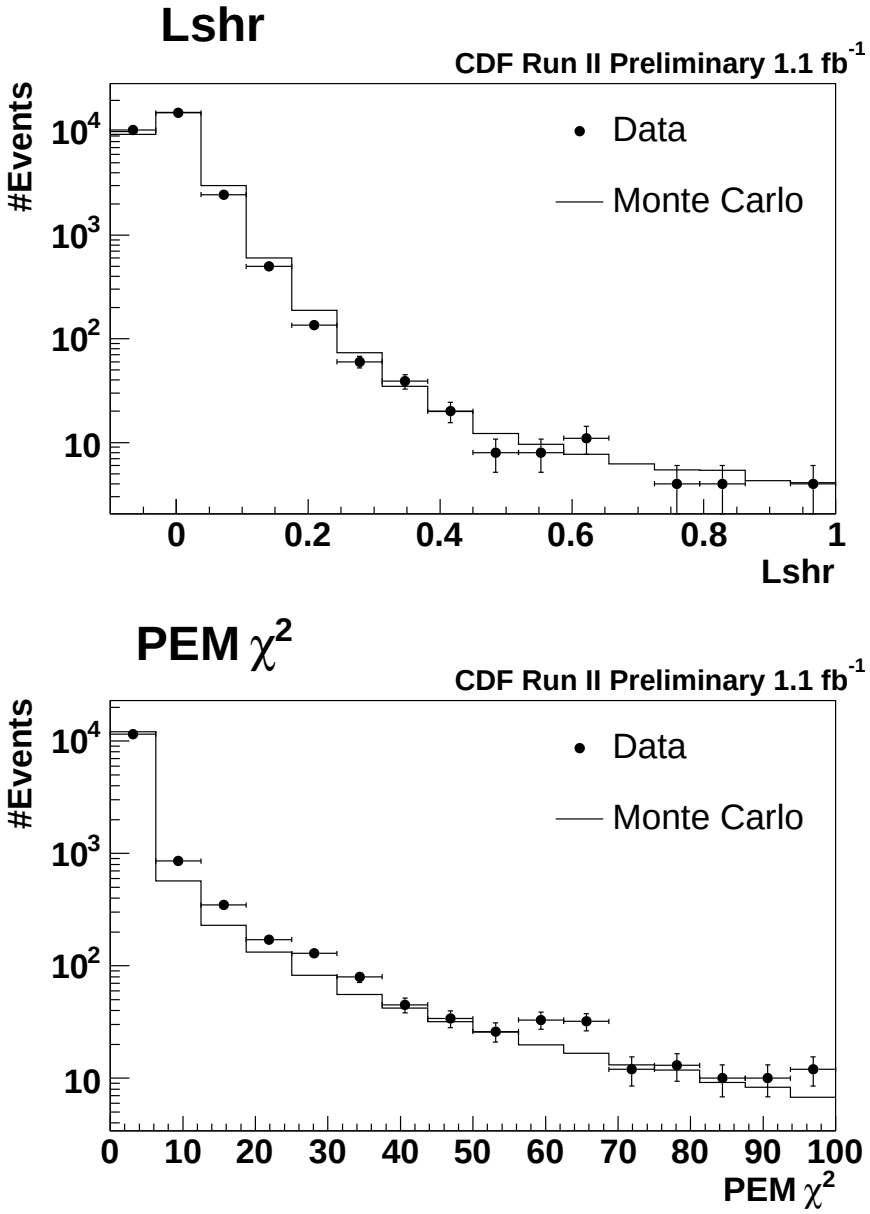

Figure 3.4: The distributions of L_{shr} and PEM $\chi^2_{3\text{ x }3}$. The data and Monte Carlo simulations are compared.

can change according to the instantaneous luminosity and the purpose of physics analyses. Each trigger path serves a specific physics goal, and the di-electron forward-backward asymmetry analysis uses two trigger paths ELECTRON_CENTRAL_18 and ELECTRON70_L2_JET.

The trigger path ELECTRON_CENTRAL_18 consists of three trigger bits, L1_CEM8_PT8, L2_CEM16_PT8 and L3_ELECTRON_CENTRAL_18, which specify the requirements at each level of triggers as following.

- L1_CEM8_PT8 : A central electromagnetic calorimeter tower with $E_T > 8$ GeV and $Had/EM < 0.125$. A matching XFT track with $P_T > 8.34$ GeV/c. Had/EM cut is only required for the towers with $E_T < 14$ GeV.

- L2_CEM16_PT8 : A central electromagnetic calorimeter cluster with $E_T > 16$ GeV and $Had/EM < 0.125$. A matching track with $P_T > 8$ GeV/c.

- L3_ELECTRON_CENTRAL_18 : A central electromagnetic calorimeter cluster with $E_T > 18$ GeV, $Had/EM < 0.125$, $L_{shr} < 0.2$, and $\Delta Z < 8$ cm, with a matching track with $P_T > 9$ GeV/c.

The ELECTRON_CENTRAL_18 path is inefficient at selecting electrons with very high energy, due to the Had/EM requirement. High energetic electron can carry some energy out of electromagnetic calorimeter and deposit the energy in the hadronic calorimeter. The trigger path ELECTRON70_L2_JET is designed to accept such electrons with better efficiency. The trigger path ELECTRON70_L2_JET consists of the following components.

- L1_JET10 : A central or plug calorimeter tower with $E_T > 10$ GeV.

- L2_JET90 : A central or plug calorimeter cluster with $E_T > 90$ GeV.
- L3_ELECTRON70_CENTRAL : A central calorimeter cluster with $E_T > 70$ GeV and $Had/EM < 0.2 + 0.001 \times E$. A matching track with $P_T > 15$ GeV/c is also required.

The Z_NOTRACK trigger path is not used for the event selection, but is used for the background estimation. The path is designed to select $Z \rightarrow e^+e^-$ events based on the calorimeter information without a track requirement.

- L1_EM8 : A central or plug calorimeter tower with $E_T > 8$ GeV and $Had/EM < 0.125$.
- L2_TWO_EM16 : A central or plug calorimeter cluster with $E_T > 16$ GeV and $Had/EM < 0.125$.
- L3_TWO_ELECTRON18 : Two calorimeter clusters with $E_T > 18$ GeV.

3.5 Selection Cuts

From the events passing either ELECTRON_CENTRAL_18 or ELECTRON_CENTRAL_70 trigger paths, at least one central electron is required. The other electron is allowed to be in either the central or the plug region. The cut values for the central and plug electron identification are listed in the Table 3.1.

3.6 Energy Scale

After the selection is made, the global energy scale of the electrons in the central and plug regions is adjusted so that the spectrum of Z mass agrees with the prediction

Variable	Central	Plug
Fiduciality	1 or 2	$1.2 < \|\eta\| < 3.0$
track $\|z_0\|$	$< 60\ cm$	N/A
E_T	$> 25\ GeV$	$> 25\ GeV$
P_T	$> 15\ GeV/c$ ($E_T < 100\ GeV$) $> 25\ GeV/c$ ($E_T > 100\ GeV$)	N/A
E_{Had}/E_{EM}	$< 0.055 + 0.00045 * E$	$< 0.05 + 0.026 * \log(E/100)$
E_T^{iso}	$< 3 + 0.02 * E_T$	$< 1.6 + 0.02 * E_T$
E/P	$< 2.5 + 0.015 * E_T$ ($E_T < 100\ GeV$)	N/A
L_{shr}	< 0.2	N/A
$\|\Delta x\|$	$< 3\ cm$	N/A
$\|\Delta z\|$	$< 5\ cm$	N/A
$PEM\chi^2_{3\ \mathrm{x}\ 3}$	N/A	< 25

Table 3.1: Selection cuts for the central and plug electron candidates.

from LEP I experiments. The correction factor is calculated from the histograms of the invariant mass with the bin size 1 GeV/c^2. The factors are calculated in three regions of the detector; central, plug in the West side, and plug in the East side. The Monte Carlo sample does not show an asymmetry between the East and West events and the same scale factor is used. Each distribution is fitted to a Gaussian function, between the range of invariant mass $86 < M_{ee} < 98$ GeV/c^2. The data and Monte Carlo samples are corrected separately. The global energy scale factors for central and plug electrons are found as follows.

	Data	Monte Carlo
Central	1.000	0.997
Plug	1.029 (West)	1.014
	1.033 (East)	

Additionally, the energy resolution in the Monte Carlo simulation is corrected to match the data. Since the width found from the CC events of the data is smaller

than that of the Monte Carlo simulation, no extra smearing is added to the central electrons in the Monte Carlo sample. Only the energies of the plug electrons are varied randomly.

After correcting the scale and the resolution, the widths of the Gaussian fits are found as follows.

	Before correction		After correction	
	Data (GeV/c^2)	MC (GeV/c^2)	Data (GeV/c^2)	MC (GeV/c^2)
CC	2.988	3.072	2.988	3.030
CP West	3.008	2.934	2.971	2.972
CP East	3.174	2.928	3.072	3.082

The ratio between the di-electron invariant mass distributions of the data and Monte Carlo samples are compared before and after the correction (Fig. 3.5).

The Standard Model expectation for the distributions of invariant mass and $\cos\theta^*$ is shown in Figs. 3.6 and 3.7. The Monte Carlo M_{ee} distribution around 80 GeV/c^2 is sensitive to the modeling of the detector material. The difference between the data and Monte Carlo in that region reflects the uncertainty of the detector material used for the simulation.

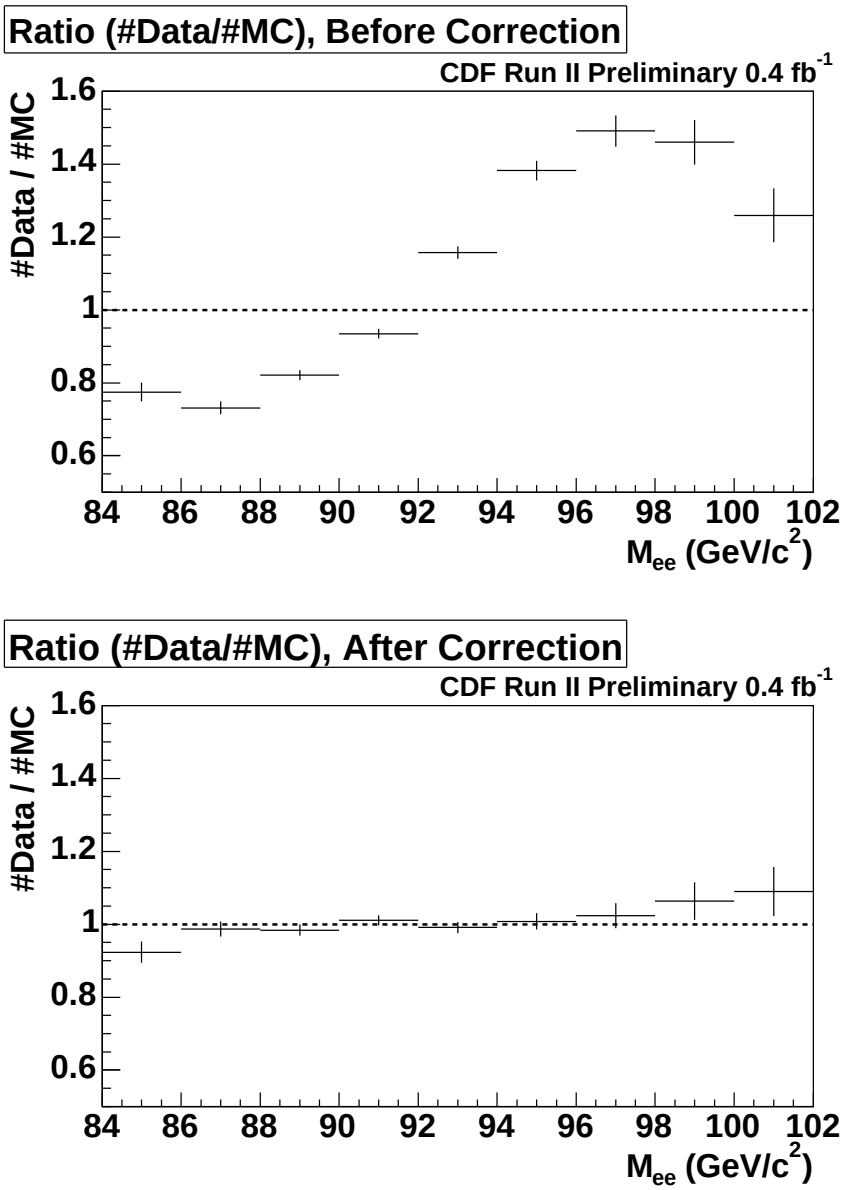

Figure 3.5: Di-electron invariant mass distribution before and after the global energy scale correction.

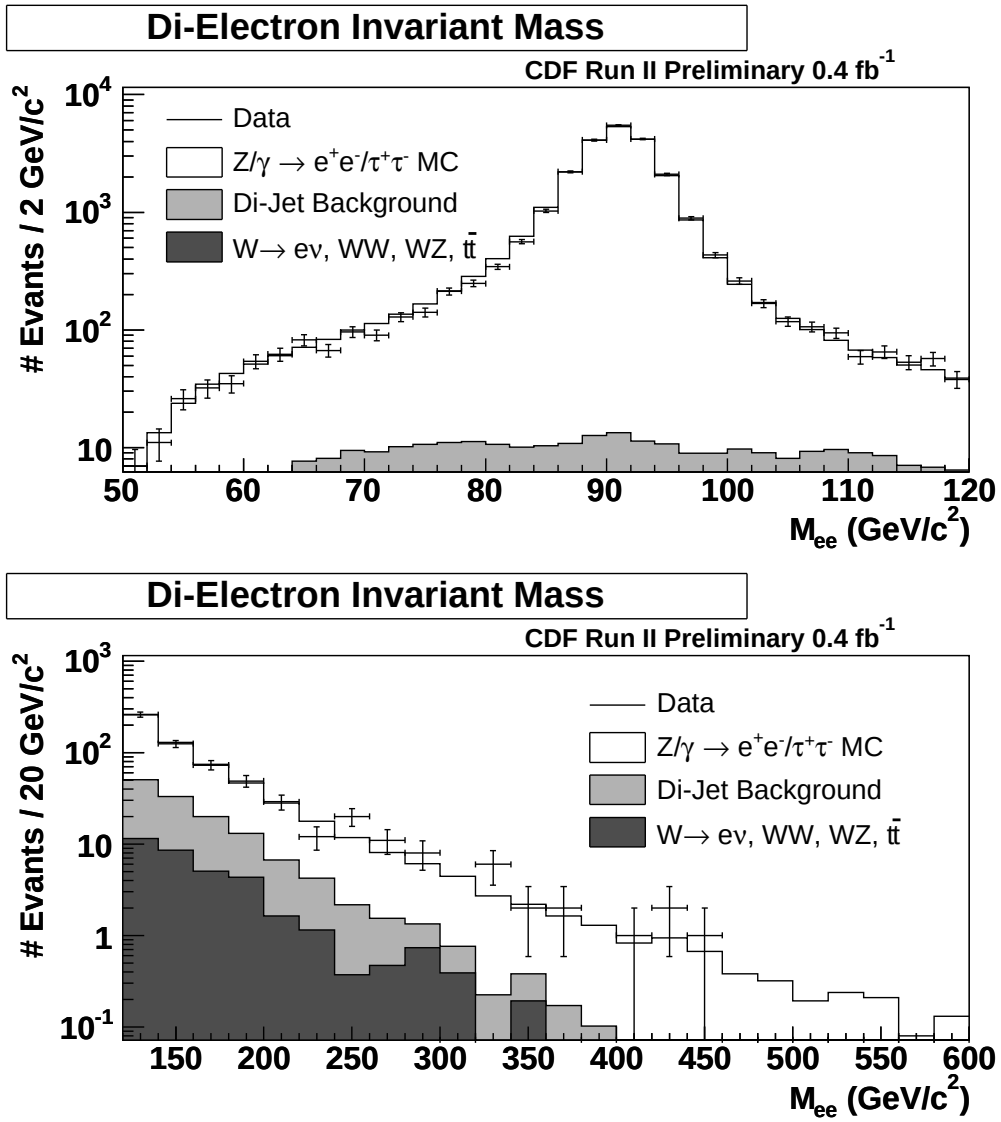

Figure 3.6: Di-electron invariant mass distribution between 50 and 120 GeV/c^2, and between 120 and 600 GeV/c^2. The data is compared to the prediction from Monte Carlo and the background estimation.

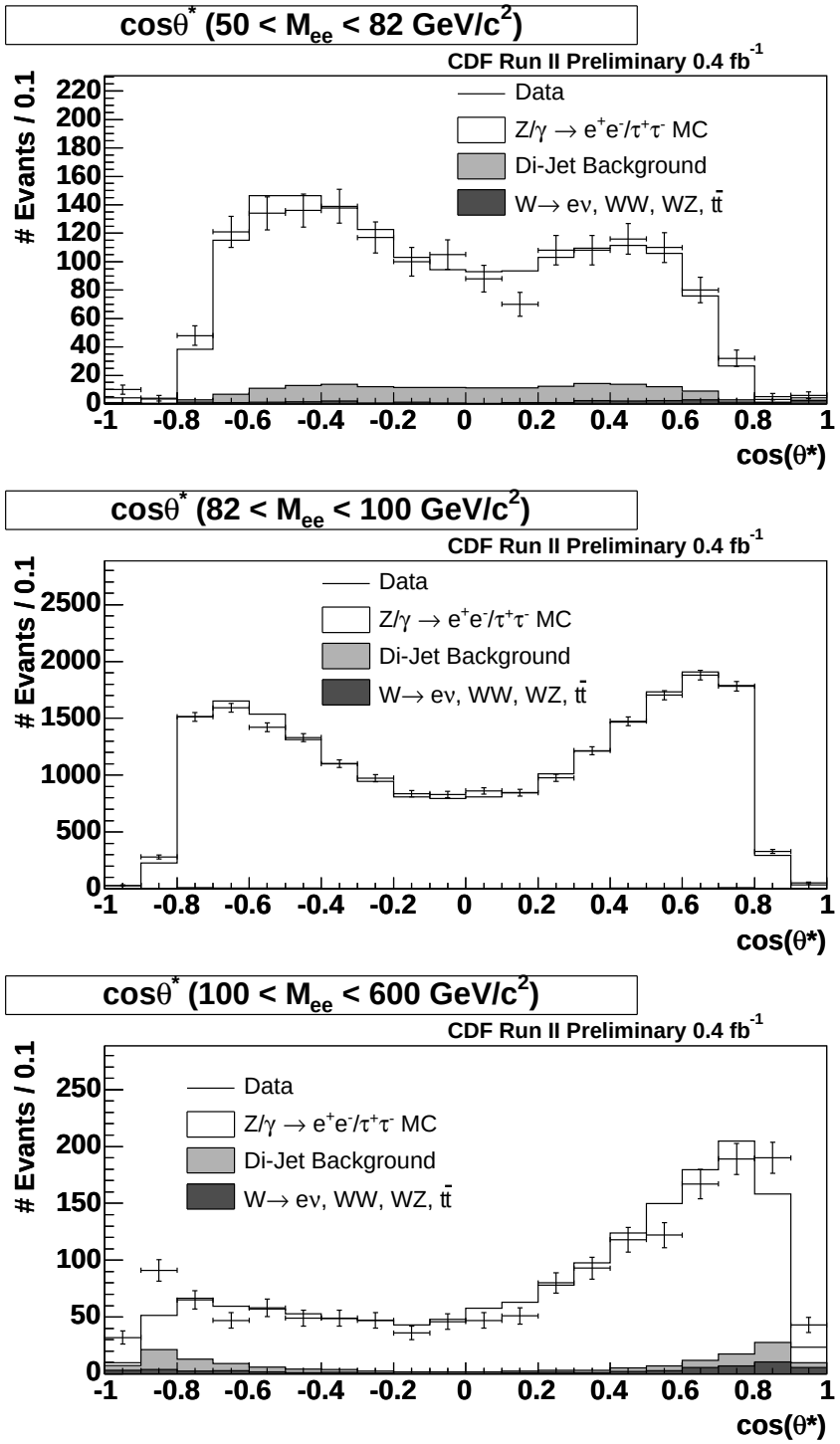

Figure 3.7: $\cos\theta^*$ distribution of the events with the invariant mass between (1) 50 and 82 GeV/c^2, (2) 82 and 100 GeV/c^2 and (3) 100 and 600 GeV/c^2.

Chapter 4

Background

An event that mimics the di-electron signature from the Z decay is a background to the analysis. Such an event may involve jets or photons that are misidentified as electrons, or real electrons from different decays. The probability for a jet to fake an electron is very small, but the jet fake is a significant source of background because the production cross section of di-jet events is large. The amount of di-jet events in the selected candidate events is estimated using the distribution of the isolation variable. Various electroweak processes have smaller cross sections, but they can have real electrons or photons, which can be easily misidentified as electrons. Their contribution to the background is estimated through the Monte Carlo simulation.

4.1 Di-jet Background

Di-jet process is the most significant source of the background to the process $p\bar{p} \rightarrow e^+e^-X$. A jet can fake an electron when hadrons in a jet are misidentified as an electron, or when a jet contains a real electron from a semi-leptonic heavy-flavor decay. The amount of di-jet background in the di-electron sample is estimated from the fact that the electrons from the Z decay tend to be more isolated than the

misidentified jets. The isolation distribution of real electrons is obtained from the pure electron sample which passes very tight cuts. Then the distribution is used as an electron template. The isolation distribution of jets faking electron is obtained from the jet-enriched sample and is used as a jet template. The amount of the di-jet background is estimated by fitting the isolation distribution of the candidate events to the linear combination of an electron template and a jet template. A schematic diagram of the isolation distributions is shown in Fig. 4.1. While the signal region is where the isolation is less than 0.1, the templates include the events with the isolation as large as 0.6 so that the background dominating region is included in the fit.

The sample is divided into three subsamples according to the di-electron invariant mass; below the Z pole, around the Z pole, and above the Z pole. The invariant

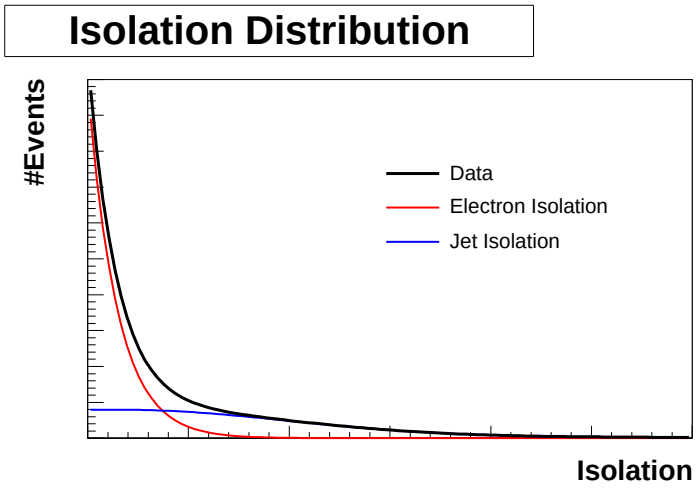

Figure 4.1: A schematic diagram of the isolation distributions of electrons and jets. Electrons tend to be well isolated and the distribution peak at zero. The isolation variable of the jets faking an electron shows a flat distribution. The isolation of the data can be described by the sum of the two distributions.

mass of the di-electron signal events peaks around the Z pole with the invariant mass 91 GeV/c^2, and the number of events drops as the invariant mass goes away from the Z pole. The estimation with the isolation fit is not sensitive to the small rate of the background around the Z pole where the signal dominates. Therefore the fit is performed for the events in the low mass and high mass regions only. The full spectrum of the di-jet background over the entire invariant mass range is obtained by normalizing the di-jet mass distribution with the constraints from the isolation fits.

4.1.1 Isolation Fit

The di-electron selection cuts are listed in the Table 3.1. For the jet background study, the isolation cut for one of the electron legs is released to obtain the isolation distribution in an extended region of the isolation value. The isolation cut in the Table 3.1 is replaced by the following transformation in order to make the cut value a constant.

$$\begin{aligned} \text{Central} &: iso_C = (0.1 * E_T^{iso})/(3.0 + 0.02 * E_T) < 0.1 \\ \text{Plug} &: iso_P = (0.1 * E_T^{iso})/(1.6 + 0.02 * E_T) < 0.1 \end{aligned}$$

These definitions are equivalent to the cuts shown in the Table 3.1, but the signal region is simply defined by a constant cut value after the transformations. This makes it easier to estimate the background because the rate of the background is estimated by integrating the fit result in the signal region between 0 and 0.1.

The electron template is obtained by applying tight cuts (Table 4.1) to the events with invariant mass within 10 GeV/c^2 around the Z mass 91 GeV/c^2. The templates for the central electrons are constructed from the events that pass the trigger paths ELECTRON_CENTRAL_18 or ELECTRON_CENTRAL_70. The templates for the plug electrons are constructed from the trigger path Z_NOTRACK because there is no

Electron Template CC		
Variable	Fitting leg (central)	Control leg (central)
Fiduciality	1 or 2	1 or 2
track$\|z_0\|$	$< 60\ cm$	$< 60\ cm$
E_T	$> 25\ GeV$	$> 25\ GeV$
p_T	$> 15\ GeV/c$ ($E_T < 100\ GeV$) $> 25\ GeV/c$ ($E_T > 100\ GeV$)	$> 15\ GeV$ ($E_T < 100\ GeV$) $> 25\ GeV$ ($E_T > 100\ GeV$)
E_{had}/E_{em}	$< 0.055 + 0.00045 * E$	< 0.05
iso	N/A	$< 0.8 * (3 + 0.02 * E_T)$
E/p	$< 2.5 + 0.015 * E_T$ ($E_T < 100\ GeV$)	$< 2.5 + 0.015 * E_T$ ($E_T < 100\ GeV$)
L_{shr}	< 0.2	< 0.18
χ^2_{strip}	N/A	< 10
$\|\Delta x\|$	$< 3\ cm$	$< 3\ cm$
$\|\Delta z\|$	$< 5\ cm$	$< 3\ cm$
Electron Template CP Central		
Variable	Fitting leg (central)	Control leg (plug)
Fiduciality	1 or 2	$1.2 < \|\eta\| < 3.0$
track$\|z_0\|$	$< 60\ cm$	N/A
E_T	$> 25\ GeV$	$> 25\ GeV$
p_T	$> 15\ GeV/c$ ($E_T < 100\ GeV$) $> 25\ GeV/c$ ($E_T > 100\ GeV$)	N/A
E_{had}/E_{em}	$< 0.055 + 0.00045 * E$	< 0.05
iso	N/A	$< 0.8 * (1.6 + 0.02 * E_T)$
E/p	$< 2.5 + 0.015 * E_T$ ($E_T < 100\ GeV$)	N/A
L_{shr}	< 0.2	N/A
$\|\Delta x\|$	$< 3\ cm$	N/A
$\|\Delta z\|$	$< 5\ cm$	N/A
$PEM\chi^2_{3\ \mathrm{x}\ 3}$	N/A	< 10
5by9U	N/A	< 0.65
5by9V	N/A	< 0.65
Electron Template CP Plug		
Variable	Control leg (central)	Fitting leg (plug)
Fiduciality	1 or 2	$1.2 < \|\eta\| < 3.0$
track$\|z_0\|$	$< 60\ cm$	N/A
E_T	$> 25 GeV$	$> 25\ GeV$
p_T	$> 15 GeV/c$ ($E_T < 100\ GeV$) $> 25 GeV/c$ ($E_T > 100\ GeV$)	N/A
E_{had}/E_{em}	< 0.055	$< 0.05 + 0.026 * \log(E/100)$
iso	$< 0.8 * (3 + 0.02 * E_T)$	N/A
E/p	$< 2.5 + 0.015 * E_T$ ($E_T < 100\ GeV$)	N/A
L_{shr}	< 0.18	N/A
χ^2_{strip}	< 10	N/A
$\|\Delta x\|$	$< 3\ cm$	N/A
$\|\Delta z\|$	$< 3\ cm$	N/A
$PEM\chi^2_{3\ \mathrm{x}\ 3}$	N/A	< 25

Table 4.1: Selection cuts for the electron template. Di-electron invariance mass is required to be within $81 < M_{ee} < 101$ GeV/c^2.

trigger path that selects a single electron in the plug region. QED radiation changes the shape of the template in different mass regions. The effect is estimated by the Monte Carlo program PYTHIA [32] and applied to the template.

The jet template is also obtained from the events triggered by the electron trigger paths in order to avoid the trigger bias. The template for the central jet is constructed from ELECTRON_CENTRAL_18 or ELECTRON_CENTRAL_70, while the plug jet template is constructed from the path Z_NOTRACK. Since these paths are designed to select the electrons, the events that produce the real electrons need to be removed to ensure that the objects that consist the templates are hadronic jets from the process $p\bar{p} \rightarrow g \rightarrow jets$, where g is a gluon that mediates QCD interaction. The decays of W and Z bosons are the most significant source of real electrons. W boson decays to an electron as $W \rightarrow e\nu$. Since the neutrino takes away a large transverse momentum, W events are removed by requiring missing transverse energy (MET) < 15 GeV. The process $Z \rightarrow e^+e^-$ is another source of electrons. Z events are removed by requiring no more than one EM object (section 3.1) with EM $E_T > 10$ GeV. In addition, an energy deposit in the hadronic calorimeter which is back-to-back to the triggered object is required to make sure that the event is with a di-jet final state. Then the electron selection cuts, except for the isolation cut, are applied to the triggered object (Table 4.2).

The isolation distribution of the candidate events is fitted with the electron and jet templates. Likelihood is minimized while taking into account for the limited statistics of the template histograms [10]. Figures 4.2 through 4.4 show the fit results in different invariant mass ranges of central-central (CC) events with two electrons in the central region, and central-plug (CP) events with one electron in the central and the other

Jet Template Central		
Variable	Central EM object	CdfJet
Fiduciality	1 or 2	N/A
track$\|z_0\|$	$< 60\ cm$	N/A
E_T	$> 25\ GeV$	> 25 GeV
p_T	$> 15\ GeV/2$ ($E_T < 100\ GeV$) $> 25\ GeV/2$ ($E_T > 100\ GeV$)	N/A
E_{had}/E_{em}	$< 0.055 + 0.00045 * E$	> 0.125
E_T^{iso}	$< 3.0 + 0.02 * E_T$	N/A
E/p	$< 2.5 + 0.015 * E_T$ ($E_T < 100\ GeV$)	N/A
L_{shr}	< 0.2	N/A
$\|\Delta x\|$	$< 3\ cm$	N/A
$\|\Delta z\|$	$< 5\ cm$	N/A
Jet Template Plug		
Variable	CdfJet	Plug EM object
Fiduciality	N/A	$1.2 < \|\eta\| < 3.0$
E_T	$> 25\ GeV$	$> 25\ GeV$
E_{had}/E_{em}	> 0.125	$< 0.05 + 0.026 * \log(E/100)$
$PEM\chi^2_{3\ \mathrm{x}\ 3}$	N/A	< 25

Table 4.2: Selection cuts for the jet template.

in the plug reigon. The amount of the background is calculated from the integral of the electron template histogram and the jet template histogram in the signal region where the isolation is less than 0.1. With CC events, the isolation distribution of two electron candidates are combined into one histogram. With CP events, central leg and plug leg are fitted separately, and then the results are combined.

The isolation fit is intended to measure the di-jet background, but the result includes the contribution from the $W + jets$ events. This is because the isolation of the radiated jet from the process $W + jets \rightarrow e\ \nu + jets$ follows the distribution of the jet template. The portion of the $W + jets$ events needs to be subtracted from the fit result in order to leave only the contribution from the di-jet background in the measurement. The amount of $W + jets$ to be subtracted is determined from the

Monte Carlo simulation. The subtraction is complicated because $W + jets$ events fake a di-electron event with one real electron and one jet faking electron, while there are two jet faking electrons in the di-jet events. In case of CC events, the isolation value of the two objects are combined into one template. Since $W + jets$ events have only one jet fake, the isolation fit can see only one half of the $W + jets$ events. The number of the $W + jets$ events in the CC candidates is estimated from the Monte Carlo simulation, and one half of the number is subtracted from the estimated number of background events. On the other hand, the di-jet background in the CP events is estimated with two separate fits. While the fit with the isolation of the central leg is sensitive to the total di-jet background, the fit is sensitive to the $W + jets$ background only if the jet fake is in the central region and the real electron is in the plug region. The fit with the plug leg is also sensitive to the total di-jet background, but is sensitive to the $W + jets$ background only if the jet fake is in the plug region and the real electron is in the central region. Because of the track requirement in the central region, the jet fake of the $W + jets$ background is more often found in the plug region than in the central region. The number of the $W + jets$ background in each fits is estimated from the Monte Carlo simulation and is subtracted from the fit result (Table 4.3).

	50-80 GeV			102-600 GeV		
	CC	CP		CC	CP	
		Central Leg	Plug Leg		Central Leg	Plug leg
Fit Result	3.8 ± 3.1	14.4 ± 4.7	20.5 ± 5.4	3.0 ± 0.8	62.9 ± 4.8	50.8 ± 7.0
$W + jets$	0.5 ± 0.4	0.5 ± 0.2	5.7 ± 2.6	0.7 ± 0.5	0.7 ± 0.3	8.0 ± 3.1

Table 4.3: The background measured by the isolation fits and the number of $W + jets$ events subtracted.

4.1.2 Normalizing the Mass Distribution

The fit of the isolation shape estimates the number of the di-jet background in the invariant mass region below the Z pole and above the Z pole. The full spectrum of the di-jet background as a function of the invariant mass is obtained from the di-jet mass distribution, and by normalizing the distribution to the fit results. The di-jet mass distribution is constructed from the events passing the trigger paths ELECTRON_CENTRAL_18 orELECTRON70_L2_JET and the following conditions are required.

- Only 1 EM object with EM $E_T > 10$ GeV.
- At least one jet object with jet $E_T > 10$ GeV with $\Delta\phi$ from the EM object > 0.53.
- MET < 15 GeV.

The conditions are designed to remove the processes that produce real electrons and ensure that the electron-like object is a jet faking electron. The electrons from Z decays are removed by requiring only 1 EM object. The electrons from W decays are rejected by the tight MET cut. The di-jet invariant mass is calculated from the four momenta of one EM object and one CDFJet object. An EM object is reconstructed from the energy deposit in the electromagnetic calorimeter with the clustering algorithm optimized to describe an electron. A CDFJet, on the other hand, is reconstructed from the energy deposits in the electromagnetic and hadronic calorimeter with larger cluster, which is optimized to find a hadronic jet. Since the cluster size of CDFJet is larger than that of EM objects, the energy of the CDFJet needs to be corrected as shown in Fig. 4.5. In order to make the correction, the correction

factor is calculated as a function of the Jet E_T (Fig. 4.6). The factor is calculated from the matching CDFJet object for each EM object. The correction is made by throwing a random number according to the relation between Jet and EM E_T, assuming the Gaussian distribution. The corrected di-jet mass shape is normalized to the constraints found from the isolation fits. The di-jet mass distribution and the background estimation are found to agree with each other (Fig. 4.7). The estimated numbers of background in CC and CP sample are summarized in the Table 4.4. The statistical uncertainty is given from the fit error.

	Total candidates	Total jet background
CC	9455	12.8 ± 3.5
CP	13455	130.0 ± 9.6

Table 4.4: Numbers of di-jet background estimated in CC and CP di-electron candidates. The errors are statistical only.

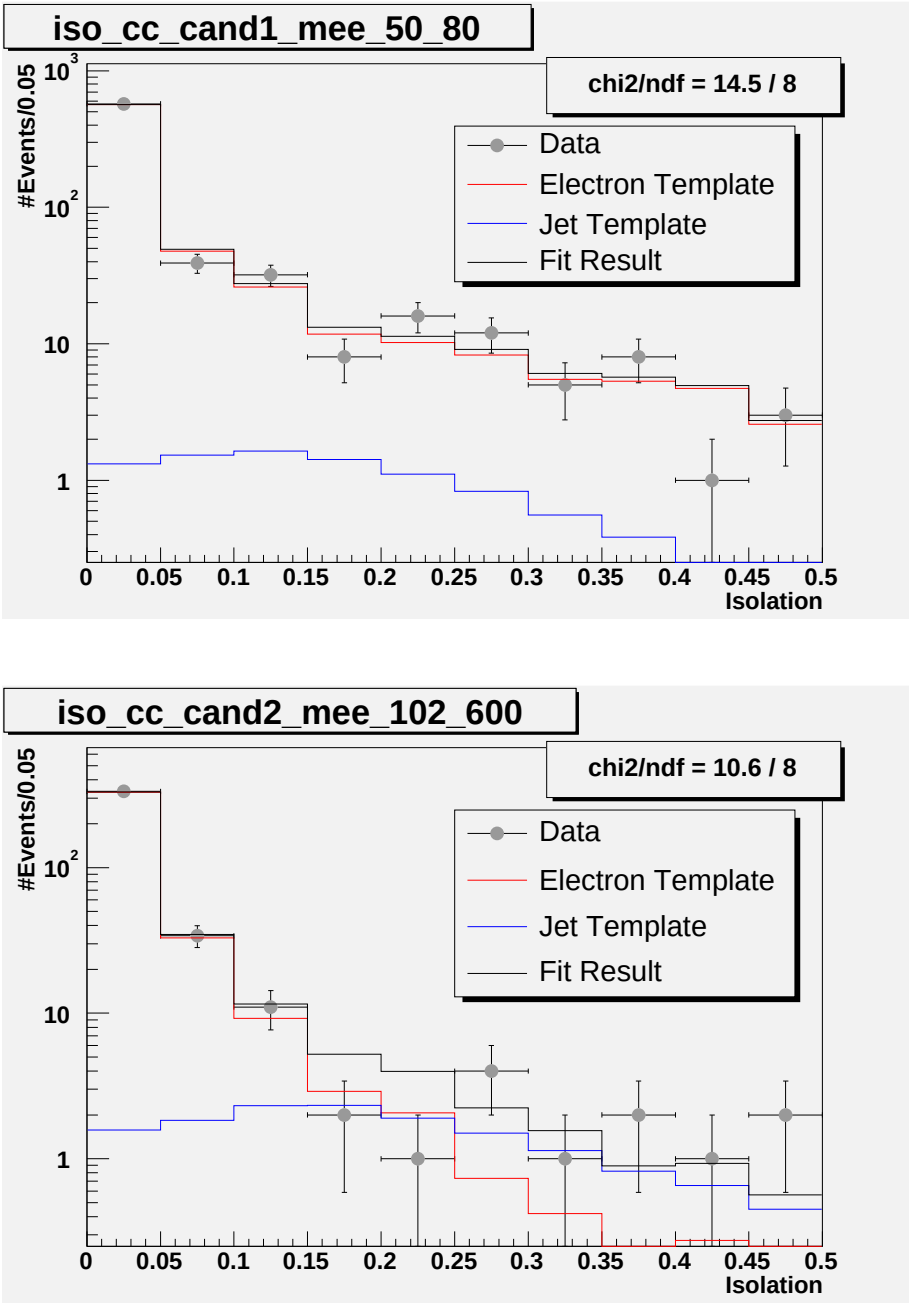

Figure 4.2: Isolation fit result with the CC events. Top plot is for the events in the mass range of 50 and 80 GeV/c^2. Bottom plot is for the events in the mass range of 102 and 600 GeV/c^2.

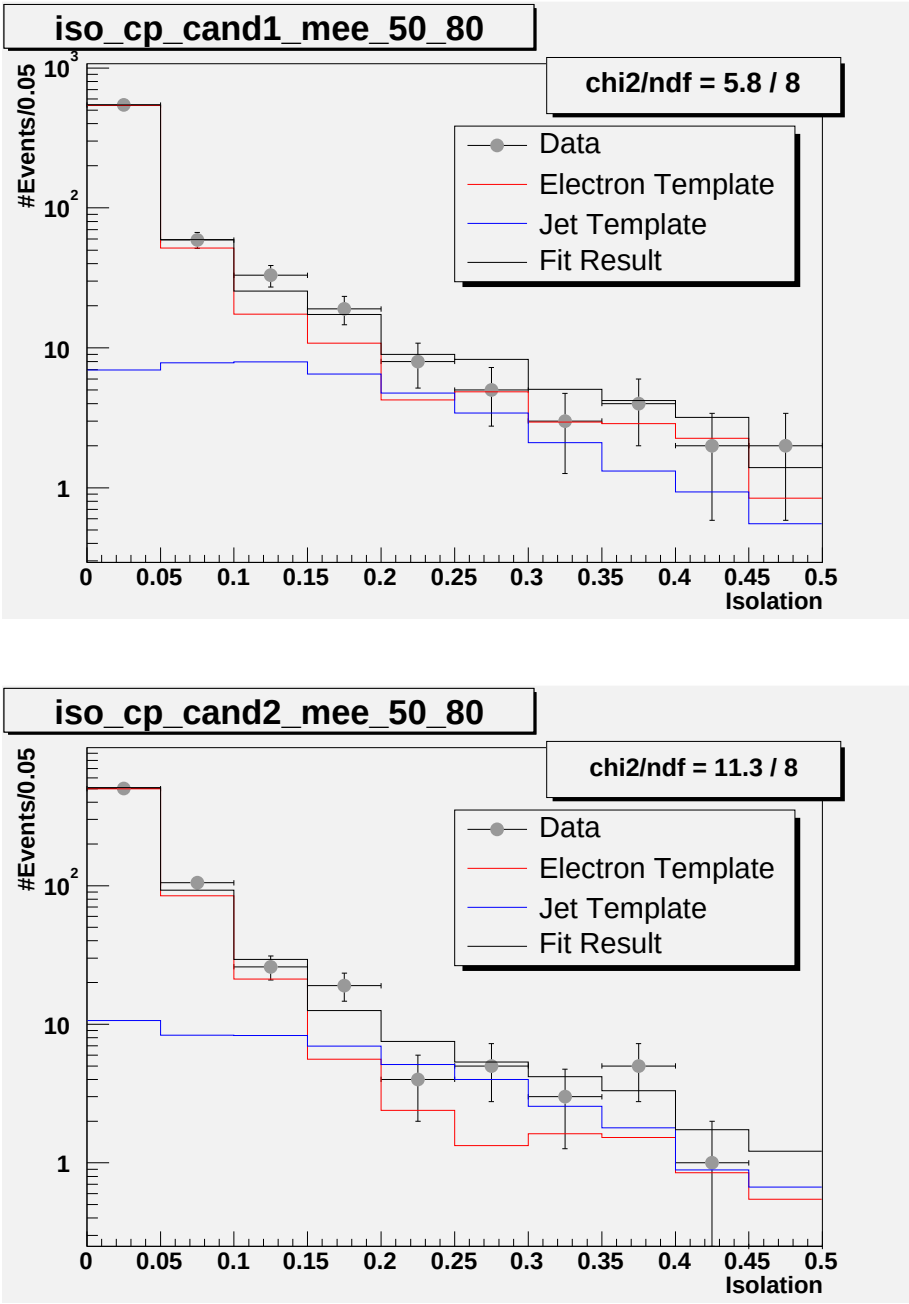

Figure 4.3: Isolation fit result below the Z pole, in the mass range of 50 and 80 GeV/c^2. Top plot is the fit with the central leg of CP events and the bottom plot is the fit with the plug leg.

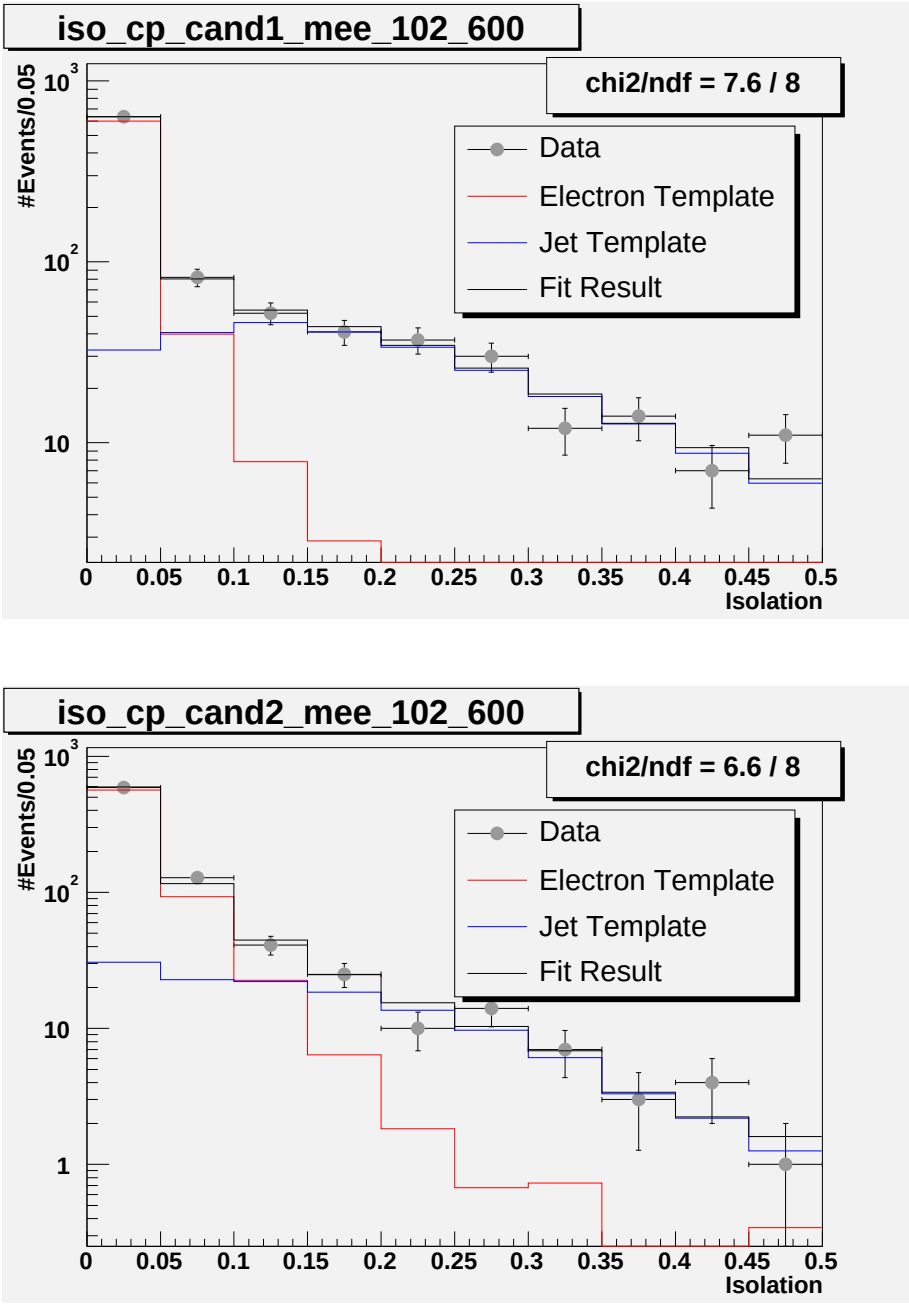

Figure 4.4: Isolation fit result with the CP events above the Z pole, in the mass range of 102 and 600 GeV/c^2. Top plot is the fit with the central leg of CP events and the bottom plot is the fit with the plug leg.

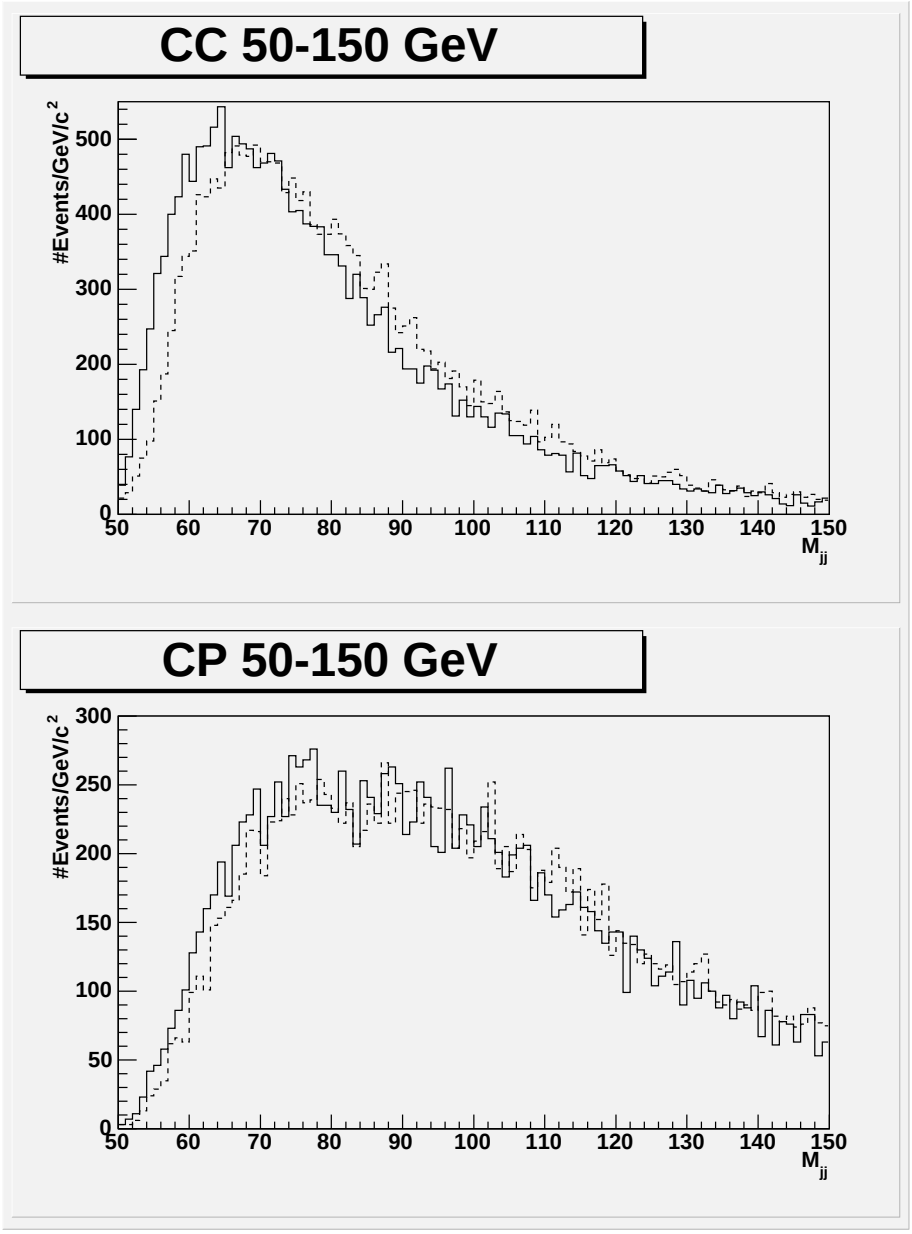

Figure 4.5: The di-jet mass distribution is constructed from one EM object and a CDFJet for each event. The difference in the clustering between CDFJet and EM object is corrected. Dashed line is before the correction and the solid line is after the correction.

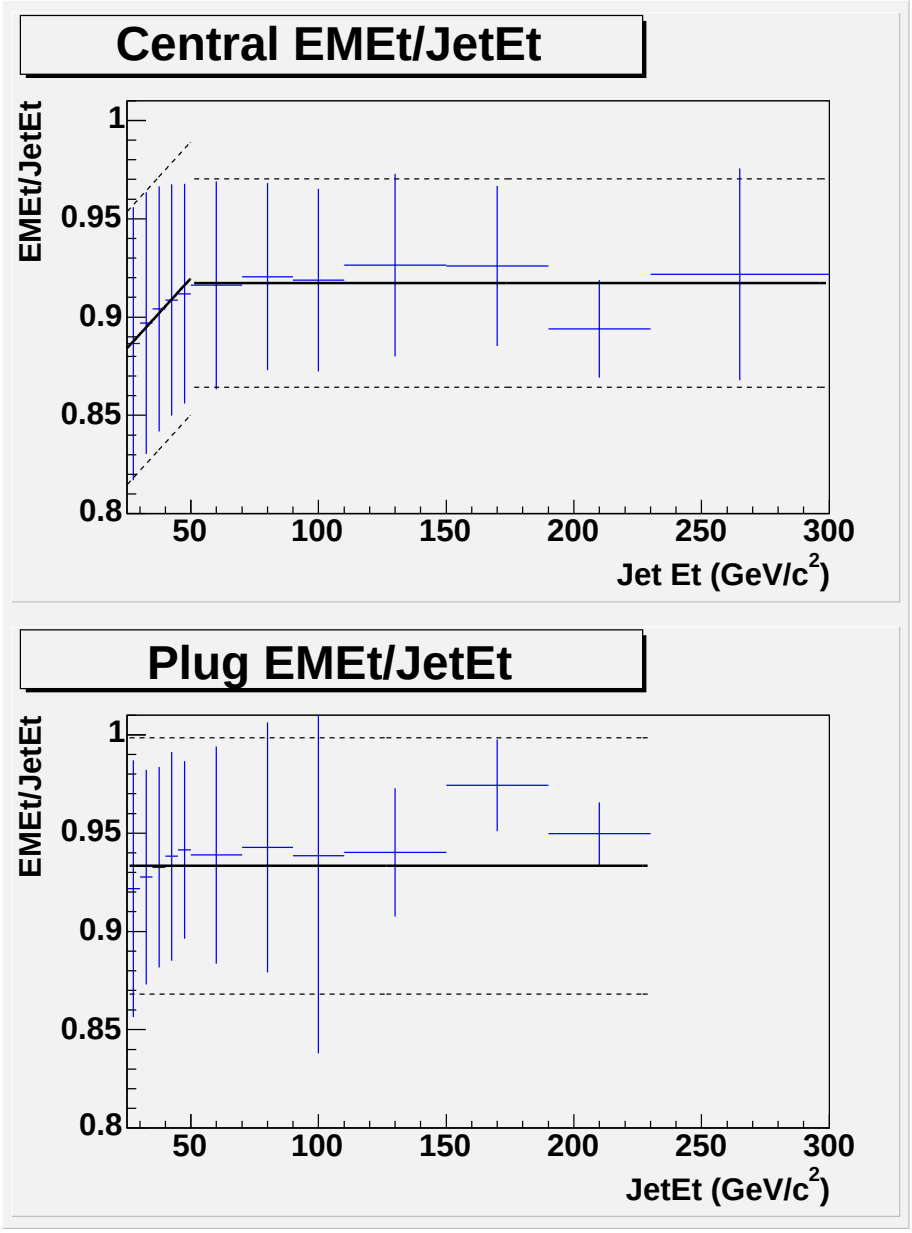

Figure 4.6: For each CDFJet, corresponding EM E_T is found. The mean and the spread of the ratio of the two E_T's is used to correct for the different clustering algorithms.

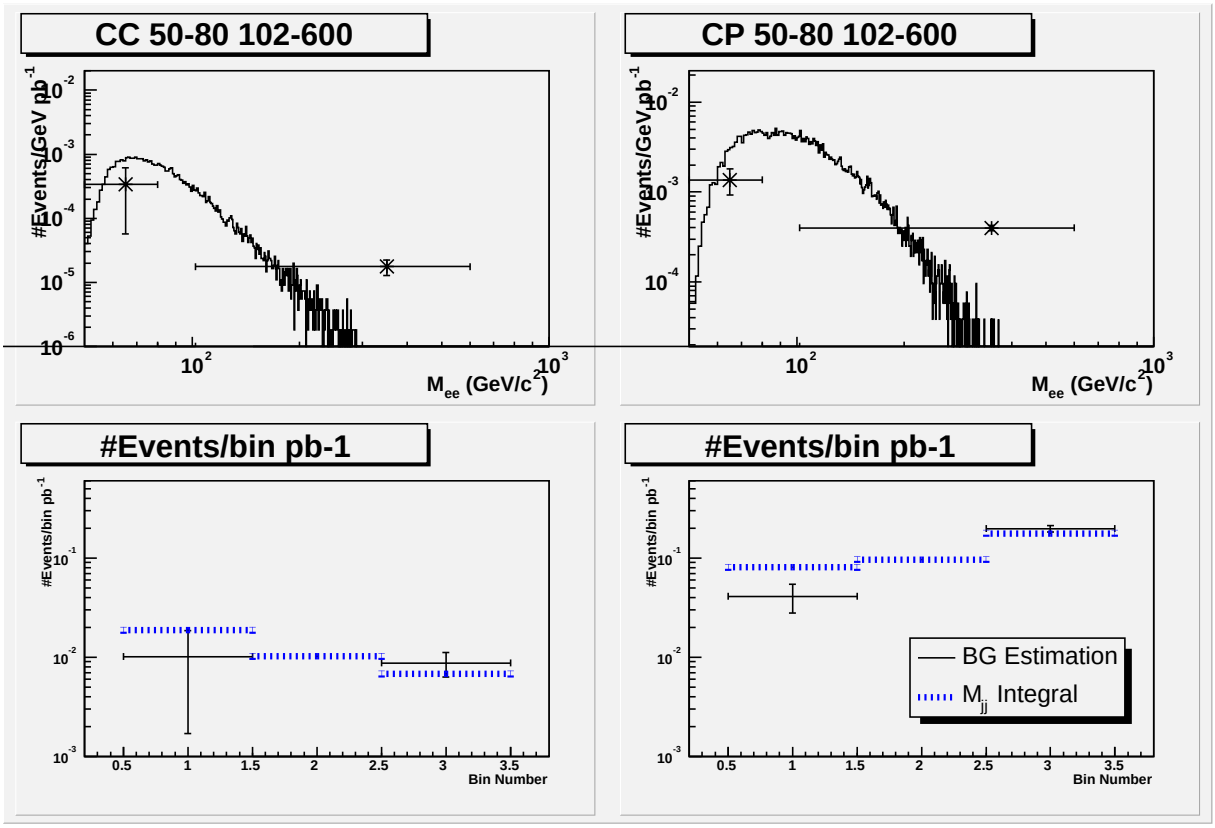

Figure 4.7: The histograms in the top plots are the CC and CP di-jet mass distributions. The points with error bars are the background estimated from the isolation fits. In order to compare them with each other, the histogram is integrated and shown as the thick dotted lines on the bottom plots. The bottom plots show that the isolation fit describes the di-jet mass shape within statistical uncertainty.

4.1.3 Systematic Uncertainties

While the statistical uncertainty of the di-jet background is given by the fit error, systematic uncertainty is estimated by changing various parameters involved in the background estimation. Fig. 4.8 shows how the electron template is changed to estimate the systematic uncertainty. The gray area shows the Poisson error band of the input template. The distribution is distorted by shifting the value by one sigma upward in the signal region where isolation is less than 0.1, and downward by one sigma elsewhere. Then the background is estimated with the distorted template and the difference of the results is recorded (Table 4.5). The template is changed in the opposite direction and the effect is calculated as well. The systematic uncertainty due to the jet template is estimated in the same way. The systematic uncertainty due to the $W + jets$ subtraction is estimated by changing the amount of the subtraction by the uncertainty of the $W + jets$ background. The effect of applying tighter cuts to the electron template is also considered as a systematic uncertainty. The tighter the cuts are, the purer the sample gets. However if there are correlations between the cuts, tight cuts can distort the isolation distribution. Therefore the change in the background estimation resulted by applying tighter cuts is considered a source of systematic uncertainty. Lastly, the amount of the detector material in the Monte Carlo simulation is changed to see its effect on the background measurement. The Monte Carlo simulation plays a role in the correction of the electron template for the radiation effect. The uncertainty in the detector material in the central region is 0.01 X_0. Two million events with the extra material is simulated for the systematic study. Another two million events were simulated with 1/6 of X_0 extra material in the plug region. The estimated uncertainties are summarized in the Table 4.5.

	CC		CP	
# Background	12.8		130.0	
Electron Template	+1.7	-1.4	+1.0	-1.1
Jet Template	+0.4	-0.4	+4.5	-4.4
$W + jets$ Subtraction	+1.9	-2.8	+1.4	-2.7
Tight Cuts	+0.4	-0.4	+3.0	-3.0
Central Material	+0.4	-0.4	+1.0	-1.0
Plug Material	+0.8	-0.8	+1.0	-1.0
Total Systematic Uncertainty	+2.8	-3.3	+5.8	-6.3
Statistical Uncertainty	± 3.5		± 9.6	
Total Uncertainty	+4.5	-4.8	+11.2	-11.5

Table 4.5: Systematic and statistical uncertainties to the background estimation. CC (central-central) events and CP (central-plug) events are shown separately.

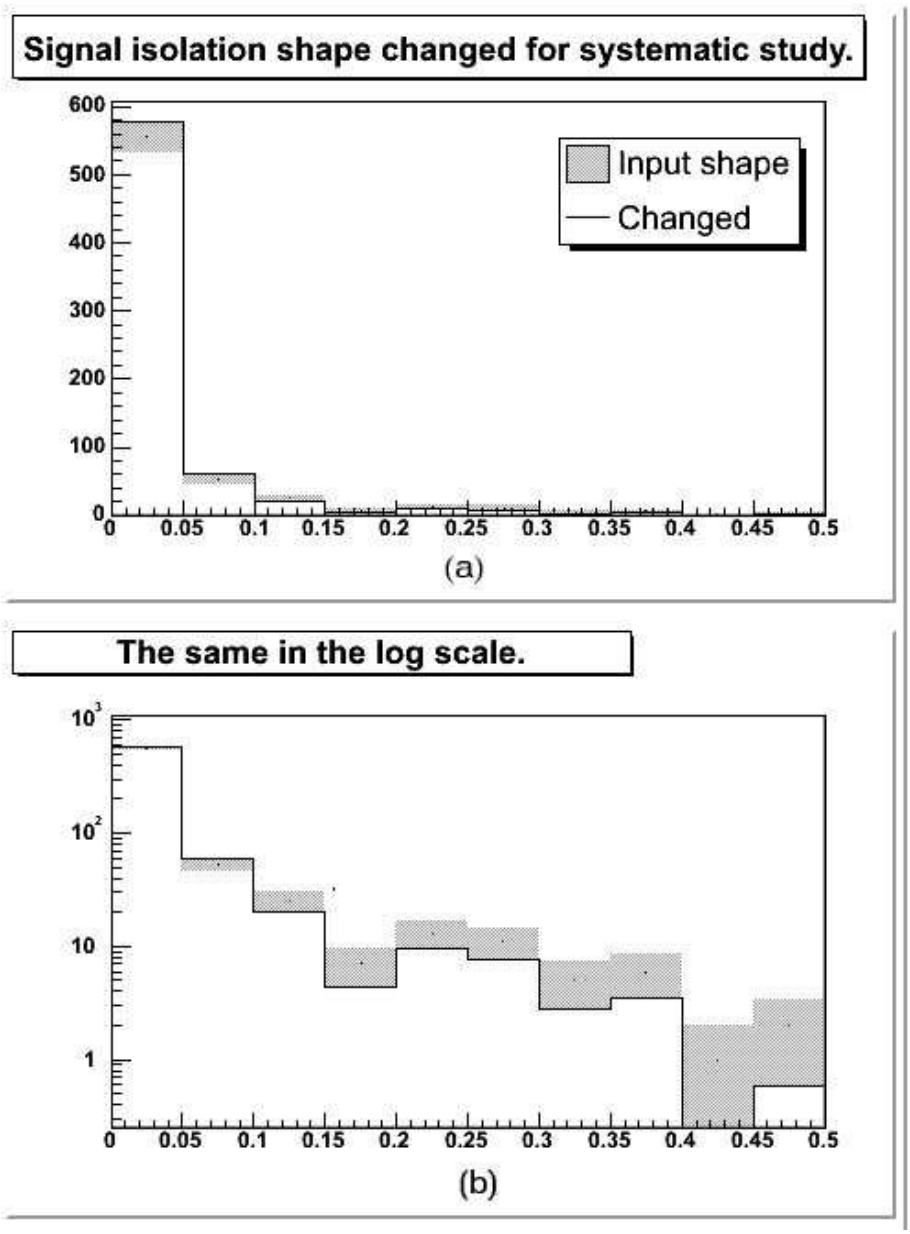

Figure 4.8: Distorted electron template used to measure the systematic uncertainty. The distribution is shifted upward by one sigma as shown in (a). In the other bins, the distribution is shifted downward, as shown in (b) in log scale.

4.2 Electroweak Background

Various electroweak processes contribute to the observed di-electron signal. While the cross sections of the processes are much lower than the di-jet production, their contribution becomes significant if the final state includes one or more electron or photon. One of such processes is $W \rightarrow e\nu$ with a radiated photon or jet. A photon can be misidentified as an electron because its behavior in the calorimeter is very similar to that of an electron. The rate of misidentification in the central region is low because the electrically neutral photon does not leave a trajectory in the tracking chamber. However the rate is higher in the plug region of the detector, where a track is not required. A jet is misidentified as an electron with much lower probability, but its contribution is significant because a jet is more often radiated than a photon. A production of di-boson can also lead to a di-electron final state. A production of two W bosons can result in a di-electron final state when the W bosons decay into electron-neutrino pairs. A production of W and Z bosons also contribute to a di-electron final state when the Z boson decays into an electron pair. Finally, a production of a top quark pair makes a final state with two electrons with a small probability. A top quark almost always decays into W boson and a b quark. The W boson then can decay into an electron and a neutrino. A di-electron final state is obtained when both top quarks decay in such a way. The expected numbers of di-electron background events for the four processes are estimated by Monte Carlo simulations and summarized in the Table 4.6. The estimated number of background is subtracted from the observed number of events before the measurement of the forward-backward asymmetry. The electron scattering angle of the electroweak background is asymmetric as shown in the Fig. 4.9. The asymmetry is taken into account when the background is subtracted.

Process	$\sigma \cdot$ Br (pb)	CC	CP	Total
$W \rightarrow e\nu + jet/\gamma$	709.6	3.7	70.5	74.3 ± 6.1
$WW \rightarrow ll\nu\nu$	1.39	5.9	6.5	12.4 ± 0.3
WZ $(Z \rightarrow e^+e^-)$	0.41	5.6	6.4	12.0 ± 0.3
$t\bar{t}$ inclusive	5.50	3.2	1.9	5.1 ± 0.2

Table 4.6: Electroweak background estimated from Monte Carlo simulation. CC (central-central) events and CP (central-plug) events are calculated separately.

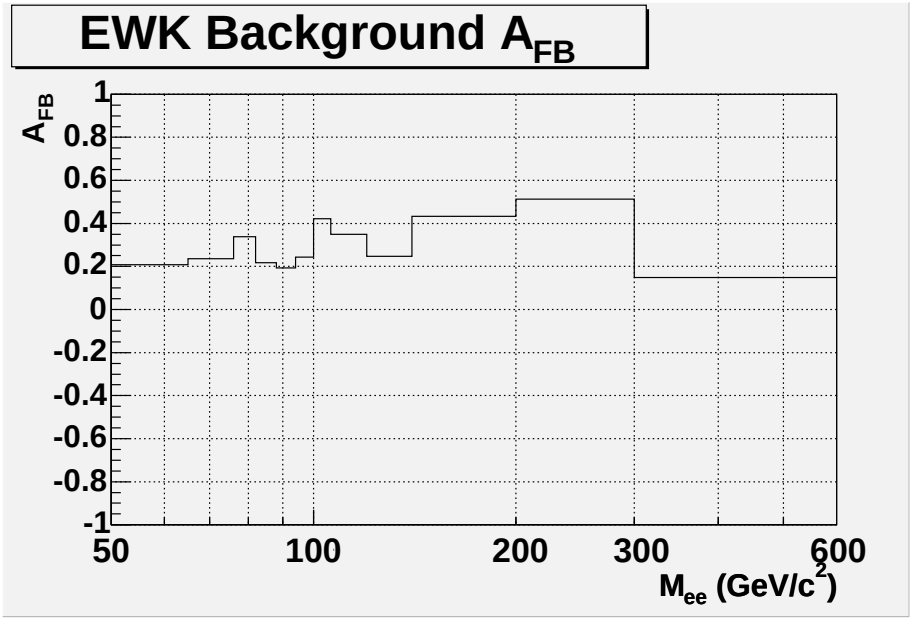

Figure 4.9: Forward-backward asymmetry A_{FB} of the electroweak background processes.

Chapter 5

Forward-Backward Asymmetry

The forward-backward asymmetry, A_{FB}, as defined by the Eq. (1.28) is measured in twelve di-electron invariant mass ranges. The raw A_{FB} is calculated simply from the observed number of events in each invariant mass range as

$$A_{FB}^{raw,i} = \frac{N_F^i - N_B^i}{N_F^i + N_B^i}, \tag{5.1}$$

where N_F and N_B are the numbers of forward and backward events in the ith invariant mass range. An event is denoted forward if $\cos\theta^*$ is positive, where θ^* is the electron scattering angle measured from the proton beam direction, given by

$$\cos\theta^* = \frac{2}{Q\sqrt{Q^2 + Q_T^2}}(P_1^+ P_2^- - P_1^- P_2^+), \tag{5.2}$$

where Q (Q_T) is the four momentum (transverse momentum) of the electron-positron pair. $P_i^{\pm}$ is defined to be $\frac{1}{\sqrt{2}}(P_i^0 \pm P_i^3)$, where P^0 and P^3 represent energy and the longitudinal components of the momentum, and $i = 1,\ 2$ represent electron and positron, respectively. A backward event has a negative $\cos\theta^*$. The di-electron invariant mass bins are labeled by $i = 1,\ 2,\ 3,\ \cdots, 12$, from 50 to 600 GeV/c^2. However, the raw A_{FB} differs from the true A_{FB} because the invariant mass distribution is distorted by the detector resolution and the QED final state radiation.

The systematic uncertainty on the measurement is estimated by repeating the measurement with varied parameters for each source of the systematics. The most significant sources of the systematics are the energy scale, energy resolution and the material in the Monte Carlo simulation. The systematic uncertainties due to the background estimation, limited statistics of the Monte Carlo sample, and the parton distribution function uncertainties are also measured.

5.1 Unfolding

The measurement of A_{FB} is complicated by the detector resolution and QED radiation which distort the distribution of the di-electron invariant mass M_{ee}. A correction to the M_{ee} distribution needs to be made in order to recover the true M_{ee} distribution and therefore the true A_{FB} as defined in Eq. (1.28). The procedure of such a correction is called unfolding.

The method of matrix inversion is chosen for this analysis because of its simplicity and lack of bias. Suppose that the true numbers of events in the invariant mass bin j is μ_j. We will refer to the vector $\boldsymbol{\mu} = (\mu_1, ..., \mu_N)$ as a true histogram. Note that these are expectation values, rather than the actual numbers of events in the invariant mass bins. The vector $\boldsymbol{\mu}$ is what we want to measure by unfolding. The observed numbers of events are $\mathbf{n} = (n_1, ..., n_N)$. It is possible to regard the variables n_i as independent Poisson variables with expectation values $\nu_i = E[n_i]$. In other words, the probability to observe n_i events in bin i is given by

$$P(n_i; \nu_i) = \frac{\nu_i^{n_i} e^{-\nu_i}}{n_i!}. \tag{5.3}$$

The expected number of events to be observed in bin i can be written as

$$\nu_i = \sum_{j=1}^{N} R_{ij}\, \mu_j, \tag{5.4}$$

where

$$\begin{aligned} R_{ij} &= \frac{P(\text{observed in bin } i \text{ and true value in bin } j)}{P(\text{true value in bin } j)} \\ &= P(\text{observed in bin } i \mid \text{true value in bin } j). \end{aligned} \tag{5.5}$$

The response matrix element R_{ij} is thus the conditional probability that an event will be found in bin i given that the true value was in bin j. The effect of off-diagonal elements in R is to smear out any fine structure. The smearing between the bins needs to be kept small in order to keep the statistical uncertainties in the final result low.

Summing over the first index gives

$$\sum_{i=1}^{N} R_{ij} \equiv \varepsilon_j, \tag{5.6}$$

i.e., one obtains the average value of the efficiency over bin j. If the expectation value for the background process in bin i is known, the vectors $\boldsymbol{\mu}$, $\boldsymbol{\nu}$, $\boldsymbol{\beta}$ and the matrix R are related as $\boldsymbol{\nu} = R\boldsymbol{\mu} + \boldsymbol{\beta}$. The matrix relation can be inverted to give $\boldsymbol{\mu} = R^{-1}(\boldsymbol{\nu} - \boldsymbol{\beta})$. The estimators of $\boldsymbol{\nu}$ is given by the corresponding data value, $\hat{\boldsymbol{\nu}} = \mathbf{n}$. The estimators for the $\boldsymbol{\mu}$ are then

$$\hat{\boldsymbol{\mu}} = R^{-1}(\mathbf{n} - \boldsymbol{\beta}). \tag{5.7}$$

In order to unfold the distribution of A_{FB}, the distributions of the forward events $\boldsymbol{\mu}^F$ and the backward events $\boldsymbol{\mu}^B$ are separately unfolded with two response matrices R^F and R^B, obtained from the forward and backward events from the Monte Carlo

simulation. The smearing between forward and backward is correctly taken into account for the construction of R^F and R^B. For example, if a forward event is reconstructed as a backward event, the efficiency of the R^F decreases and that of R^B increases. The unfolded A_{FB} of invariant mass bin i is written in terms of the unfolded numbers of events as following.

$$A_{FB}^i = \frac{\mu_i^F - \mu_i^B}{\mu_i^F + \mu_i^B}, \tag{5.8}$$

where $\mu_i^{F,B} = R_{ij}^{(F,B)-1}\nu_j^{F,B}$. The statistical uncertainty for the unfolded number arises from the data ($\boldsymbol{\nu}$) and from the response matrix (R_{ij}^{-1}):

$$(\sigma_{\mu_i})^2 = \sum_{j=1}^{N}(\frac{\partial\mu_i}{\partial\nu_j}\sigma_{\nu_j})^2 + \sum_{j=1}^{N}(\frac{\partial\mu_i}{\partial R_{ij}^{-1}}\sigma_{R_{ij}^{-1}})^2 = \sum_{j=1}^{N}(R_{ij}^{-1}\sigma_{\nu_j})^2 + \sum_{j=1}^{N}(\nu_j\sigma_{R_{ij}^{-1}})^2, \tag{5.9}$$

where the uncertainties of the response matrix $\sigma_{R_{ij}^{-1}}$ can be written as [26],

$$(\sigma_{R_{ij}^{-1}})^2 = \sum_{\alpha=1}^{N}\sum_{\beta=1}^{N}[R_{i\alpha}^{-1}]^2[\sigma_{R_{\alpha\beta}}]^2[R_{\beta j}^{-1}]^2. \tag{5.10}$$

5.2 Pseudo Experiment Test

The validity of the matrix inversion method is tested with the pseudo experiments generated by the Monte Carlo simulation. Two million Monte Carlo events are used to throw 11 mutually exclusive pseudo experiments. Each pseudo experiment is unfolded with the inverted response matrix (Fig. 5.1). The averaged result shows that the input asymmetry agrees with the measurement made through the matrix inversion unfolding method (Table 5.1 and Fig. 5.2).

Mass (GeV/c^2)	$\hat{A}_{FB}$	A_{FB}^{LO}	$\hat{A}_{FB} - A_{FB}^{LO}$	$\sigma_{\hat{A}_{FB}}$	pull of A_{FB}
50-65	-0.380	-0.340	-0.040	0.017	-2.29
65-76	-0.430	-0.457	0.028	0.022	1.25
76-82	-0.244	-0.335	0.091	0.025	3.70
82-88	-0.134	-0.120	-0.013	0.014	-0.98
88-94	0.062	0.063	-0.001	0.004	-0.24
94-100	0.192	0.209	-0.017	0.013	-1.26
100-106	0.320	0.355	-0.036	0.028	-1.28
106-120	0.484	0.474	0.010	0.030	0.34
120-140	0.590	0.571	0.020	0.042	0.46
140-200	0.602	0.613	-0.010	0.046	-0.22
200-300	0.583	0.620	-0.037	0.087	-0.43
300-600	0.682	0.617	0.066	0.173	0.38

Table 5.1: Eleven pseudo experiments. $\hat{A}_{FB}$ is the mean of eleven measurements. Measurements are compared with the leading order calculations. $\sigma_{\hat{A}_{FB}}$ is the expected spread of the measurements assuming 364 pb^{-1}. Pull of A_{FB} is $(\hat{A}_{FB} - A_{FB}^{LO})/\sigma_{\hat{A}_{FB}}$ and its RMS is 1.46.

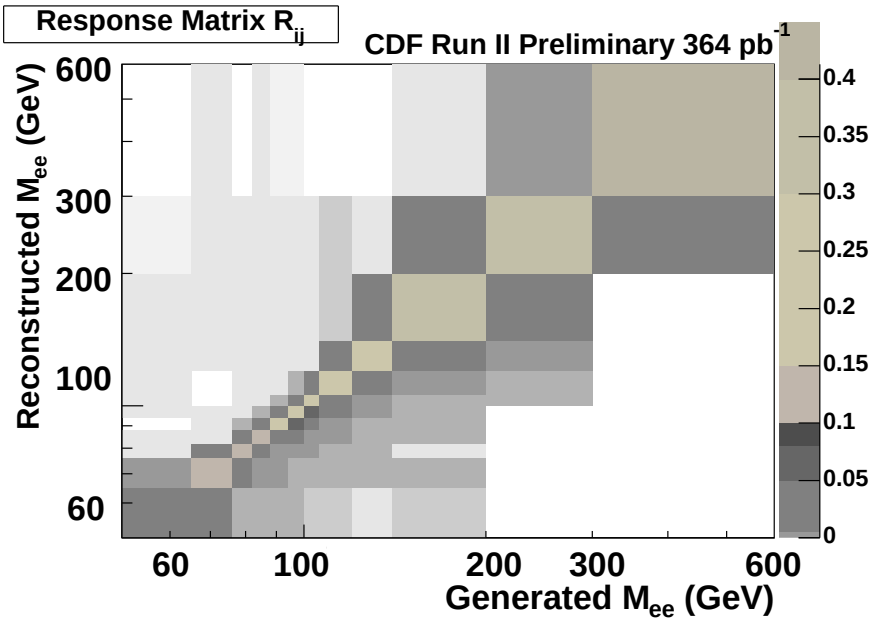

Figure 5.1: The response matrix. Each column is normalized to the detection efficiency of the events generated in the mass bin.

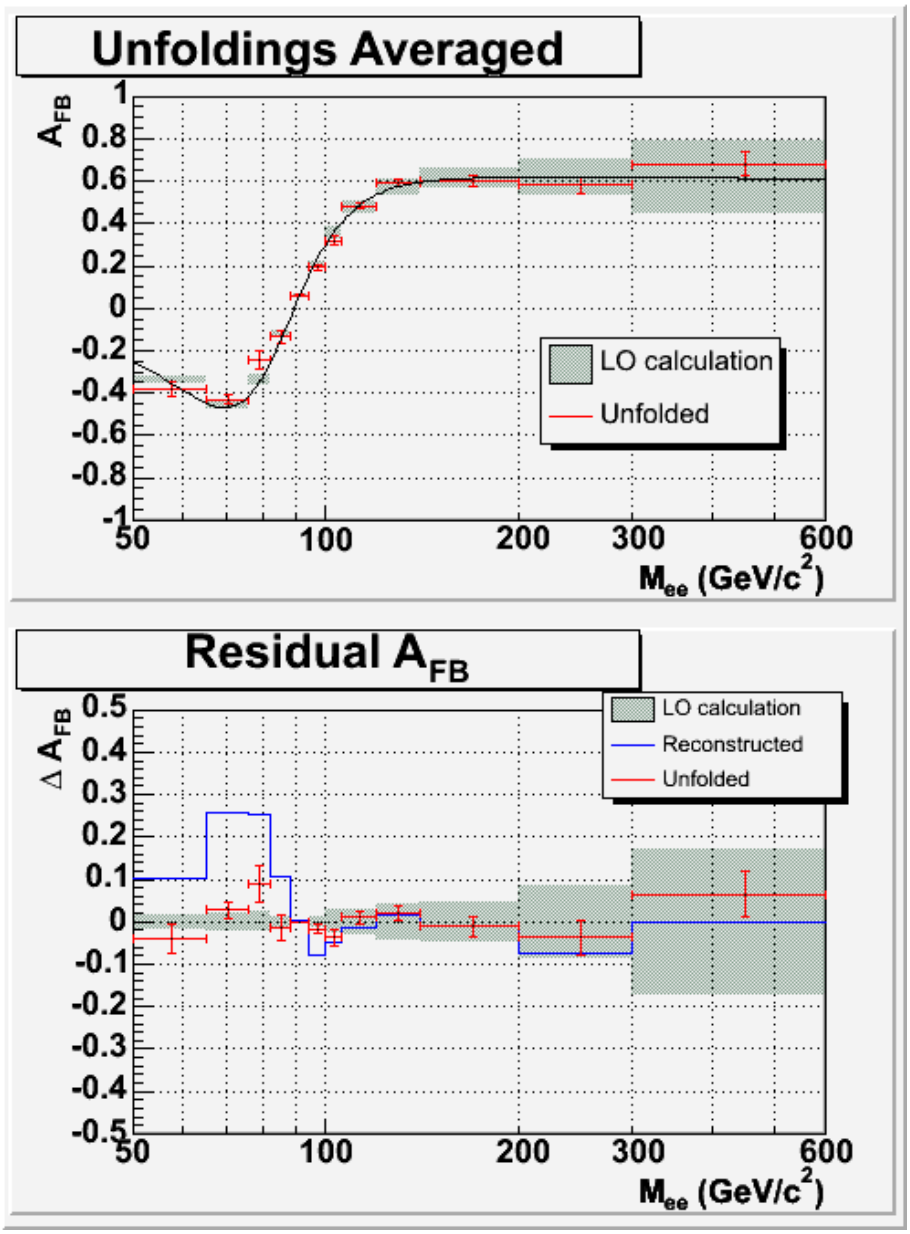

Figure 5.2: The 11 pseudo experiments. Shaded area is the LO prediction with the expected spread of the measurement at 364 pb^{-1}. Blue histogram is the A_{FB} before the unfolding. The unfolded A_{FB} is shown in red with the error = RMS/$\sqrt{11-1}$.

5.3 Systematic Uncertainty

The systematic uncertainty on the measurement of A_{FB} is estimated for the following sources.

- Energy scale and resolution.
- Detector material in the Monte Carlo simulation.
- Background estimation.
- Response matrix.
- Parton distribution function used for the Monte Carlo simulation.

The uncertainty of the energy scale is estimated from the di-electron invariant mass distribution of the data as a function of the $|\eta_{det}|$ of the electron (Fig. 5.3). η is divided into 13 regions between $\eta = -2.8$ and $\eta = 2.8$. The distribution of the di-electron invariant mass of the events that belong to the η bin is fitted to a Gaussian function. The mean of the Gaussian in each η bin is shown in the plot. The values of 13 η bins fluctuate around the Z mass 91 GeV/c^2. The uncertainty of the energy scale is shown as the dashed line that covers the fluctuating invariant masses. Based upon the observation, the uncertainty on the energy scale is chosen as 0.2 % when$|\eta| <$ 2.35 and 0.8 % when $|\eta| > 2.35$. In order to estimate the systematic uncertainty on the A_{FB} originating from the uncertainty of the energy scale, the energies of the electrons in the pseudo experiments are varied by 0.2 % and 0.8 % according to the η coordinates of the electrons. The shifts in the measured A_{FB} due to the variation are taken as the systematic uncertainty on A_{FB} in each invariant mass bin.

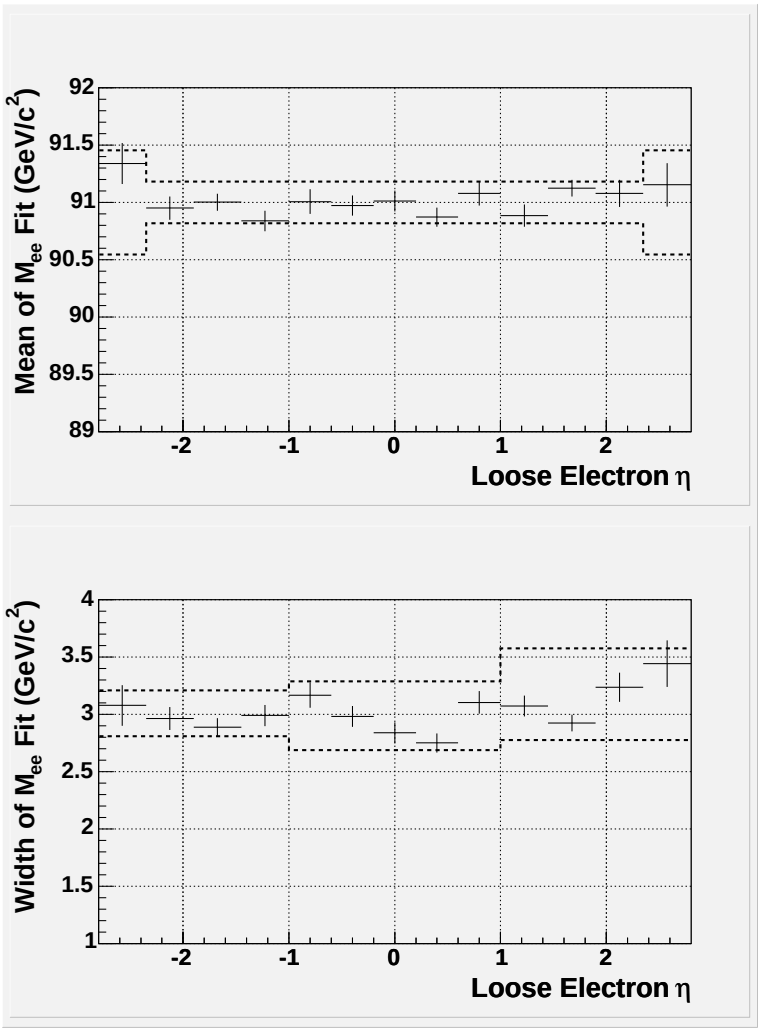

Figure 5.3: The uncertainties in the energy scale and the resolution are found from the Gaussian peaks of mass distributions.

Similarly, the uncertainty of the energy resolution is estimated from the fluctuations of the width of the di-electron invariant mass distribution in each η bin (Fig. 5.3). The uncertainty of the energy resolution is found to be 0.3 GeV in the central region ($|\eta| < 1.0$), 0.2 GeV in the West plug region ($\eta < -1.0$), and 0.4 GeV in the East plug region ($\eta > 1.0$). The systematic uncertainty on the A_{FB} measurement is found by adding extra smearing to the electron energies in the pseudo experiment events. For each electron, the energy is changed to the random number generated following the Gaussian distribution centered at the original electron energy with the width equal to the uncertainty found from the Fig. 5.3. The shifts in the measured A_{FB} due to the variation are taken as the systematic uncertainty of the A_{FB} due to the uncertainty of the energy resolution.

The response matrix is made with the Monte Carlo simulation events which is affected by the amount of the detector material used for the detector simulation. For the material systematic study, two million $p\bar{p} \rightarrow Z/\gamma \rightarrow e^+e^-$ events are generated by the event generating program Pythia. The standard sample is made from the two million $Z \rightarrow e^+e^-$ events by running the detector simulation with the best estimation of the detector material. Another sample is made from the same two million events, but by running the detector simulation with 1 % of X_0 more material in the central tracking region of the detector. Lastly, the same two million events were simulated with 1/6 of X_0 extra material in the plug region. Fig. 5.4 shows how the material uncertainty in the central region is determined. The three response matrices with different input materials were used to measure A_{FB} of the 11 pseudo experiments. The variations in the measured A_{FB} are taken as the systematic uncertainty on A_{FB}.

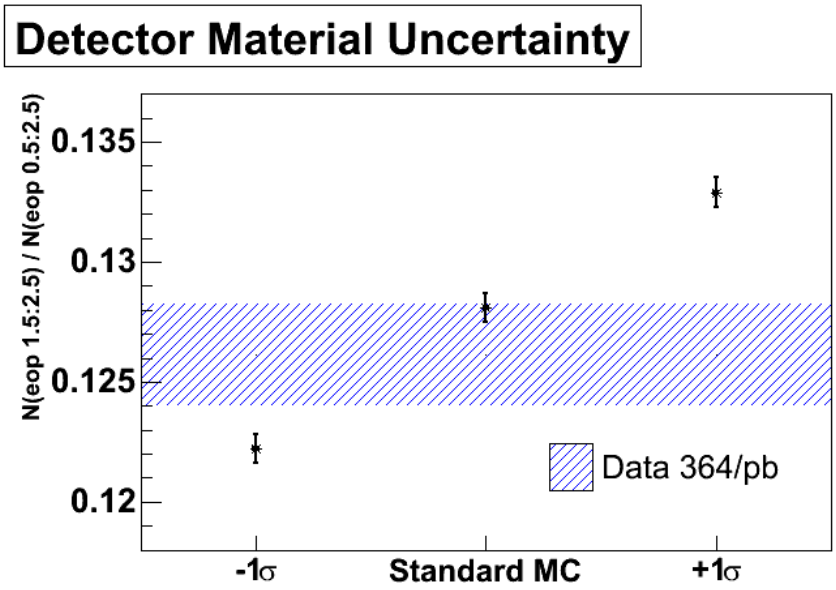

Figure 5.4: Determination of the central material uncertainty with the E/P distribution. The y-axis is the ratio of the numbers of events with $1.5 < E/P < 2.5$ and $0.5 < E/P < 2.5$. The events with $1.5 < E/P < 2.5$ are most sensitive to the material effect, therefore the ratio directly reflects the amount of the material. Three Monte Carlo samples were generated changing the material by $\pm$ 1 % X_0. The ratio and its uncertainty calculated form the data is shown by the blue box. 1 % is conservatively selected as the uncertainty of the central material in the simulation.

The amount of the estimated background is subtracted from the forward and backward di-electron invariant mass distributions before applying the matrix inversion unfolding. The uncertainty in the background estimation is therefore a source of the systematic uncertainty on the A_{FB} measurement. The statistical and systematic uncertainties in the background measurement are found from the procedure described in section 4. In order to see the effect of the background subtraction to the measurement of the A_{FB}, the subtraction is made by the amount of the estimated background plus the uncertainty in the background estimation. The change in the measured A_{FB}

due to the overestimated background is the systematic uncertainty on A_{FB}.

The Monte Carlo program that creates the response matrix uses the parton distribution function (PDF) CTEQ5L. The function describes the probability for each flavor of partons to participate in the hard scattering interaction. A PDF function is constructed from the fits to various experimental data. The uncertainty of each fit contributes to the uncertainty of the PDF function. The CTEQ PDF is made from 20 fits to the data. To help the error analysis, CTEQ provides 40 PDF functions with each eigenvector changed by plus and minus 1 sigma of the fit error [28]. In order to estimate the systematic uncertainty on the A_{FB} measurement due to the uncertainty in the PDF function, 40 response matrices are made by weighting the standard Monte Carlo events. The weighting factor is calculated for each event based upon the fractional momentum of the generated partons. The 40 response matrices are then applied to the 11 standard pseudo experiments to determine the systematic uncertainty on the A_{FB} measurement (Fig. 5.5).

The response matrix for the unfolding is made from the 10 million $Z \rightarrow e^+e^-$ events. Each element of the inverted matrix R^{-1} has an uncertainty due to the limited statistics of the Monte Carlo sample (Eq. 5.10). The elements of the inverted matrix are shifted by the amount of the uncertainties and the systematic uncertainty of the A_{FB} measurement is estimated.

The systematic uncertainties for each source is summarized in the Table 5.2. The total systematic uncertainty is calculated as the square sum of the individual uncertainties.

Mass GeV/c^2	LO A_{FB}	Energy Scale	Energy Resol.	PDF	Material	Back-ground	Reponse Matrix	Total Syst.
50-65	-0.340	±0.009	±0.020	±0.003	±0.015	±0.018	±0.018	±0.037
65-76	-0.457	±0.010	±0.006	±0.002	±0.060	±0.016	±0.027	±0.069
76-82	-0.335	±0.017	±0.047	±0.001	±0.041	±0.008	±0.067	±0.093
82-88	-0.120	±0.030	±0.063	±0.003	±0.062	±0.002	±0.023	±0.096
88-94	0.063	±0.022	±0.005	±0.001	±0.008	±0.000	±0.002	±0.010
94-100	0.209	±0.028	±0.033	±0.002	±0.037	±0.001	±0.030	±0.064
100-106	0.355	±0.018	±0.014	±0.001	±0.033	±0.005	±0.029	±0.050
106-120	0.474	±0.011	±0.007	±0.000	±0.026	±0.012	±0.017	±0.036
120-140	0.571	±0.005	±0.015	±0.000	±0.018	±0.018	±0.015	±0.034
140-200	0.613	±0.004	±0.009	±0.000	±0.041	±0.030	±0.017	±0.054
200-300	0.620	±0.006	±0.016	±0.001	±0.022	±0.030	±0.030	±0.051
300-600	0.617	±0.000	±0.034	±0.001	±0.049	±0.012	±0.042	±0.074

Table 5.2: Summary of the systematic uncertainty from various sources. The leading order calculation of A_{FB} is shown. The material uncertainty is measured separately with the extra material in the central and plug, and then combined.

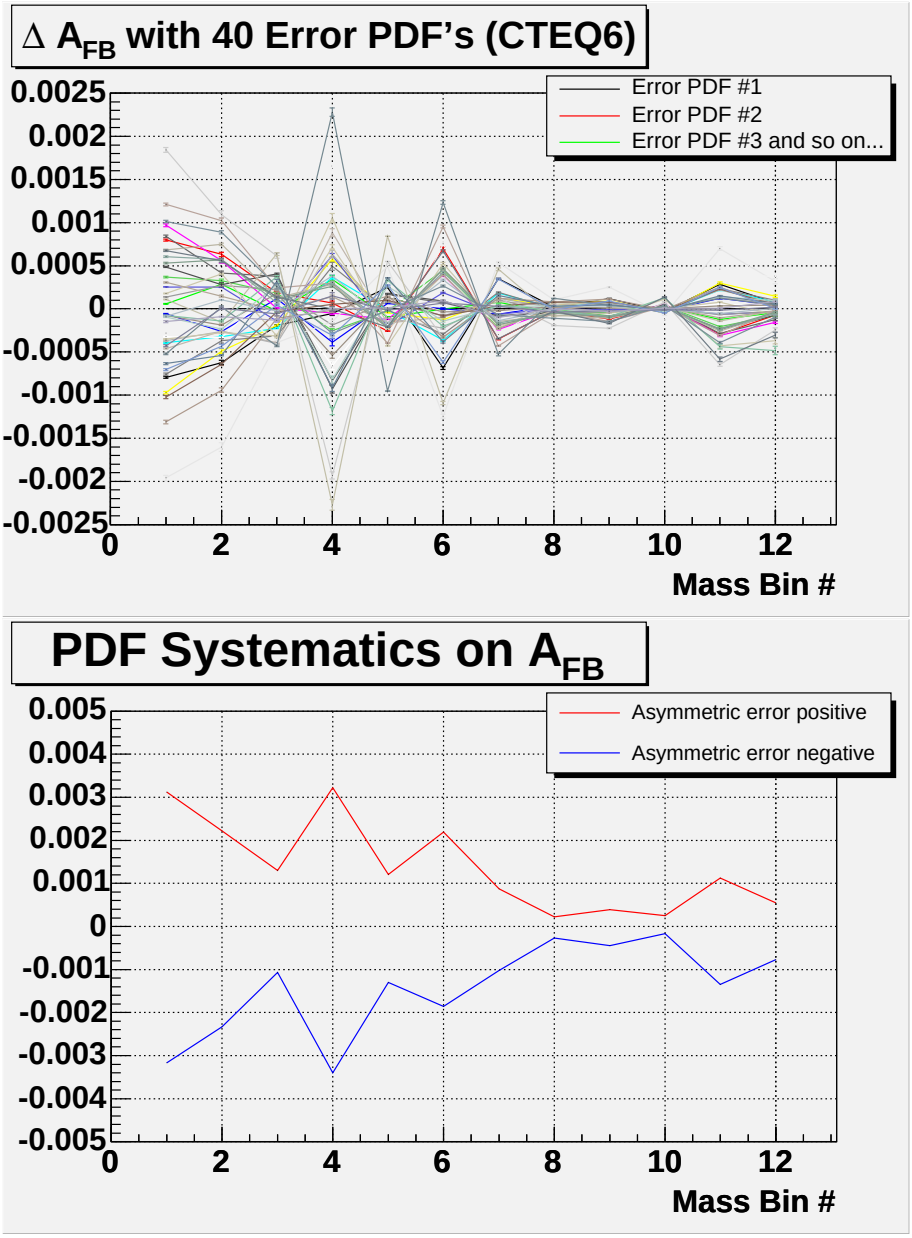

Figure 5.5: Forty error PDF's are used for the PDF systematic measurement. The upper plot shows the effect of each individual error PDF's. They are combined in the bottom plot.

5.4 Forward-Backward Asymmetry in the Data

The Z forward-backward charge asymmetry of the CDF Run II data is measured from the di-electron invariant mass distributions of the forward events ($\cos\theta^* > 0$) and the backward events ($\cos\theta^* < 0$). The invariant masses of the selected events are filled into histograms with fourteen bins, which include an underflow bin and an overflow bin. Then the estimated background is subtracted from each bin. The two resulting distributions of the forward and backward events are unfolded by the response matrix separately. The A_{FB} in each bin is calculated from the unfolded numbers of the forward and backward events (Fig. 5.6 and Fig. 5.7). The integrated luminosity of the data is 364 pb^{-1}. The measurement is compared to the standard model leading order calculation and the χ^2 value is calculated as

$$\chi^2 = \sum_{i=1}^{N} \frac{(A_{FB}^{measured} - A_{FB}^{expected})^2}{(\sigma_{A_{FB}}^{expected})^2} = 10.9, \tag{5.11}$$

where the number of degrees of freedom is 12. The numbers of observed events and estimated backgrounds in each bins are listed in the Table 5.3.

Mass	Forward		Backward		Meas.	Stat.	Syst.	Total
(GeV/c^2)	#Evt's	#BG	#Evt's	#BG	A_{FB}	Error	Error	Error
50-65	97	9.6	120	7.6	-0.236	0.091	0.037	0.098
65-76	207	15.8	284	12.7	-0.389	0.086	0.069	0.110
76-82	330	9.5	394	7.3	-0.348	0.119	0.093	0.151
82-88	1791	8.9	1817	7.5	-0.102	0.066	0.096	0.117
88-94	6935	12.6	6295	10.1	0.044	0.011	0.010	0.015
94-100	1853	8.3	1348	6.8	0.471	0.052	0.064	0.083
100-106	333	8.5	169	6.0	0.303	0.083	0.050	0.097
106-120	288	18.6	130	13.3	0.432	0.065	0.036	0.074
120-140	166	14.9	58	11.9	0.555	0.079	0.034	0.086
140-200	140	22.7	53	14.7	0.512	0.079	0.054	0.096
200-300	45	7.5	15	4.1	0.571	0.132	0.051	0.140
300-600	10	0.8	3	0.7	0.668	0.265	0.074	0.275

Table 5.3: Numbers of data and background events in each mass bins. The measured A_{FB}'s and their uncertainties are shown.

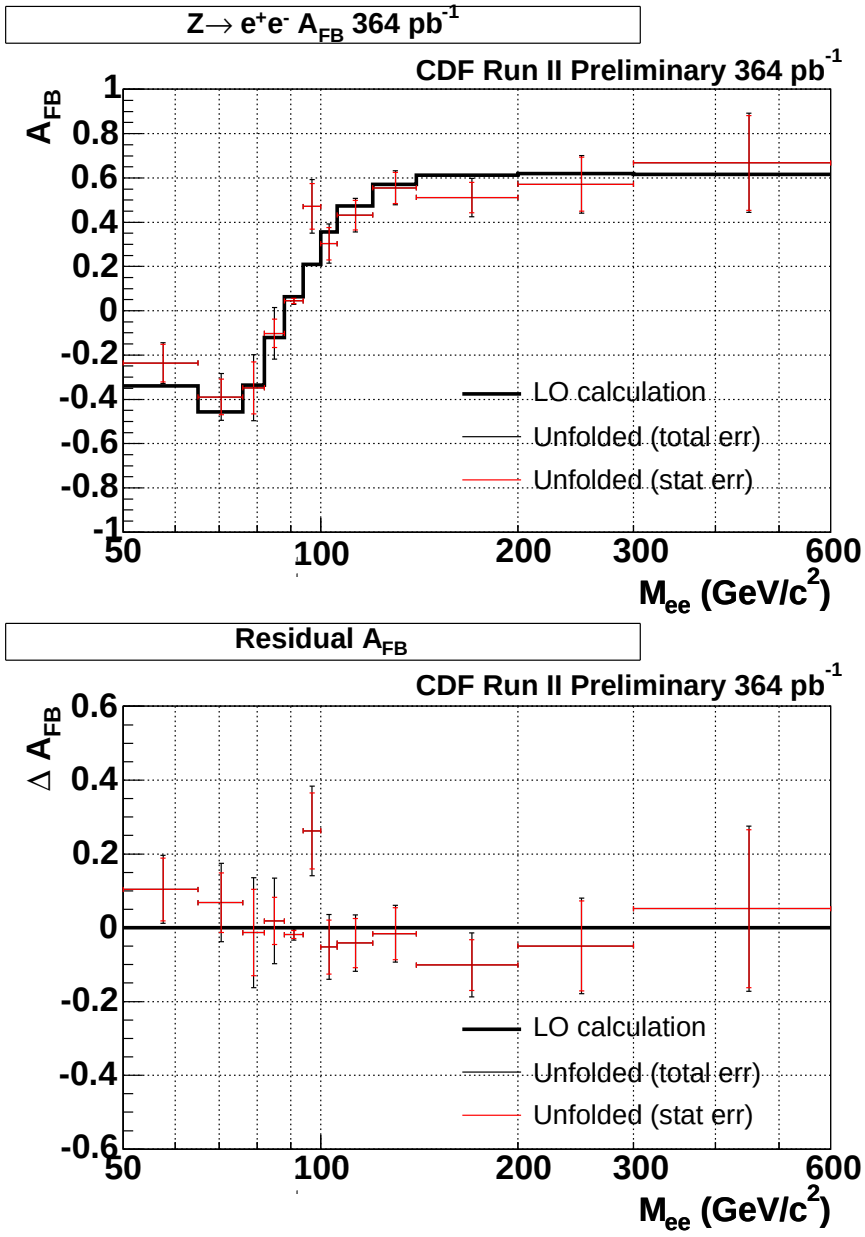

Figure 5.6: The A_{FB} of the data of 364 pb^{-1}. The χ^2 with respect to the leading order standard model is found to be 10.9, and the number of degrees of freedom 12.

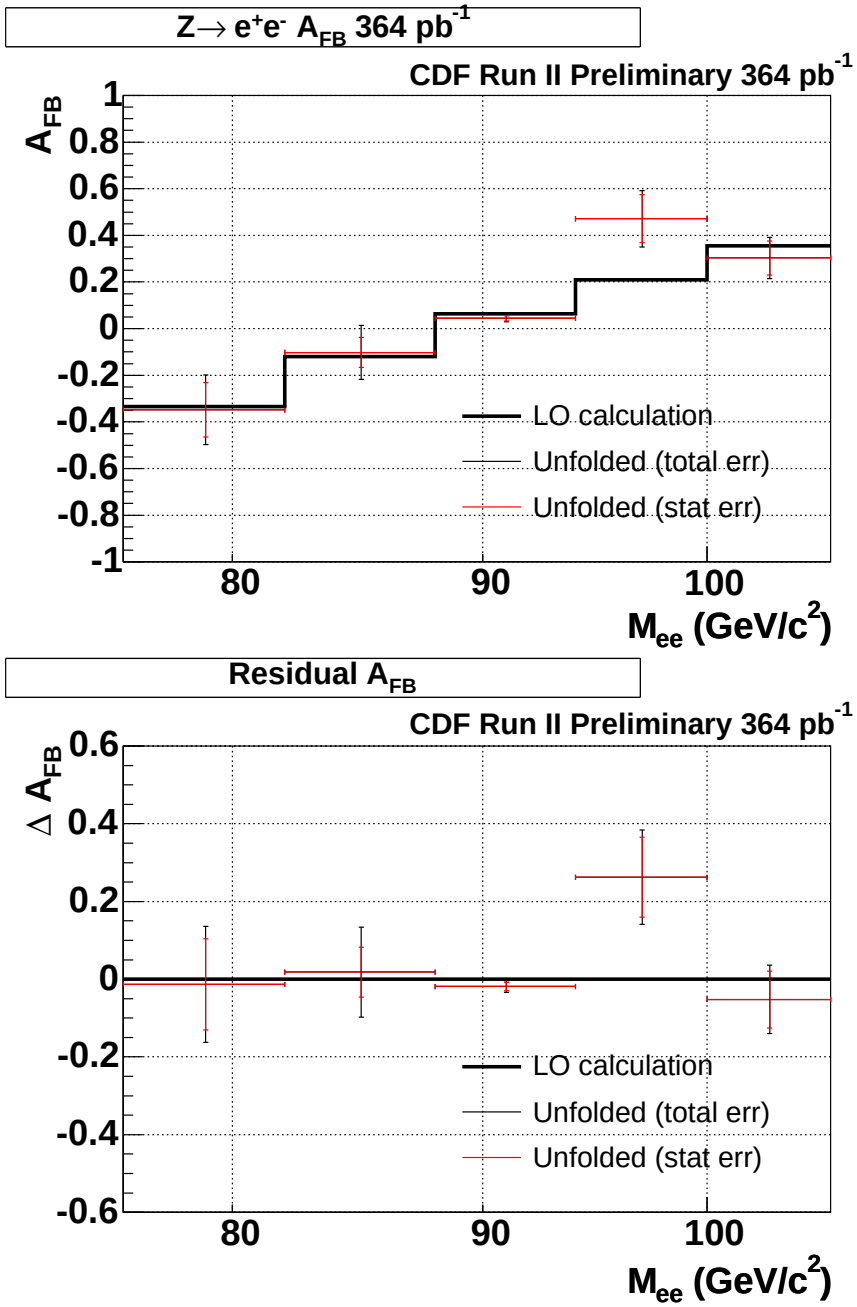

Figure 5.7: The unfolded A_{FB} zoomed into the Z pole region.

Chapter 6

A Search for Z'

An extra gauge boson Z' is postulated in many theories that extend the standard model. A Z' is an electrically neutral gauge boson with the same properties as the Z boson, except for its mass and its couplings to other particles. No compelling experimental evidence for the Z' has been found so far.

If a Z' exists with a high mass and its mass is within the reach of the Tevatron, the observed distributions of di-electron invariant mass, M_{ee}, and forward-backward asymmetry, A_{FB}, will deviate from the prediction of the standard model. A search for Z' by analyzing the M_{ee} and A_{FB} distributions with 0.45 fb^{-1} CDF Run II data is presented in this chapter [3].[1]

A search for Z' is an independent analysis, but is closely related to the measurement of the forward-backward charge asymmetry. While the two studies commonly analyze the di-electron final state, there are two major differences worth noting. First, while the A_{FB} measurement is a precision measurement over the whole invariant mass above 50 GeV/c^2, the Z' search concentrates on the high mass region above 200 GeV/c^2. Since the event cross-section at a very high mass becomes small, an

[1]The analysis was collectively led by Catalin Ciobanu, Sam Harper, Jedong Lee and Greg Veramendi.

extra data set of about 50 pb^{-1} was included. The data set was collected during a period when a layer of the COT detector was not working properly. Therefore the extra data included more background events. However when the cross-section is very small, increasing the sample size is important. Another difference is the methods used for the statistical interpretation of the result. For the A_{FB} measurement, the observation is unfolded with the method of matrix inversion to find the value of the A_{FB}, and the associated statistical uncertainty is reported. In case of the Z' search, on the other hand, the limit on the Z' mass is set with 95 % confidence limit. There are many statistical methods for setting the limits to a parameter, and we chose the method called CL_s because the method is known to be conservative [29].

6.1 Z' Production

In the presence of a Z', the scattering amplitude for the process $f\bar{f} \to e^+e^-$ can be expressed as a sum of the terms arising from the exchanges of the virtual photon γ^*, the Z boson, and the Z' as following:

$$\begin{aligned} A_{ij} &\equiv A(f_i\bar{f} \to e_j^- e^+) \\ &= -Qe^2 + \frac{\hat{s}}{\hat{s} - M_Z^2 + iM_Z\Gamma_Z} c_i^Z(f) c_j^Z(e) \\ &\quad + \frac{\hat{s}}{\hat{s} - M_{Z'}^2 + iM_{Z'}\Gamma_{Z'}} c_i^{Z'}(f) c_j^{Z'}(e), \end{aligned} \tag{6.1}$$

where $i, j = L$ or R for left-handed and right-handed fermions, respectively. The coupling constants of the Z and Z' to the fermions $c_i^Z(f)$, $c_j^Z(e)$, $c_i^{Z'}(f)$, and $c_j^{Z'}(e)$ are discussed in the sections 1.2 and 1.3. $\hat{s}$ denotes the square of the center of mass system energy, and $Q = -1$, the electric charge of an electron. Constraints from precision measurements of the couplings of the Z restrict the mixing between Z and

Z' to be very small [7]; therefore, it is ignored in Eq. (6.1). The differential cross section for the process can be written as

$$\frac{d\hat{\sigma}(f\bar{f}\to e^+e^-)}{d\cos\theta^*} = \frac{1}{128\pi\hat{s}}[(|A_{LL}|^2+|A_{RR}|^2)(1+\cos\theta^*)^2+(|A_{LR}|^2+|A_{RL}|^2)(1-\cos\theta^*)^2]. \tag{6.2}$$

At the Tevatron, the fermions in the initial state are a pair of quark and anti-quark out of a proton and anti-proton. The cross section for the process $p\bar{p}\to e^+e^-$ is obtained by integrating the parton distribution functions.

$$\frac{d\sigma(p\bar{p}\to e^+e^-)}{d\cos\theta^*} = \frac{1}{3}\frac{1}{3}3\sum_{(f,\bar{f})}\int_0^1 dx_1\int_0^1 dx_2 f_f(x_1)f_{\bar{f}}(x_2)\frac{d\hat{\sigma}(f\bar{f}\to e^+e^-)}{d\cos\theta^*} \tag{6.3}$$

$$= \frac{1}{3}\sum_{(f,\bar{f})}\int d\tau\int dy f_f(x_1)f_{\bar{f}}(x_2)\frac{d\hat{\sigma}(f\bar{f}\to e^+e^-)}{d\cos\theta^*}, \tag{6.4}$$

where $\tau = M^2/s = x_1x_2$ and $(f,\bar{f})$ represents all the possible combinations of $q\bar{q}$ pairs from $p\bar{p}$ collisions. The factor $\frac{1}{3}$ accounts for the need to match the QCD "color" charges of the partons in the colorless final state. The expression is differentiated with respect to the mass of the exchanged boson M, where $M^2 = \hat{s}$, to give the two-dimensional differential cross section

$$\frac{d\sigma}{dM\ d\cos\theta^*} = \frac{2M}{s}\frac{d}{d\tau}\left(\frac{d\sigma(p\bar{p}\to e^+e^-)}{d\cos\theta^*}\right)$$

$$= \frac{2M}{3s}\sum_{(f,\bar{f})}\frac{d\hat{\sigma}(f\bar{f}\to e^+e^-;\hat{s}=M^2)}{d\cos\theta^*}\int_{\log\sqrt{\tau}}^{-\log\sqrt{\tau}} dy f_f(x_1)f_{\bar{f}}(x_2), \tag{6.5}$$

where $x_{1,2} = \sqrt{\tau}e^{\pm y}$.

The mass of the exchanged boson M is not directly measurable. In the $\gamma^*/Z/Z'\to e^+e^-$ decay, the di-electron invariant mass M_{ee} is used as an estimate for M. However, the measured M_{ee} is not equal to M due to the detector resolution and the final state QED radiation. Those effects are estimated from the Monte Carlo simulation.

6.2 Signal Modeling

The scattering mediated by Z' bosons is expected to interfere with the standard model γ^*/Z exchange (Eq. 6.1); therefore the γ^*/Z production is not labeled as background. Instead, the $\gamma^*/Z/Z'$ production is referred to as the Z' *signal*, and the γ^*/Z is referred to the standard model Drell-Yan production. All other standard model processes that contribute to the di-electron final state will be designated as *background*.

The Z' is parameterized in a model-independent way [16] (section 1.3), with three parameters: the Z' mass $M_{Z'}$, the coupling strength of the extra $U(1)$ gauge group $g_{Z'}$, and a variable x that determines the coupling constants as shown in the Table 1.2.

In this analysis, a large number of Z' models with different parameters are tested and thus having a fully simulated sample of Z' events for each model is not practically feasible. As a solution to this problem, one large sample of the process $q\bar{q} \to \gamma^* \to e^+e^-X$ is generated by PYTHIA [32] to determine the CDF detector response. The response is parameterized in terms of a two-dimensional grid of M_{ee} and $\cos\theta^*$ with the step sizes of 10 GeV/c^2 in M_{ee} and 0.25 in $\cos\theta^*$. The discrete bins are labeled by integers from 1 to 800 in the region $50 < M_{ee} < 1050$ GeV/c^2 and $-1 < \cos\theta^* < 1$. For each event in the Monte Carlo sample, the bin index j at the generation-level and the bin index i at the simulation-level are recorded. The index j is calculated before the detector simulation or QED radiation, from the generated mass of γ^*, and the $\cos\theta^*$ calculated from the decay $\gamma^* \to e^+e^-$. The index i is calculated after the full detector simulation and object reconstruction, from the M_{ee} and $\cos\theta^*$ calculated from the four-momenta of the reconstructed e^+ and e^-. The acceptance matrix A_{ij}

is defined as

$$\mathcal{N}_i = \sum_{j}^{N_{bins}} A_{ij} N_j, \tag{6.6}$$

where $\mathcal{N}_i$ is the total number of simulation-level events that populate bin i, N_j is the number of generation-level events in bin j, and N_{bins} is the total number of the bins. This is illustrated in Fig. 6.1.

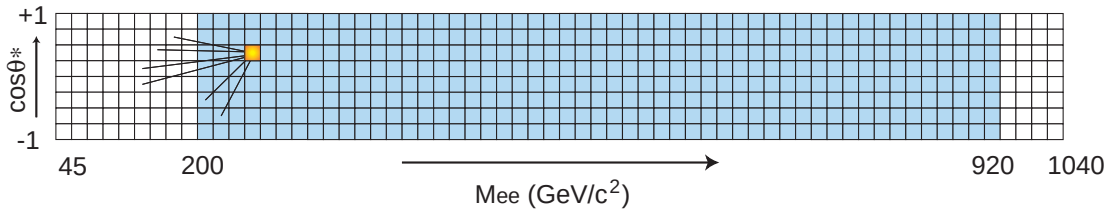

Figure 6.1: A diagram showing how the acceptance matrix A_{ij} is defined. The Z' signature is searched in the blue region with $200 < M_{ee} < 920$ GeV/c^2.

For a given Z' model, the expected numbers of observed events in each bin in the two-dimensional space (M_{ee}, $\cos\theta^*$), denoted by a *template*, is calculated. The calculation is based upon a customized leading order (LO) cross-section of the process $\gamma^*/Z/Z' \rightarrow e^+e^-$ within each bin in the (M_{ee}, $\cos\theta^*$) space. The leading order results are multiplied by a K-factor which is the ratio between the next-to-next-to-leading order (NNLO) and leading order cross-sections as a function of mass [22]. The K-factor corrected cross-sections are multiplied by the luminosity $\mathcal{L} = 448$ pb^{-1}. The expected number of observed events in each bin is derived from Eq. (6.6). The standard model Drell-Yan template is constructed in a similar manner.

6.3 Background

As discussed in chapter 4, the sources of background to the processes $p\bar{p} \rightarrow \gamma^*/Z/Z' \rightarrow e^+e^-X$ are:

- Di-jet events where the jets are misidentified as electrons,
- $W + X \rightarrow e\nu + X$, where X is a photon or a jet misidentified as an electron,
- $\gamma^*/Z \rightarrow \tau^+\tau^- \rightarrow e^+e^-\nu_\tau\nu_e\bar{\nu_\tau}\bar{\nu_e}$,
- $W^+W^- \rightarrow e^+e^-\nu_e\bar{\nu_e}$,
- $W^\pm Z$ where $Z \rightarrow e^+e^-$,
- $t\bar{t} \rightarrow e^+e^-\nu_e\bar{\nu_e}b\bar{b}$.

Di-jet events are the dominant source of background. The number of di-jet background is estimated from the data using the 'fake rate', the probability that a jet is misidentified as an electron. The other backgrounds are estimated using Monte Carlo simulations. Table 6.1 shows the number of events expected in the sample of 448 pb^{-1} for each process. The systematic uncertainties on these background estimates reflect the 6 % uncertainty on the integrated luminosity, the 5 % uncertainty on the acceptances, and the uncertainties on the theoretical production cross sections. Note that the background for the Z' analysis is estimated by the 'fake rate' method, which suffers a large uncertainty due to the trigger bias. The isolation method introduced in chapter 4 provides more precise determination of the di-jet background.

The distributions of M_{ee} and $\cos\theta^*$ of the data are compared to the standard model Drell-Yan and background predictions in Figs. 6.2 and 6.3. The $\cos\theta^*$ distributions

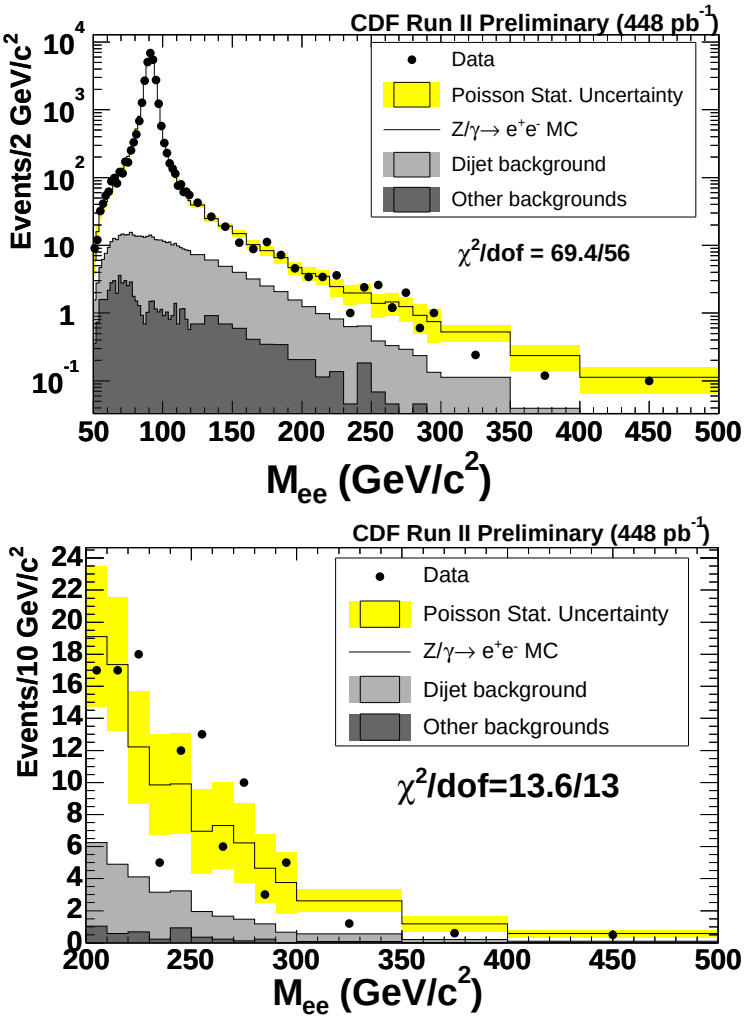

Figure 6.2: Invariant mass distribution of the data compared to the prediction for the standard model Drell-Yan and backgrounds. The round points are the data, the open histogram is the standard model Drell-Yan, and the shaded histograms are the background predictions. The histograms are stacked. The agreement for $M_{ee} > 100$ GeV/c^2 is $\chi^2/\text{dof} = 16.9/19$.

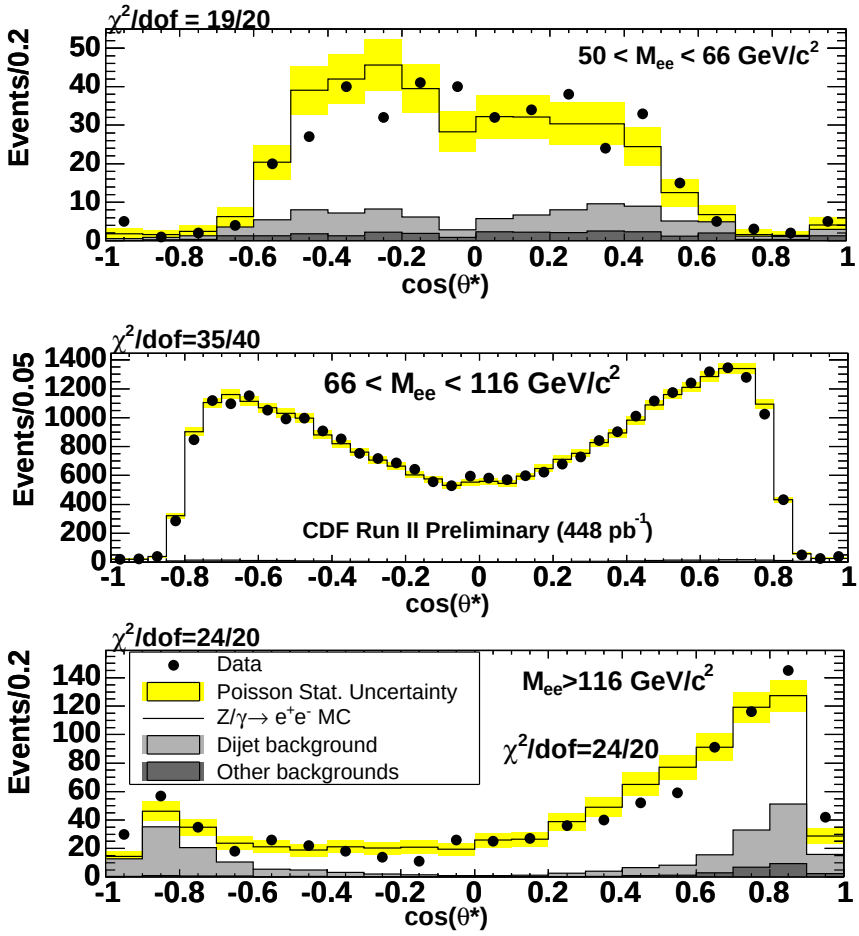

Figure 6.3: Distributions of $\cos\theta^*$ for the three mass regions. The data is compared to the predictions of the standard model Drell-Yan and backgrounds. The round points are the data, the open histograms are the predictions from Drell-Yan Monte Carlo simulation, and the shaded histograms are the predictions from background.

Process	Events Expected		
	C-C	C-P	$M_{ee} > 200\ GeV/c^2$
Di-jet	43 ± 32	450 ± 230	29 ± 14
$W + \gamma \to e\nu + \gamma$	1.9 ± 0.4	48.3 ± 9	4.9 ± 0.1
$\gamma^*/Z \to \tau^+\tau^-$	11.6 ± 2.2	17.6 ± 3.1	0.13 ± 0.03
$W^+W^- \to e^+e^-\nu_e\bar{\nu}_e$	7.7 ± 1.5	9.3 ± 1.8	1.2 ± 0.2
$W^{\pm}Z$ where $Z \to e^+e^-$	6.3 ± 1.2	7.9 ± 1.6	0.19 ± 0.04
$t\bar{t} \to e^+e^-\nu\bar{\nu}b\bar{b}$	5.1 ± 1.0	3.3 ± 0.6	0.65 ± 0.12
Total Backgrounds	75 ± 33	540 ± 230	36 ± 14

Table 6.1: Summary of expected backgrounds to the Z' search. Cross-sections for the electroweak and top processes are taken from the references [15, 14, 12, 17]. Monte Carlo estimates are normalized to the integrated luminosity of 448 pb^{-1}.

are made from three samples in different mass regions; $50 < M_{ee} < 66$ GeV/c^2, $66 < M_{ee} < 116$ GeV/c^2, and $M_{ee} > 116$ GeV/c^2. The M_{ee} and $\cos\theta^*$ distributions from the Drell-Yan and background predictions agree well with the data. Therefore, no compelling evidence for a contribution from Z' boson is found in the data, and we will set limits to restrict the possible Z' parameter space.

6.4 Statistical Method

The method of parameter estimation used for the Z' search is called CL_s [29], which has been previously used to set limits for the Higgs boson mass at LEP II experiments [9]. In application of the CL_s, the data are tested against two mutually exclusive hypotheses:

- The null hypothesis ($H0$): data are described by the standard model γ^*/Z exchange and backgrounds.

- The test hypothesis ($H1$): data are described by the $\gamma^*/Z/Z'$ exchange and

backgrounds.

The probability to have the $(M_{ee},\ \cos\theta^*)$ distribution of the data from the null hypothesis $H0$ is derived from the Poisson statistics as

$$P(\text{data}|H0) = \prod_{i=1}^{N_{bins}} P^i = \prod_{i=1}^{N_{bins}} \frac{e^{\mathcal{N}_i^{H0}} \cdot (\mathcal{N}_i^{H0})^{d_i}}{d_i!}, \tag{6.7}$$

and similarly for $P(\text{data}|H1)$. In the above expression, $\mathcal{N}_i$ and d_i are the expected and observed numbers of events in the bin i, respectively. A test statistic Q is defined as

$$Q = -2 \cdot \ln \frac{P(\text{data}|H1)}{P(\text{data}|H0)} = \text{const} - 2 \cdot \sum_{N_{bins}}^{i=1} d_i \cdot \ln \frac{\mathcal{N}_i^{H1}}{\mathcal{N}_i^{H0}}. \tag{6.8}$$

The expected distribution of the test statistic Q is found from the Monte Carlo pseudo-experiments. Pseudo-experiments are drawn from the null hypothesis $H0$ and the Z' hypothesis $H1$. The two distributions should be well separated in order for the experiment to be sensitive to a certain Z' model. Fig. 6.4 shows well separated distributions of $Q(H0)$ and $Q(H1)$ for a particular Z' of $B-xL$ class with $M_{Z'} = 440$ GeV/c^2, $g_{Z'} = 0.03$, and $x = 10$. Assuming that the value Q_{obs} is observed from the data, three quantities CL_b, CL_{s+b}, and CL_s can be defined in terms of $Q(H0)$ and $Q(H1)$ as follows.

$$CL_{s+b}(Q_{obs}) = P(Q \leq Q_{obs}|H1) = \int_{Q_{obs}}^{\infty} Q(H1) \cdot dQ \tag{6.9}$$

$$CL_b(Q_{obs}) = P(Q \leq Q_{obs}|H0) = \int_{Q_{obs}}^{\infty} Q(H0) \cdot dQ \tag{6.10}$$

$$CL_s(Q_{obs}) = \frac{CL_{s+b}}{CS_b} \tag{6.11}$$

The 95 % confidence level exclusion region for the signal plug background hypothesis is defined by $CL_s < 0.05$.

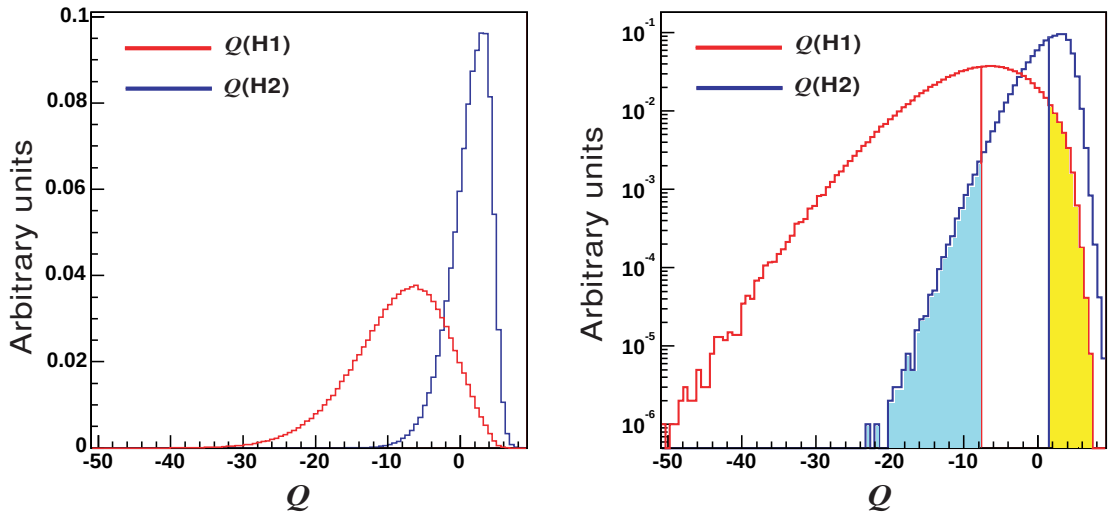

Figure 6.4: The distributions of test statistics Q from pseudo-experiments. The separation between the two distributions $Q(H0)$ and $Q(H1)$ is an indicator of the exclusion potential. The expected CL_s is 6.5 % and corresponds to the yellow area.

The systematic uncertainties are simultaneously accounted for when the pseudo-experiments are generated, by fluctuating the expected production cross-section. The amount of the fluctuation is determined by the change of the cross-section due to the sources of the systematic uncertainties. For each pseudo-experiment, the fluctuated cross-sections for each bin is determined, from which a pseudo-experiment is drawn. Then, the resulting $(M_{ee},\ \cos\theta^*)$ templates d_i are fed into Eq. (6.8) and the value of CL_s is subsequently calculated based on the $Q(H0)$ and $Q(H1)$ distributions. The main sources of systematic uncertainties are listed below.

- **Energy Scale and Resolution.** To estimated the effect of the energy scale and resolution, the energy scale in the central and plug region is shifted by 1 %. At the same time, the calorimeter resolution is varied by 3 % in both

the central and plug calorimeters. The shifted acceptance matrix A_{ij} due to the change is denoted by A'_{ij}. The Q distributions are calculated with A'_{ij} for several representative models. The expected CL_s increased by up to 7 % due to this effect.

- **Uncertainties in the Background Estimations.** Di-jet background is estimated from the 'fake rate', the probability that a jet is misidentified as an electron. The uncertainty is found from the discrepancies between the fake rates found from jet samples. The expected CL_s values change by up to 0.5 % due to this effect.

- **Uncertainty of the Parton Distribution Functions (PDF).** The PDF factors into the leading order Z' cross-section calculation. The uncertainty in the cross-section due to the PDF uncertainty is estimated from the 40 PDF sets obtained by shifting the 20 eigenvectors up or down by the fit uncertainties. The impact on the expected CL_s is found to be negligible.

- **Luminosity, Electron ID Efficiency, and Acceptance Uncertainties.** The effects are grouped together because they affect on the overall number of events expected, but not on the shape of the (M_{ee}, $\cos\theta^*$) templates. Taking a conservative uncertainty of 20 %, the shift of up to 5 % in the expected CL_s is measured.

6.5 Results

No significant evidence of Z' signal is found. The 95 % confidence level lower limits on the mass of chosen Z' models [23] are shown in the Table 6.2. The Z' exclusion regions in the (M_{ee}, $g_{Z'}$, x) space is mapped out in Fig. 6.5, using the parameterization discussed in Ref. [16]. The horizontal axes of the plots are the variable x, which determines the Z' couplings to fermions. Therefore a higher sensitivity, or higher $M_{Z'}$ limit, is observed with increasing $|x|$, as expected. A similar argument holds for the overall coupling strength $g_{Z'}$. The exclusion from the LEP II experiment is taken from the Ref. [16] and compared to the CDF limits. CDF limits are found to be more sensitive in the case of small coupling constants.

Z' Model	Z_{SM}	Z_χ	Z_ψ	Z_η	Z_I
Observed Limit (GeV/c^2)	845	720	690	715	625

Table 6.2: The observed 95 % confidence level lower limits on $M_{Z'}$ for chosen Z' models. Z_{SM} is a Z' with the same coupling constants as the Z boson. Other Z' models arise from different symmetry breaking scenarios of the E_6 model.

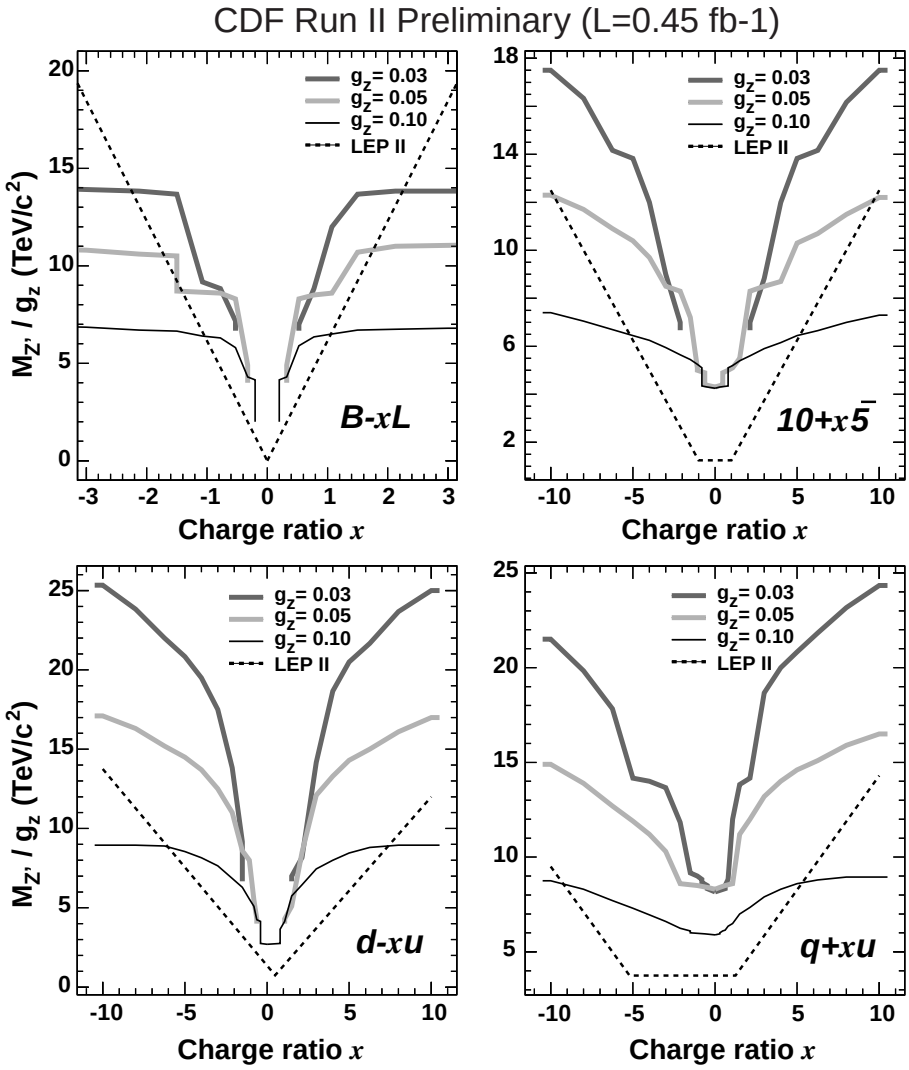

Figure 6.5: Exclusion contours for the Z' model-lines $B - xL$, $10 + x\bar{5}$, $d - xu$, and $q + xu$. The dotted lines represent the exclusion boundaries derived in Ref. [16] from the LEP II results [1]. The region below each curve is excluded by 95 % confidence level. Only models with $M_{Z'} > 200$ GeV/c^2 are tested, which causes the gap at small $|x|$ for some models.

Chapter 7

Publication of Search for $Z' \to e^+e^-$

(Published in Phys. Rev. Lett. 96:211801, 2006.)

Search for $Z' \to e^+e^-$ Using Dielectron Mass and Angular Distribution

The CDF Collaboration
(Dated: January 9, 2007)

We report results from a search for Z' bosons in high-mass dielectron events produced in $p\bar{p}$ collisions at $\sqrt{s} = 1.96$ TeV. The data were recorded with the CDF II detector at the Fermilab Tevatron and correspond to an integrated luminosity of 0.45 fb^{-1}. To identify the $Z' \to e^+e^-$ signal, both the dielectron invariant mass distribution and the angular distribution of the electron pair are used. No significant evidence of signal is found, and 95% confidence level lower limits are set on the Z' mass for several models.

Source	$Z/\gamma \to e^+e^-$	Dijet	Diboson	Total SM	Observed
Events	80.0 ± 8.0	28^{+14}_{-17}	6.8 ± 1.4	115^{+19}_{-18}	120

TABLE I: SM estimates for dielectron candidates with $M_{ee} > 200$ GeV/c^2. The SM Drell-Yan contribution is estimated as described in the text. The diboson ($W\gamma$, WW, WZ) contributions are estimated using PYTHIA [18] and normalizing to the theoretical cross sections [19–21]. The dijet contribution is estimated using data.

Most extensions of the Standard Model (SM) gauge group predict the existence of electrically-neutral, massive gauge bosons commonly referred to as Z' [1–5]. The leptonic decays $Z' \to \ell^+\ell^-$ provide the most distinct signature for observing the Z' signal at a hadron collider. In two recent publications, the Collider Detector at Fermilab (CDF) Collaboration has set limits on different Z' models by analyzing the invariant mass ($M_{\ell\ell}$) spectrum of the dielectron, dimuon, and ditau final states, using a dataset corresponding to an integrated luminosity of roughly 0.2 fb^{-1} [6, 7]. Besides the dilepton mass $M_{\ell\ell}$, it has been shown that the angular distribution of the dilepton events can also be used to test the presence of a finite-width Z' boson by detecting its interference with the SM Z boson [8]. In this Letter, for the first time at a hadron collider, the massive resonance search technique ($M_{\ell\ell}$ analysis) is extended to include dilepton angular information to identify $Z' \to e^+e^-$ decays in 0.45 fb^{-1} of data accumulated with the CDF II detector. As integrated luminosity increases, the sensitivity of the standard $M_{\ell\ell}$ analysis tends to plateau; adding the angular information starts to become an important handle for extending the Z' exclusion reach and discovery potential. Many of the theoretical Z' models are surveyed, and results are reported for the sequential Z'_{SM}, the canonical superstring-inspired E6 models Z_χ, Z_ψ, Z_η, Z_I, Z_N, $Z_{\rm sec}$ [9, 10], the "littlest" Higgs Z_H model [4, 5], the four generic model-lines of Ref. [2], and contact-interaction searches. No significant evidence of a Z' signal is found, and the tightest constraints to date are set on these models.

The CDF detector is described in detail elsewhere [11]. For this analysis, the relevant subdetector systems are the central tracking chamber (COT) and the central and the plug calorimeters. The COT is a 96-layer open cell drift chamber immersed in a 1.4 Tesla magnetic field, used to measure charged particle momenta within the pseudorapidity range $|\eta| < 1.0$ [12]. Surrounding the COT are the electromagnetic (EM) and hadronic (HAD) calorimeters, segmented in projective $\eta - \phi$ towers pointing to the nominal collision point $z = 0$. The central calorimeters measure the energies of particles within the range $|\eta| < 1.1$, while the plug calorimeters extend the range to $1.1 < |\eta| < 3.6$. Two triggers were used to select the data for this analysis. The main trigger requires two high-E_T EM clusters in the calorimeter while a backup trigger accepts events with a single electron candidate with very high E_T and looser electron-selection requirements.

For this analysis, events are selected with two high-E_T electron candidates [13, 14], of which at least one is required to have been measured in the central calorimeter. A matching COT track is required for all central candidates. Events with same-sign central electron pairs are rejected, and an isolation condition for the energy found within a cone of angular radius $R = \sqrt{(\Delta\eta)^2 + (\Delta\phi)^2} = 0.4$ around the electron is imposed for electron candidates. The angular distribution is measured using $\cos\theta^*$, where θ^* is the angle between the electron and the incoming quark in the Collins-Soper frame.

The Z' production is expected to interfere with the SM Drell-Yan Z/γ^* process, altering the $\cos\theta^*$ distribution. For this reason, the Z/γ^* process is not labeled as a "background". Instead, the $Z'/Z/\gamma^*$ is referred as the Z' *signal*, while the SM Z/γ^* is referred as the *SM Drell-Yan* production. The term *background* will be used to designate all other SM processes (excluding Z/γ^*) expected to contribute to the dielectron final state sample. Of these background sources, the most important are the dijet events in which jets are misidentified as electrons, and diboson events (see Table I). The dijet background is estimated using the probability for a jet to be misidentified as an electron ("fake rate") which is measured in the jet data. All non-dijet backgrounds are estimated via Monte Carlo simulation. Other background processes such as ditau events $Z/\gamma^* \to \tau^+\tau^- \to e^+e^-\nu_\tau\nu_e\bar{\nu_\tau}\bar{\nu_e}$, or top-quark production $t\bar{t} \to e^+e^-\nu_e\bar{\nu_e}b\bar{b}$ have negligible contributions in the high-mass region considered for this analysis.

A leading-order calculation is used as the starting point to construct the signal and SM Drell-Yan Monte Carlo distributions [15]. A next-to-next-to-leading order mass-dependent $K-$factor [16] is then factored in, followed by a parameterization of the CDF detector response [17] to dielectron events. This parameterization is extracted by running the CDF simulation on a large sample of dielectron events generated with PYTHIA [18] in such a way that the distributions in M_{ee} and $\cos\theta^*$ of the electron pair are roughly uniform.

To isolate the Z' signal, two variables are used: the invariant mass of the electron-positron pair M_{ee} in 10 GeV/c^2 bins, and $\cos\theta^*$ in 0.25 bins. The bidimensional distribution ($M_{ee}, \cos\theta^*$) of the CDF data is used to test two mutually exclusive hypotheses: 1) the *test* hypothesis (*H1*), where data points are described by the Z' signal and background

3

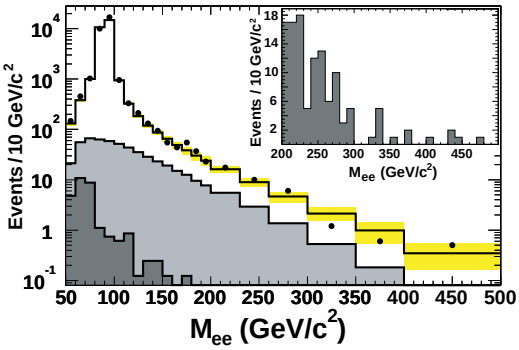

FIG. 1: M_{ee} distribution of the data (points) compared to the prediction for SM Drell-Yan and backgrounds. The individual contributions are stacked as follows: other backgrounds (dark grey), dijet background (light grey), and SM Drell-Yan (open). The inset shows the M_{ee} distribution of high-mass data events using a bin size of 10 GeV/c^2.

combined distributions, and 2) the *null* hypothesis (*H2*), where data are described by SM Drell-Yan and background combined distributions. A test statistic Q is defined as [22]:

$$Q = -2 \cdot \ln \frac{P(\text{data}|H1)}{P(\text{data}|H2)} = \text{const} - 2 \cdot \sum_{i=1}^{N_{bins}} d_i \cdot \ln \frac{\mathcal{N}_i^{H1}}{\mathcal{N}_i^{H2}}$$

where N_{bins} denotes the total number of bins in the $(M_{ee}, \cos\theta^*)$ plane, d_i is the observed number of events in bin i, while $\mathcal{N}_i^{H1}$ and $\mathcal{N}_i^{H2}$ are the expected numbers of events in bin i in the *H1* or *H2* hypotheses, respectively.

Several sources of systematic uncertainty affect our measurement. First, a relative uncertainty of 10% on the total rate is incurred due to uncertainties in the luminosity measurement, the dielectron detector acceptance and electron identification efficiency, and the LO calculation. The second dominating effect is the electron energy scale and resolution uncertainty, which modifies the shape of the M_{ee} and $\cos\theta^*$ distributions. The third source is the uncertainty in the background (particularly dijet) estimations. The dijet prediction uncertainty is extracted from the differences in the fake rate measured in kinematically different jet samples. Finally, the uncertainty related to the choice of the parton distribution functions set (CTEQ6M [23]) is evaluated using the Hessian method advocated in Ref. [24], and found to have a negligible effect on our results.

For the different Z' models (*H1* hypotheses) mentioned in the beginning of this Letter, a large number of simulated experiments are generated to extract the distributions $Q(H1)$ and $Q(H2)$. The systematic uncertainties are accounted for as described in Ref. [22]. The Q distributions are in turn used to verify the consistency of the data with the test or null hypotheses, as well as extracting the expected exclusion reach. The CDF data is found to be consistent with the null (no Z') hypothesis; Figs. 1 and 2 show good agreement between data and Monte Carlo SM distributions, for the M_{ee} and $\cos\theta^*$ distributions. For illustration, Fig. 2 also presents the forward-backward asymmetry A_{FB} [14] defined as $(N_+ - N_-)/(N_+ + N_-)$, where N_+ and N_- are the numbers of forward ($\cos\theta^* > 0$) and backward ($\cos\theta^* < 0$) events in the given M_{ee} range. The A_{FB} plot is a common way of representing the mass dependence of the angular distribution.

The sequential Z'_{SM} boson, which has the same couplings to fermions as the SM Z boson, is excluded by our data up to a mass of 850 GeV/c^2. It is noted here that using the dielectron invariant mass alone would require roughly 25% more data for the same Z'_{SM} exclusion. In general, the improvement provided by including the $\cos\theta^*$ spectrum depends strongly on the particular Z' under investigation and the integrated luminosity being analyzed. Other Z' theories include grand unification E6 models [1, 3, 9], where the E6 gauge group breaks down as E6$\to$SO(10)$\times$U(1)$_\psi$ $\to$SU(5)$\times$U(1)$_\chi\times$U(1)$_\psi$, and the SM gauge structure results from breaking down the SU(5) group. Therefore, an extra Z' will be a combination of the two U(1)'s: $Z_{\theta_{E6}} = Z_\psi \sin\theta_{E6} + Z_\chi \cos\theta_{E6}$. Table II lists the expected and observed 95% confidence level lower limits on the $M_{Z'}$ for the Z_χ, Z_ψ, Z_η, Z_I, Z_N, and the secluded Z_{sec} E6 models. The results are shown for the two extreme scenarios in which either none or all of the decay channels of the Z' into non-SM particles are open [10].

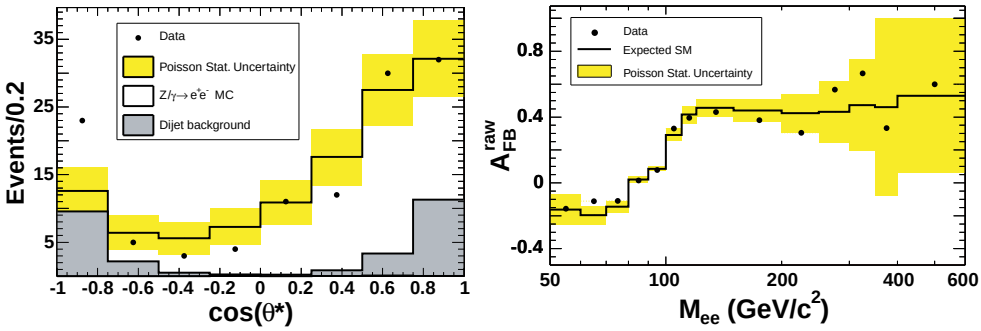

FIG. 2: Top: Distributions of $\cos\theta^*$ for the high mass region $M_{ee} > 200$ GeV/c^2. The points are the data, the open histograms are the predictions from Drell-Yan Monte Carlo simulation, and the shaded histograms are the background predictions. The individual contributions are stacked. Bottom: distributions of the forward-backward asymmetry A_{FB}^{raw} for the data (points) and predicted SM processes (histogram). The superscript "raw" is used here to emphasize that no detector acceptance, background subtraction, or efficiency corrections are applied.

Z' Model	Z_{SM}	Z_χ	Z_ψ	Z_η	Z_I	Z_N	$Z_{\rm sec}$	Z_H^1	Z_H^2	Z_H^3	Z_H^4
Exp. limit (GeV/c^2)	860	735 (595)	725 (455)	745 (495)	650 (515)	710 (470)	675 (550)	625	765	835	910
Obs. limit (GeV/c^2)	850	740 (610)	725 (435)	745 (520)	650 (525)	710 (450)	680 (565)	625	760	830	900

TABLE II: Z' exclusion summary: expected and observed 95% C.L. lower limits on $M_{Z'}$ for the sequential, the canonical E6, and the littlest Higgs Z' models. For the E6 models we show the default results where the Z' decays to SM particles only, followed by (in parentheses) the limits in the assumption that all decay channels to non-SM particles are open [10]. The littlest-Higgs bosons Z_H^1, Z_H^2, Z_H^3, and Z_H^4 correspond to $\cot\theta_H = 0.3$, 0.5, 0.7, and 1.0, respectively.

Another class of theories addressing the electroweak symmetry breaking and the hierarchy problem are the little Higgs theories [4], where Z'_H bosons are predicted in order to stabilize the Higgs mass against quadratically divergent one-loop radiative corrections. In the minimal model of this type - the littlest Higgs, the Z'_H couples to left-handed fermions only, and these couplings are parameterized as functions of the mixing angle cotangent $\cot\theta_H$ [5]. Our results for $\cot\theta_H = 0.3$, 0.5, 0.7, and 1.0 are shown in Table II, and improve the results reported in [6].

The recent phenomenological study of Z' production at the Tevatron reported in [2] has also been investigated. This study uses simple constraints such as generation-independent fermion charges and gauge anomaly cancellations to reduce the number of parameters (17) required to define an arbitrary Z' model. The Z' couplings to fermions are expressed as first-degree polynomials in a real variable x. Four sets of rational coefficients for these polynomials are found, defining four types of Z' models, or model-lines: $B - xL$, $d - xu$, $q + xu$, $10 + x\bar{5}$. Within each of these four model-lines, a certain Z' boson is specified by three parameters only: its mass $M_{Z'}$, the coupling strength g_Z, and the value of x. These parameters are varied to obtain the exclusion regions shown in Fig. 3. This method yields a higher sensitivity (better exclusion) than the LEP results ([2]) for small $|x|$ values and coupling strengths $0.01 \lesssim g_z \leq 0.10$.

Finally, Z' constraints can be derived from searches for contact interactions, if the collider energy is far below the Z' pole [2, 25, 26]. An effective Lagrangian for the $qqee$ contact interaction can be written as: $\sum_q \sum_{i,j=L,R} \frac{4\pi\eta}{\Lambda_{ij}^2} \bar{e}_i \gamma^\mu e_i \bar{q}_j \gamma_\mu q_j$, where Λ is the scale of the interaction, and $\eta = \pm 1$ determines the interference structure with the Z/γ^* amplitudes [27]. A generation-universal interaction is assumed and lower limits are measured for Λ in six helicity structure scenarios: LL, LR, RL, RR, VV and AA (Table III) [28].

In conclusion, we have searched for Z' decays to e^+e^- pairs in 0.45 fb^{-1} of data accumulated with the CDF

Interaction	LL	LR	RL	RR	VV	AA
Λ_{qe}^+ limit (TeV/c^2)	3.7	4.7	4.5	3.9	5.6	7.8
Λ_{qe}^- limit (TeV/c^2)	5.9	5.5	5.8	5.6	8.7	7.8

TABLE III: 95% C.L. lower limits for the contact interaction mass scales.

FIG. 3: Exclusion contours for the $B - xL$, $10 + x\bar{5}$, $d - xu$, and $q + xu$ Z' models. The dotted lines represent the indirect LEP II exclusion boundaries, taken from Ref. [2]. The region below each curve is excluded by our data at 95% C.L..

II detector. To strengthen this search, the reconstructed dielectron invariant mass M_{ee} spectrum and the angular distribution of the electron pair $\cos\theta^*$ are analyzed simultaneously. This is the first study of this kind at the Tevatron, and it opens up a new avenue for exploring the Z' production in the femtobarn luminosity regime. Many of the Z' models encountered in the literature are surveyed, no significant evidence for signal is found, and 95% C.L. limits are set on these models. Constraints are also placed on contact interaction mass scales far above the Tevatron energy scale. Finally, exclusion contours for the generic Z' model-lines advocated in Ref. [2] are mapped out. In comparison to the LEP contact interaction Z' search results given in [2], our results exhibit higher sensitivity in the small $|x|$ and small g_z regions.

We thank the Fermilab staff and the technical staffs of the participating institutions for their vital contributions. This work was supported by the U.S. Department of Energy and National Science Foundation; the Italian Istituto Nazionale di Fisica Nucleare; the Ministry of Education, Culture, Sports, Science and Technology of Japan; the Natural Sciences and Engineering Research Council of Canada; the National Science Council of the Republic of China; the Swiss National Science Foundation; the A.P. Sloan Foundation; the Bundesministerium für Bildung und Forschung, Germany; the Korean Science and Engineering Foundation and the Korean Research Foundation; the Particle Physics and Astronomy Research Council and the Royal Society, UK; the Russian Foundation for Basic Research; the Comisión Interministerial de Ciencia y Tecnología, Spain; in part by the European Community's Human Potential Programme under contract HPRN-CT-2002-00292; and the Academy of Finland. We thank M. Carena, B. Dobrescu, P. Langacker, H. Logan, and T. Tait for many fruitful discussions.

[1] F. del Aguila, M. Quiros, and F. Zwirner, Nucl. Phys. **B287**, 419 (1987); J. L. Hewett and T. G. Rizzo, Phys. Rept.**183**, 193 (1989).
[2] M. Carena *et al.*, Phys. Rev. D **70**, 093009 (2004).
[3] J. Erler *et al.*, Phys. Rev. D **66**, 015002 (2002). T. Han *et al.*, Phys. Rev. D **70**, 115006 (2004).
[4] N. Arkani-Hamed *et al.*, J. High Energy Phys. 07, 034 (2002).
[5] T. Han *et al.*, Phys. Rev. D **67**, 095004 (2003).
[6] A. Abulencia *et al.*, Phys. Rev. Lett. **95**, 252001 (2005).
[7] D. Acosta *et al.*, Phys. Rev. Lett. **95**, 131801 (2005).
[8] J. L. Rosner, Phys. Rev. D **54**, 1078 (1996); T. Affolder *et al.*, Phys. Rev. Lett. **87**, 131802 (2001).
[9] J. L. Rosner, Phys. Rev. D **35**, 2244 (1987).
[10] J. Kang and P. Langacker, Phys. Rev. D **71**, 035014 (2005).
[11] F. Abe *et al.*, Nucl. Instrum. Methods Phys. Res., Sect. A **271**, 387 (1988); D. Amidei *et al.*, *ibid.* **350**, 73 (1994); P. Azzi *et al.*, *ibid.* **360**, 137 (1995).
[12] In the CDF geometry, θ is the polar angle with respect to the proton beam axis (positive z direction), and ϕ is the azimuthal angle. The pseudorapidity is $\eta = -\ln[\tan(\theta/2)]$. The transverse momentum, p_T, is the component of the momentum projected onto the plane perpendicular to the beam axis. The transverse energy E_T of a shower or calorimeter tower is E $\sin\theta$, where E is the energy deposited.
[13] D. Acosta *et al.*, Phys. Rev. Lett. **94**, 091803 (2005).
[14] D. Acosta *et al.*, Phys. Rev. D **71**, 052002 (2005).
[15] The couplings we use are detailed in C. Ciobanu *et al.*, FERMILAB-FN-0773-E (2005).
[16] The K-factor, used in Ref. [2], was provided to us by M. Carena, Fermilab.
[17] GEANT, *"Detector Description and Simulation Tool"*, CERN Program Library Long Writeup W5013 (1993).
[18] T. Sjöstrand *et al.*, Comput. Phys. Commun. **135**, 238 (2001). We use PYTHIA version 6.129a.
[19] R. Hamberg, W. L. van Neerven, and T. Matsuura, Nucl. Phys. **B359**, 343 (1991).
[20] R. V. Harlander and W. B. Kilgore, Phys. Rev. Lett. **88**, 201801 (2002).
[21] J. M. Campbell and R. K. Ellis, Phys. Rev. D **60**, 113006 (1999).
[22] A. L. Read, J. Phys. G: Nucl. Part. Phys. **28**, 2693 (2002). P. Bock *et al.* (the LEP Collaborations), CERN-EP-98-046 (1998) and CERN-EP-2000-055 (2000).
[23] H. Lai *et al.*, Phys. Rev. D **51**, 4763 (1995). The CTEQ6 information can be found here: `http://user.pa.msu.edu/wkt/cteq/cteq6/cteq6pdf.html`.
[24] J. Pumplin *et al.*, Phys.Rev. D **65**, 014013 (2002).
[25] D. Abbaneo *et al.* (the LEP Collaborations) and N. de Groot *et al.* (the SLD Collaboration), CERN-PH-EP-2004-069

(2004).
[26] F. Abe *et al.*, Phys. Rev. Lett. **79**, 2198 (1997).
[27] E. J. Eichten, K. D. Lane, M. E. Peskin, Phys. Rev. Lett. **50**, 811 (1983).
[28] We use: VV(AA)=LL+LR+(−)RL+(−)RR.

Chapter 8

Conclusion

The forward-backward charge asymmetry of the Z boson is measured with the CDF Run II data. The integrated luminosity of the data is 364 pb^{-1}. The χ^2 with respect to the standard model prediction is found to be 10.9, where the number of degrees of freedom is 12.

The signature of an extra neutral gauge boson Z' is probed. Both the di-electron invariant mass distribution and $\cos\theta^*$ distribution were investigated. No evidence for Z' is found. The mass limits are set for chosen Z' models. A model-independent parameterization is used to constrain the Z' mass.

Although no evidence of a new physics is found, searches for new physics will be carried on for the rest of the CDF experiment, and then continued by the LHC experiments. LHC will start running in 2007, colliding proton beams at the center of momentum energy of 14 TeV. The expected signal of the $Z' \to \mu^+\mu^-$ with $M_{Z'} = 1$ TeV at an LHC experiment is shown in the Fig. 8.1. It is noteworthy that even with the early LHC data it would be possible to discover a Z' if its mass is not much higher than 1 TeV/c^2. Z' is one of the earliest new physics signals expected from the LHC experiments.

While M_{ee} distribution would play an important role for the discovery of Z', other properties of the Z' such as its couplings to the fermions can be probed through the measurement of the A_{FB} around the Z' mass. Fig. 8.2 [30] shows the expected A_{FB} as functions of M_{ee} for different Z' models. The measurement of the A_{FB} therefore provides discrimination power between theories that predict different Z' couplings, and the Z' search at the Tevatron has demonstrated that such an analysis could be realized in the hadron collider environment.

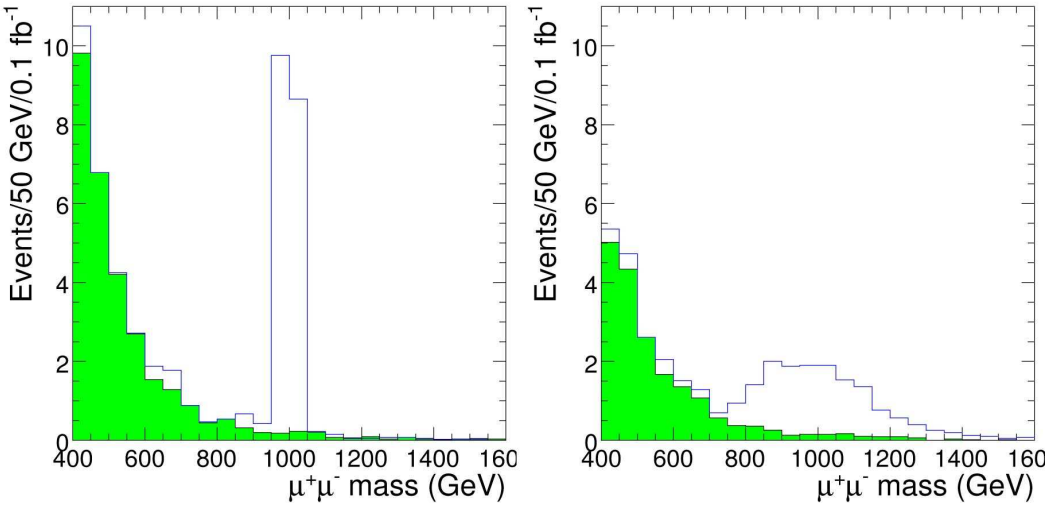

Figure 8.1: The expected $Z' \rightarrow \mu^+\mu^-$ signature at the ATLAS experiment. Z_η with a mass of 1 TeV/c^2 with the integrated luminosity of 0.1 fb^{-1} is assumed. The invariant mass distribution at the generator level is shown on the left. Z_η plus background is the open histogram, and the shaded one is for background only. The expected observed distribution during the early phase of the misaligned reconstruction is shown on the right.

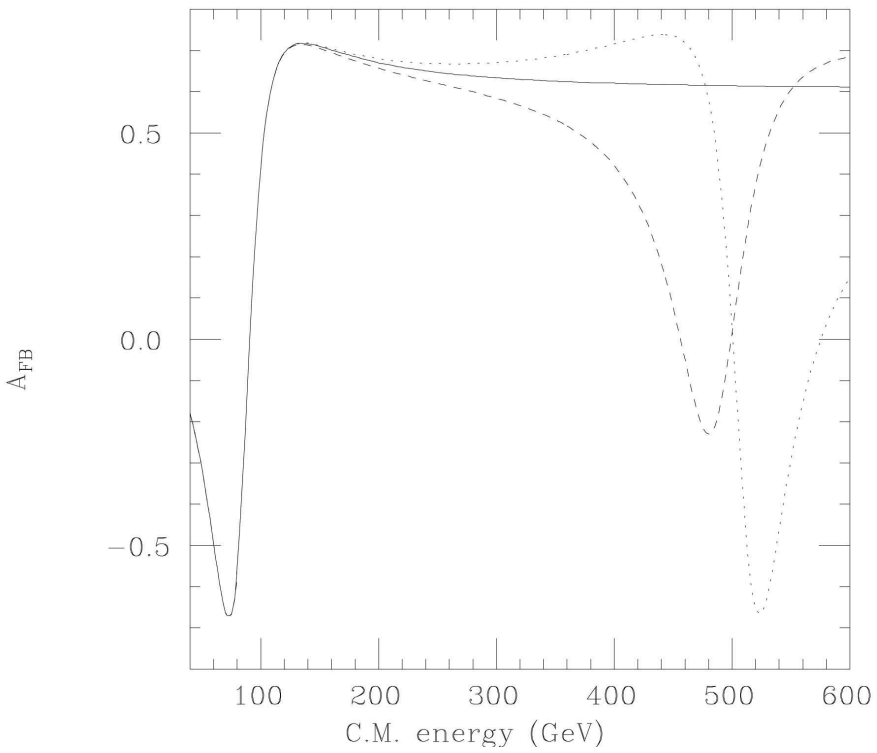

Figure 8.2: Parton-level forward-backward asymmetries for $u\bar{u} \to e^+e^-$. Solid line: standard model. Dashed line: 500 GeV/c^2 Z_χ added. Dotted line: 500 GeV/c^2 Z_ψ added.

Appendix A

Glossary

CDF Collider Detector at Fermilab.

CEM Central Electromagnetic Calorimeter.

CES Central Electromagnetic Showermax.

COT Central Outer Tracker.

CPR Central Preshower Radiator.

MET Missing Transverse Energy.

Parton Quarks and gluons that comprise protons and neutrons.

PDF Parton Distribution Function.

PEM Plug Electromagnetic Calorimeter.

PES Plug Electromagnetic Showermax.

PPR Plug Preshower Radiator.

QCD Quantum Chromodynamics.

QED Quantum Electrodynamics.

Bibliography

[1] *A combination of preliminary electroweak measurements and constraints on the standard model*, (2003).

[2] F. Abe et al., *The CDF detector: An overview*, Nucl. Instr. Meth. **A271** (1988), 387.

[3] A. Abulencia et al., *Search for Z' $\rightarrow e^+e^-$ using dielectron mass and angular distribution*, Phys. Rev. Lett. **96** (2006), 211801.

[4] Anthony A. Affolder et al., *CDF central outer tracker*, Nucl. Instrum. Meth. **A526** (2004), 249–299.

[5] M. G. Albrow et al., *The CDF plug upgrade electromagnetic calorimeter: Test beam results*, Nucl. Instrum. Meth. **A480** (2002), 524–546.

[6] Guido Altarelli, *The standard model of particle physics*, (2005).

[7] Guido Altarelli and Martin W. Grunewald, *Precision electroweak tests of the standard model*, Phys. Rept. **403-404** (2004), 189–201.

[8] L. Balka et al., *The CDF central electromagnetic calorimeter*, Nucl. Instrum. Meth. **A267** (1988), 272.

[9] R. Barate et al., *Search for the standard model higgs boson at LEP*, Phys. Lett. **B565** (2003), 61–75.

[10] Roger J. Barlow and Christine Beeston, *Fitting using finite monte carlo samples*, Comput. Phys. Commun. **77** (1993), 219–228.

[11] Arie Bodek and Ulrich Baur, *Implications of a* 300 $GeV - 500$ GeV/c^2 *Z' boson on p anti-p collider data at* $s^{1/2} = 1.8$ *TeV*, Eur. Phys. J. **C21** (2001), 607–611.

[12] Roberto Bonciani, Stefano Catani, Michelangelo L. Mangano, and Paolo Nason, *NLL resummation of the heavy-quark hadroproduction cross- section*, Nucl. Phys. **B529** (1998), 424–450.

[13] N. Cabibbo, L. Maiani, G. Parisi, and R. Petronzio, *Bounds on the fermions and higgs boson masses in grand unified theories*, Nucl. Phys. **B158** (1979), 295.

[14] M. Cacciari, S. Frixione, M. L. Mangano, P. Nason, and G. Ridolfi, *The t anti-t cross-section at* 1.8 *TeV and* 1.96 *TeV: A study of the systematics due to parton densities and scale dependence*, JHEP **04** (2004), 068.

[15] J. M. Campbell and R. K. Ellis, *An update on vector boson pair production at hadron colliders*, Phys. Rev. **D60** (1999), 113006.

[16] Marcela Carena, Alejandro Daleo, Bogdan A. Dobrescu, and Tim M. P. Tait, *Z' gauge bosons at the tevatron*, Phys. Rev. **D70** (2004), 093009.

[17] Stefano Catani, Michelangelo L. Mangano, Paolo Nason, and Luca Trentadue, *The top cross section in hadronic collisions*, Phys. Lett. **B378** (1996), 329–336.

[18] John C. Collins and Davison E. Soper, *Angular distribution of dileptons in high-energy hadron collisions*, Phys. Rev. **D16** (1977), 2219.

[19] F. Englert and R. Brout, *Broken symmetry and the mass of gauge vector mesons*, Phys. Rev. Lett. **13** (1964), 321–322.

[20] G. S. Guralnik, C. R. Hagen, and T. W. B. Kibble, *Global conservation laws and massless particles*, Phys. Rev. Lett. **13** (1964), 585–587.

[21] F. Halzen and Alan D. Martin, *Quarks and leptons: An introductory course in modern particle physics*, New York, Usa: Wiley (1984).

[22] R. Hamberg, W. L. van Neerven, and T. Matsuura, *A complete calculation of the order α_s^2 correction to the drell-yan K factor*, Nucl. Phys. **B359** (1991), 343–405.

[23] JoAnne L. Hewett and Thomas G. Rizzo, *Low-energy phenomenology of superstring inspired E(6) models*, Phys. Rept. **183** (1989), 193.

[24] Peter W. Higgs, *Broken symmetries, massless particles and gauge fields*, Phys. Lett. **12** (1964), 132–133.

[25] M.Herndon C.-J.Lin A.Yagil J.Thom, D.Glenzinski, *Determination of the run II COT tracking efficiency using the w-no-track sample*, CDF Internal Note 6866 (2004).

[26] M. Lefebvre, R. K. Keeler, R. Sobie, and J. White, *Propagation of errors for matrix inversion*, Nucl.Instrum.Meth.A **451** (2000), 520.

[27] M. Lindner, *Implications of triviality for the standard model*, Zeit. Phys. **C31** (1986), 295.

[28] J. Pumplin et al., *New generation of parton distributions with uncertainties from global QCD analysis*, JHEP **07** (2002), 012.

[29] Alexander L. Read, *Presentation of search results: The CL_s technique*, J. Phys. **G28** (2002), 2693–2704.

[30] Jonathan L. Rosner, *Forward-backward asymmetries in hadronically produced lepton pairs*, Phys. Rev. **D54** (1996), 1078–1082.

[31] Jonathan L. Rosner, *Resource letter: The standard model and beyond*, Am. J. Phys. **71** (2003), 302–318.

[32] Torbjorn Sjostrand et al., *High energy physics event generation with PYTHIA 6.1*, Comput. Phys. Commun. **135** (2001), 238–259.

[33] Steven Weinberg, *A model of leptons*, Phys. Rev. Lett. **19** (1967), 1264–1266.

[34] Chen-Ning Yang and Robert L. Mills, *Conservation of isotopic spin and isotopic gauge invariance*, Phys. Rev. **96** (1954), 191–195.